UNIVERSITY
OF MICHIGAN
MAY 11 1956
CHEMISTRY
LIBRARY

Journal of Research

of the National Bureau of Standards

MARCH 1956

VOLUME 56 NUMBER 3

U. S. DEPARTMENT OF COMMERCE
Sinclair Weeks, Secretary
NATIONAL BUREAU OF STANDARDS
A. V. Astin, Director

MARCH • 1956
VOLUME • 56
NUMBER • 3

JOURNAL OF RESEARCH

of the

NATIONAL BUREAU OF STANDARDS

PERIODICALS OF THE NATIONAL BUREAU OF STANDARDS

(Published monthly)

The National Bureau of Standards is engaged in fundamental and applied research in physics, chemistry, mathematics, and engineering. Projects are conducted in fifteen fields: electricity and electronics, optics and metrology, heat and power, atomic and radiation physics, chemistry, mechanics, organic and fibrous materials, metallurgy, mineral products, building technology, applied mathematics, data processing systems, cryogenic engineering, radio propagation, and radio standards. The Bureau has custody of the national standards of measurement and conducts research leading to the improvement of scientific and engineering standards and of techniques and methods of measurement. Testing methods and instruments are developed; physical constants and properties of materials are determined; and technical processes are investigated.

JOURNAL OF RESEARCH

The Journal presents research papers by authorities in the specialized fields of physics, mathematics, chemistry, and engineering. Complete details of the work are presented, including laboratory data, experimental procedures, and theoretical and mathematical analyses. Annual subscription: domestic, $4.00; $1.25 additional for foreign mailing.

TECHNICAL NEWS BULLETIN

Summaries of current research at the National Bureau of Standards are published each month in the Technical News Bulletin. The articles are brief, with emphasis on the results of research, chosen on the basis of their scientific or technologic importance. Lists of all Bureau publications during the preceding month are given, including Research Papers, Handbooks, Applied Mathematics Series, Building Materials and Structures Reports, Miscellaneous Publications, and Circulars. Each issue contains 12 or more two-column pages; illustrated. Annual subscription: domestic, $1.00; 35 cents additional for foreign mailing.

BASIC RADIO PROPAGATION PREDICTIONS

The Predictions provide the information necessary for calculating the best frequencies for communication between any two points in the world at any time during the given month. The data are important to all users of long-range radio communications and navigation, including broadcasting, airline, steamship, and wireless services, as well as to investigators of radio propagation and ionosphere. Each issue, covering a period of one month, is released three months in advance and contains 16 large pages, including pertinent charts, drawings, and tables. Annual subscription: domestic, $1.00; 25 cents additional for foreign mailing.

Order all publications from the Superintendent of Documents
U. S. Government Printing Office, Washington 25, D. C.

The printing of this publication has been approved by the Director of the Bureau of the Budget, May 12, 1953.

Journal of Research of the National Bureau of Standards Vol. 56, No. 3, March 1956 Research Paper 2656

Penetration of Gamma Radiation From a Plane Monodirectional Oblique Source[1]

Martin J. Berger

The penetration of gamma radiation from a plane monodirectional oblique source is solved by the moment method of Spencer and Fano. The novel feature of the treatment is the systematic investigation and exploitation of a function-fitting technique, which consists of approximating the desired radiation-flux function, $f(x)$, by an expression of the form $\sum_n A_n \phi(B_n x)$, the parameters A_n and B_n being determined from the knowledge of the flux moments.

A discussion is given of the criteria for the proper choice of the "weight function," $\phi(x)$, and of the accuracy of the fitting procedure. The results of a sample calculation are presented for an 0.66-Mev source in water.

1. Introduction

One of the most effective techniques for calculating the diffusion of gamma rays in infinite media is the moment method [1],[2] i. e., the determination of the spatial and angular moments of the radiation flux and subsequent calculation of the flux-distribution function by moment-fitting. This technique has been successfully applied to the calculation of radiation from plane and point isotropic sources and from monodirectional plane sources emitting radiation perpendicularly to the source plane [2]. The purpose of this work is to extend the method to the determination of the propagation of radiation from monodirectional *oblique* plane sources, i. e., sources emitting photons at a specified obliquity angle with respect to the source plane. In the problems treated previously, analytical asymptotic theory was available describing the radiation field at great distances from the source [3]; this facilitated the reconstruction of the flux function from its moments. For the problem of the oblique source, reliable guidance in the form of a corresponding analytical asymptotic theory is lacking, so that increased care must be given to the moment-fitting procedures.

Although specific application of the method described in this paper will be made to the diffusion of gamma radiation, the technique used should also be useful for determining the propagation of other types of radiation, e. g., neutrons, from plane oblique sources.

We consider an infinite homogeneous scattering medium that contains, in the plane $z=0$, a radiation source emitting 1 photon per square centimeter per second. The source photons are all emitted with energy E_0, and in directions inclined at an angle α with respect to the normal to the source plane. (The distribution of the azimuthal directions with which the photons are emitted may be considered arbitrary, being irrelevant for the propagation as a function of distance from the source plane.) Our task is to determine the energy flux, $F^{(\alpha)}(E,z)dE$, at a distance z from the source plane, due to photons in the energy range $(E,E+dE)$ as a function of the obliquity α. The energy flux is defined as the flow of energy through an isotropic detector with unit cross-sectional area. The energy, E, will be expressed in million electron volts and the distance, z, in units of the mean free path of the primary radiation.

Unscattered radiation will be treated separately because its direct calculation is trivial. In order to facilitate the moment-fitting procedures, separate consideration will also be given to singly-scattered radiation. This separation is desirable because its flux distribution differs considerably from that of the multiply-scattered radiation.

---

[1] This work was supported by the Office of Naval Research and the Armed Forces Special Weapons Project.

[2] Figures in brackets indicate the literature references at the end of this paper.

Section 2 discusses the moment-fitting procedures appropriate to the problem. In section 3 specific application of these methods is made to radiation with a source energy of 0.66 Mev (cesium–137 radiation) in a scattering medium of water. Various energy spectra and space distributions are presented as functions of the obliquity angle. In section 4 the accuracy of the results is investigated by the comparison of various methods of moment-fitting and by comparisons with other related calculations and with an experiment. Details and subsidiary questions are given in appendixes.

In appendix A, equations are derived for the calculation of the flux of singly-scattered radiation. In appendix B it is explained how the flux moments are calculated by the Spencer-Fano method; in particular, it will be pointed out how the moments required for the treatment of the monodirectional oblique plane source radiation can be obtained from a certain set of standard moments computed on the NBS automatic computer (SEAC). Appendix C presents details of the moment-fitting procedure.

2. Moment-Fitting Methods

2.1. Introductory Remarks

We assume that the first eight spatial moments of the energy flux,

$$\overline{z^n}(E,\alpha)=\int_{-\infty}^{\infty} z^n F^{(\alpha)}(E,z)dz, \tag{1}$$

$$(n=0,1,\ldots,7),$$

are known. (It is assumed that $F^{(\alpha)}$ stands for the flux of singly-scattered or multiply-scattered radiation, whichever we may want to determine. For details concerning the computation of the moments, see appendix B.)

Although a well-behaved function is determined uniquely if all its moments are known the reconstruction of a function from only eight moments requires some finesse. It is desirable to incorporate prior knowledge concerning the flux that is available from related analytical calculations, physical intuition, or experience with similar problems, into a so-called weight function, which serves as the initial approximation. Successive improved approximations are then found by the use of the moments.

In order to choose this weight function properly, we must give some thought to the expected spatial dependence of the flux function. Assuming that $0\leq\alpha\leq\pi/2$, i. e., that the photons are released by the source in the direction of positive z, we anticipate that the flux of scattered radiation will be a unimodal asymmetric function of z with a peak at a value of z somewhat larger than zero, and decreasing more rapidly on the negative than on the positive side of the peak. The asymmetry of the function will depend on the obliquity, being a maximum when $\alpha=0$, and zero when $\alpha=\pi/2$. Furthermore, it can be expected that at large distances from the source plane the flux has a dominantly exponential behavior as function of z.

To find a weight function embodying these features is difficult. The task is made easier if the flux is split into a symmetric component $f^{(\alpha)}(E,z)$ and an antisymmetric component $g^{(\alpha)}(E,z)$, so that

$$F^{(\alpha)}(E,z)=f^{(\alpha)}(E,z)+g^{(\alpha)}(E,z) \tag{2a}$$

$$F^{(\alpha)}(E,-z)=f^{(\alpha)}(E,z)-g^{(\alpha)}(E,z), \tag{2b}$$

where z denotes $|z|$. In this manner we can account for the expected peak without incorporating this feature into $f^{(\alpha)}$ and $g^{(\alpha)}$, which may be chosen to be more or less smooth, monotonic asymptotically exponential functions. There is another advantage inherent in this splitting

technique. We can fit four even moments to determine $f^{(\alpha)}$ and four odd moments to determine $g^{(\alpha)}$. This is much easier than fitting eight moments simultaneously. There is a slight disadvantage also; the flux cannot be determined very accurately far behind the source because for large negative values of z the functions $f^{(\alpha)}$ and $g^{(\alpha)}$ will have nearly the same value, and their difference will be rather inaccurate. This is not a serious drawback because the small amount of radiation far behind the source usually is not of much interest.

2.2. Polynomial Expansions

We shall now discuss the method of polynomial expansion used by Spencer and Fano [1] for the solution of the plane source with $\alpha=0$ and explain why this approach cannot readily be carried over to the treatment of the source with $\alpha\neq 0$.

Spencer and Fano also made use of the splitting technique and set

$$f^{(0)}(E,z)=\frac{e^{-wz}}{2}\sum_{n=0}^{\infty}c_n(E)U_n(wz) \tag{3a}$$

$$g^{(0)}(E,z)=\frac{wze^{-wz}}{2}\sum_{n=0}^{\infty}d_n(E)V_n(wz), \tag{3b}$$

where z denotes $|z|$; $e^{-wz}/2$ and $wze^{-wz}/2$ are the respective weight functions.

$$U_n(z)=\frac{(-1)^n}{2^n}\left(\frac{\partial}{\partial z}-1\right)^{2n}\sum_{j=0}^{n}\binom{n+j}{j}\frac{1}{(n-j)!}2^{-j}z^{n-j}, \tag{4a}$$

and

$$V_n(z)=\frac{2}{2(n+1)}\left(\frac{\partial}{\partial z}-1\right)^{2}U_n(z) \tag{4b}$$

$$(n=0,1,2,\cdots)$$

are orthogonal polynomial systems associated with these weight functions. The coefficients $c_n(E)$ and $d_n(E)$ are related to the moments as follows, the nth coefficient involving only moments of order not exceeding n.

$$c_n(E)=\sum_{j=0}^{n}\binom{n}{j}\frac{(-1)^j}{(2j)!}\overline{(wz)^{2j}} \tag{5a}$$

$$d_n(E)=\sum_{j=1}^{n+1}\binom{n+1}{j}\frac{(-1)^{j-1}}{(2j-1)!}\overline{(wz)^{2j-1}} \tag{5b}$$

The validity of such a polynomial expansion depends on the correct choice of the exponent w in the weight functions. It can be shown by physical arguments and by related asymptotic penetration theory that a satisfactory choice for the plane source with obliquity zero is $w\approx(\mu_p/\mu_0)$, where μ_0 is the linear narrow-beam absorption coefficient of the primary radiation and μ_p that of the most penetrating component of the radiation. (This is usually, though not always, radiation with the primary energy.) With a correctly chosen parameter, the polynomial expansion will converge rapidly for wz up to ≈ 15, so that only a few terms requiring the use of the first few moments have to be fed into the expansion.

The parameter w is difficult to determine for the plane oblique source. Clearly, the radiation component with the highest energy (usually the component with the smallest attenuation coefficient) will not govern the deep penetration because it must travel a distance approximately equal to $z/\cos\alpha$ in order to get a distance z away from the source. On the other hand, radiation that has been turned parallel to the z-axis travels away from the source plane

on the shortest possible path but has lost energy, so that its attenuation is increased. One would expect that the deep penetration is controlled by the small amount of the radiation that has been turned approximately parallel to the z-axis in a number of collisions such that it has lost very little energy. It has been found by numerical experimentation that it is difficult to obtain reliable polynomial expansions by adjusting the parameter w on the basis of convergence considerations. These difficulties can be overcome, however, by another approach [4].

2.3. Function Fitting

If eight moments are available and an even-odd split is used, we set

$$f^{(\alpha)}(E,z)=A_1(E,\alpha)\phi[zB_1(E,\alpha)]+A_2(E,\alpha)\phi[zB_2(E,\alpha)] \tag{6a}$$

$$g^{(\alpha)}(E,z)=C_1(E,\alpha)\psi[zD_1(E,\alpha)]+C_2(E,\alpha)\psi[zD_2(E,\alpha)], \tag{6b}$$

where $\phi(z)$ and $\psi(z)$ are suitable weight functions with the desired asymptotic and symmetry properties:

$$\varphi(z)=\varphi(-z) \tag{7a}$$

$$\psi(z)=-\psi(-z). \tag{7b}$$

$$\left.\begin{aligned}\varphi(z)&=\bar{\varphi}(z)e^{-z}\\ \psi(z)&=\bar{\psi}(z)e^{-z}\end{aligned}\right\}\text{ for large } z, \tag{8a, 8b}$$

where $\bar{\varphi}(z)$ and $\bar{\psi}(z)$ are slowly varying functions of z.

The quantities A_j and C_j are intensity (normalization) parameters, and the B_j and D_j are scale parameters. The introduction of location parameters is not necessary because the peak in the flux function will be determined by the superposition of symmetric and antisymmetric solutions. The parameters B_j and D_j, analogous to the parameter w in the method of polynomial expansion, will be effectively determined from the moments themselves, so that no "inspired guess" is necessary.

We require that

$$\overline{z^{2n}}(E,\alpha)=\sum_{j=1}^{2}A_j(E,\alpha)\int_{-\infty}^{\infty}z^{2n}\phi[zB_j(E,\alpha)]dz \tag{9a}$$

$$(n=0,1,2,3)$$

$$\overline{z^{2n+1}}(E,\alpha)=\sum_{j=1}^{2}C_j(E,\alpha)\int_{-\infty}^{\infty}z^{2n+1}\psi[zD_j(E,\alpha)]dz. \tag{9b}$$

The solution of these equations is described in appendix C. The important aspect of the solution is the fact that there are restrictions on the class of allowed weight functions $\phi(z)$ and $\psi(z)$. In order to obtain the desired asymptotic behavior, it is required that the scale parameters B_j and D_j are real-valued; otherwise, the weight functions would turn into oscillatory functions, which is inconsistent with the expected smooth behavior of the radiation density function.

As shown in appendix C, two pairs of dimensionless parameters may be introduced to characterize the relation between the function to be fitted and the proposed weight functions:

$$\left.\begin{aligned}s&=\frac{m_2^2}{m_0m_4}\frac{M_0M_4}{M_2^2}\\ t&=\frac{m_2^3}{m_0^2m_6}\frac{M_0^2M_6}{M_2^3}\end{aligned}\right\} \tag{10}$$

$$\left.\begin{aligned}\hat{s}&=\frac{m_3^2}{m_1m_5}\frac{M_1M_5}{M_3^2}\\ \hat{t}&=\frac{m_3^3}{m_1^2m_7}\frac{M_1^2M_7}{M_3^3}\end{aligned}\right\} \tag{11}$$

where $M_n=\overline{z^n}(E,\alpha)$, $m_{2n}=\int_{-\infty}^{\infty}z^{2n}\varphi(z)dz$, and $m_{2n+1}=\int_{-\infty}^{\infty}z^{2n+1}\psi(z)dz$.

The weight function $\varphi(z)$ belongs to the allowed class (i. e., the scale parameters B_j are real) if, and only if, the point (s,t) lies in an "allowed region" of the s-t plane, indicated by the shaded area in figure 1 and specified in appendix C. To determine whether $\psi(z)$ is allowable, we replace the point (s,t) by $(\hat{s},\hat{t})$ and use the same diagram.

It has been found in this investigation and in other related work, that considerable searching is often necessary to get an allowed weight function, but when there are several such functions they yield moment-fitting results that are in close agreement. Thus the function-fitting technique seems to operate in a sort of all-or-nothing fashion, and differs in this respect from the polynomial expansion method.

The symmetric and asymmetric weight functions have been related as follows:

$$\psi(z)=z\varphi(z). \tag{12}$$

This implies that at $z=0$, the antisymmetric component of the scattered flux vanishes and the total scattered flux is continuous.[3] The choice of z, rather than some other antisymmetric function of z as the proportionality factor in eq (12) is somewhat arbitrary but recommends itself by its simplicity and is consistent with what is known about the analytical behavior of the flux carried by photons with energies close to the source energy.

[3] The unscattered flux is obtained as space integral over the source function and the flux of the nth order of scattering as a space integral over the flux of the $n-1$st order of scattering. The source function is a delta function $\delta(z)$. The unscattered flux thus has a simple discontinuity at the origin, whereas the flux of higher orders of scattering is continuous.

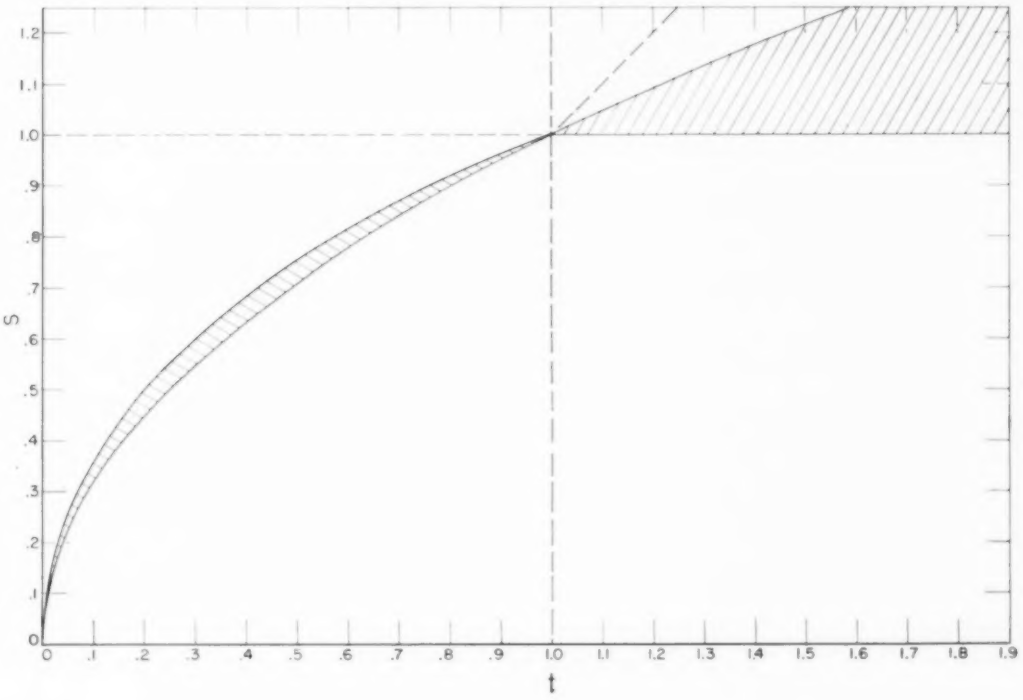

FIGURE 1. *Diagram indicating whether a weight-function is "permissible" for function-fitting.*

The diagram should extend over the region $0\leq s\leq\infty$, $0\leq t\leq\infty$, but only a portion of this region is shown. A weight-function is "permissible" if its (s, t)-point lies in the shaded region of the diagram.

3. Numerical Application: Radiation from a 0.66-Mev Plane-Oblique Source in Water

A sample calculation, based on the methods outlined in section, 2 was carried out for a source of 0.66-Mev photons (radiation from cesium-137) in water.

The flux moments needed as input data were calculated on the SEAC at energies ranging from 0.66 to 0.134 Mev. At lower energies, spectra were obtained through an extrapolation procedure based on two characteristic features of gamma-ray diffusion:

(1) At very low energies an equilibrium spectrum prevails in the sense that the flux can (at least, approximately) be factored into the product of a space-dependent function and an energy-dependent function. This has been shown to be the case for radiation from point and plane isotropic sources [2, 3], and there is no reason to doubt that it will also hold for plane oblique sources.

(2) The shape of the energy spectrum at low energies is nearly independent of the source energy. This is demonstrated by plotting in figure 2 the moment $M_0(E)$ of the flux in water as a function of energy in the range from 0.134 Mev down to 0.020 Mev for source energies of 0.255 Mev and 1.0 Mev. The two curves have been normalized in such a manner that they have the same ordinate at 0.134 Mev. It can be seen that they lie quite close together; the area under the corresponding curve for 0.66-Mev source energy, which must lie between them, can be estimated with an accuracy of 5 percent. (For the purpose of this estimate, only multiply-scattered radiation from the 0.255-Mev source should be considered because a 0.66-Mev source will produce only multiply-scattered radiation below 0.134 Mev.)

Computations were carried out for the energies and angles of incidence indicated in table 1.

Singly-scattered radiation was calculated directly according to the equations given in appendix A. Some moment calculations were also made and are discussed in section 4.

Multiply-scattered radiation was treated by the moment-method according to the function-fitting procedure outlined in section 2. It is desirable that one can fit the flux for as many

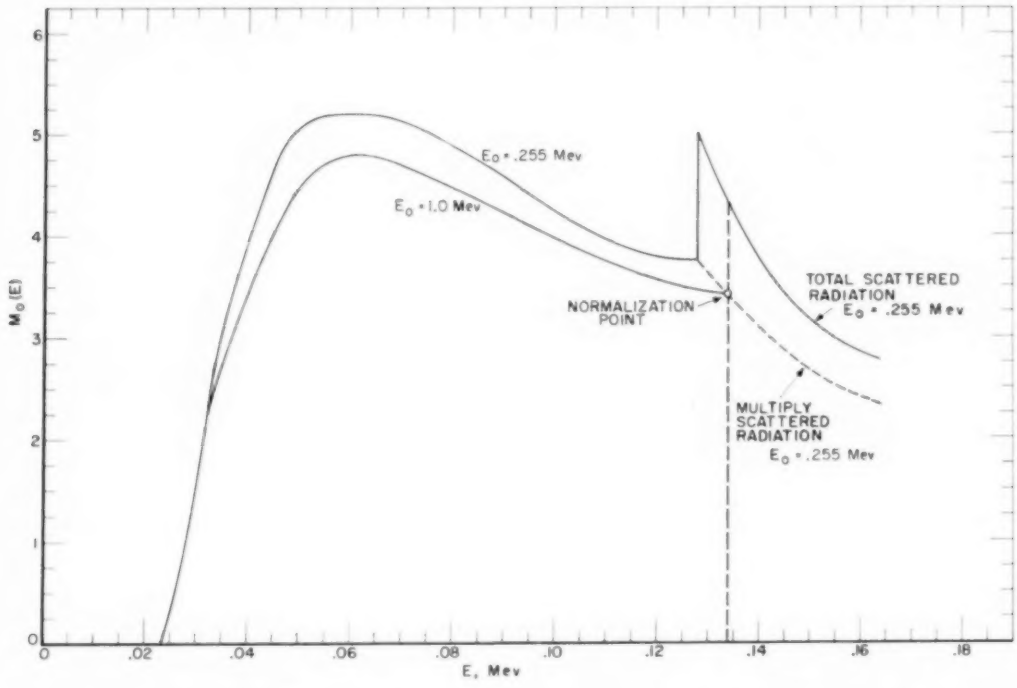

FIGURE 2. *Energy spectrum of scattered gamma radiation from 1.0- and 0.255-Mev sources in a scattering medium of water.*

These distributions were used to obtain by interpolation the low-energy part of the spectral distribution of radiation from a 0.66-Mev source.

TABLE 1. *Energies and obliquity angles for which the energy flux was calculated.*

[Asterisks indicate the values for which the multiply-scattered flux was determined by the method of function-fitting with the use of the weight function $\varphi(z)=L_{5/2}(z)$.]

E	α			
	0°	30°	60°	90°
Mev				
0.660	*	*	*	
.503	*	*		*
.325		*	*	*
.259			*	*
.215	*	*	*	*
.184	*	*	*	*
.159	*	*	*	*
.134	*	*	*	*

energies and source obliquities as possible with the use of the same weight function. This not only inspires confidence that the choice of the weight function is correct, but more importantly, it makes possible smooth interpolation. A considerable number of weight functions were tried, and the results obtained with them are described in section 4.

Preference was finally given to the function

$$\varphi(z)=z^{5/2}K_{5/2}(z)=L_{5/2}(z), \tag{13}$$

where $K_{5/2}$ is a Bessel function of the second kind with imaginary argument. This weight function was superior to other functions considered in that its region of applicability included most of the energies and obliquity angles of interest (see table 1). In the relatively rare instances of nonapplicability, interpolation with the aid of results obtained with some of the other weight functions was successfully used. In any case, it is shown in section 4.2 that the results obtained with different weight functions were generally in excellent agreement. This provides pragmatic justification for the moment-fitting technique.[4]

The results of the sample calculations for a 0.66-Mev plane monodirectional oblique source in water are illustrated in figures 3, 4, and 5. Figure 3 (a, b, c, d) shows energy spectra of the flux of scattered radiation at various distances from the source plane for obliquity angles $\alpha=0°$, 30°, 60°, and 90°.[5] Figure 4 (a, b) shows the dependence of the total scattered flux $\int_0^{0.66} F^{(\alpha)}(E, z)dE$ on the source obliquity and the distance from the source plane.

When the penetration of radiation as a function of the obliquity angle is known, one can, by superposition, determine the penetration of radiation from plane sources with arbitrary angular distribution. An example of such an application is the calculation of the ratio

$$r(\cos\alpha', z)=\frac{\int_{\cos\alpha'}^{1} d\cos\alpha \int_0^{0.66} dEF^{(\alpha)}(E,z)}{\int_{-1}^{1} d\cos\alpha \int_0^{0.66} dEF^{(\alpha)}(E,z)}. \tag{14}$$

This is the fraction of the scattered integrated energy flux from an isotropic 0.66-Mev plane source that is due to source radiation emitted within a cone of opening α' around the normal to the source plane. This ratio is exhibited in figure 5 as a function of $\cos\alpha'$ for various values of z.

---

[4] One suspects that there may be a deeper-lying reason for the wide applicability of Bessel functions of the type used in eq (13). According to Spencer (private communication) such functions have also proved themselves useful for fitting flux moments for a point monodirectional source.

[5] The flux is expressed as the flow of energy, in Mev per Mev of spectral energy per unit time, through a unit area of surface perpendicular to the direction of motion of the radiation, i. e., through an isotropic detector with an efficiency independent of the direction of the incident radiation. The normalization corresponds to a source emitting one photon with an energy of 0.66 Mev per unit time and unit area. Distances from the source plane are expressed in mean free paths (mfp) of the primary radiation.

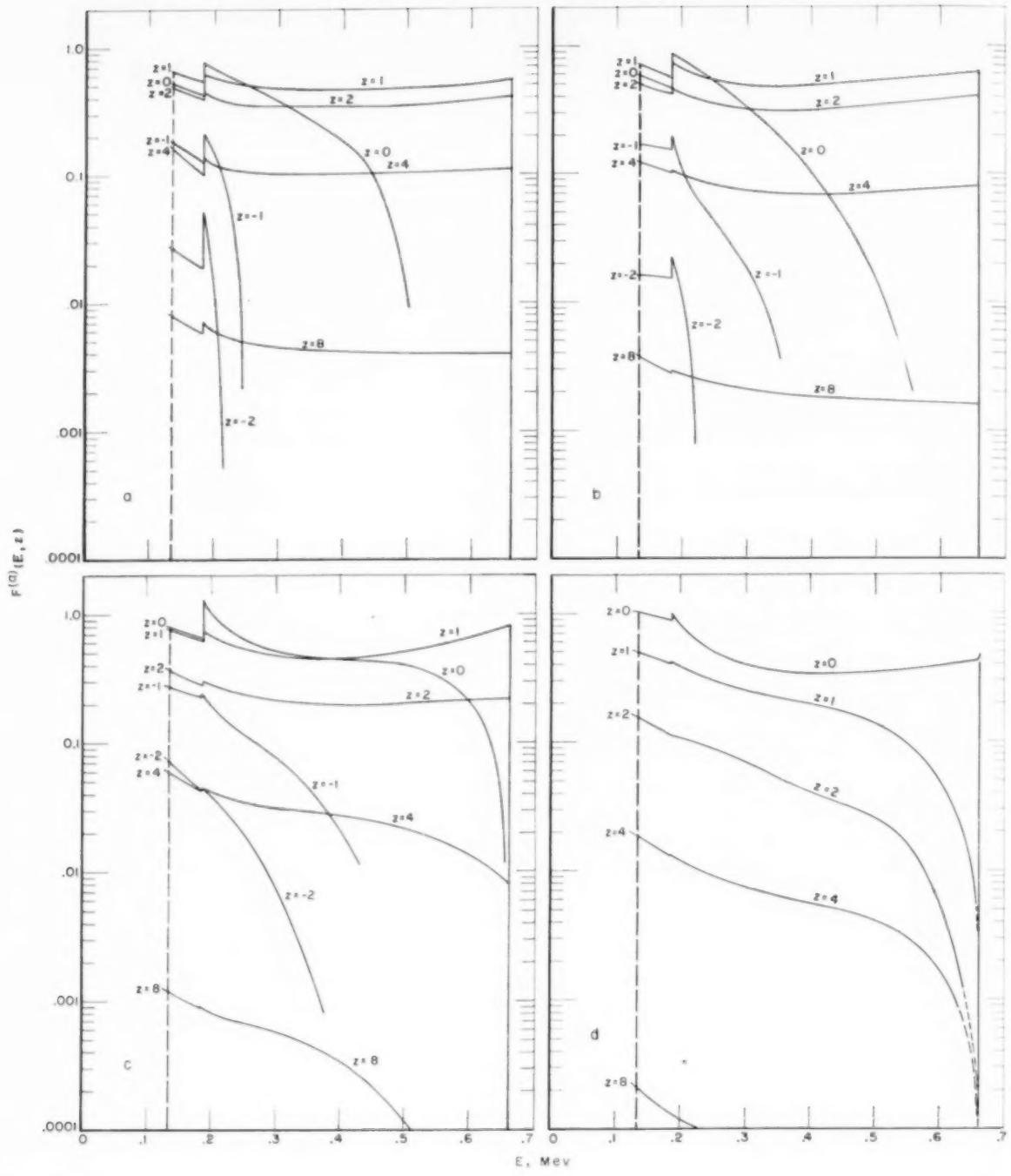

FIGURE 3. *Differential spectra $F^{(\alpha)}(E, z)$ of the scattered gamma-ray flux ((Mev/cm² sec)/Mev) at various distances z (mfp) from a plane monodirectional oblique source of 0.66-Mev radiation in a scattering medium of water.*

The ordinate scale corresponds to a source emitting 1 photon/cm² sec.
a, Obliquity α=0°; b, obliquity α=30°; c, obliquity α=60°; d, obliquity α=90°.

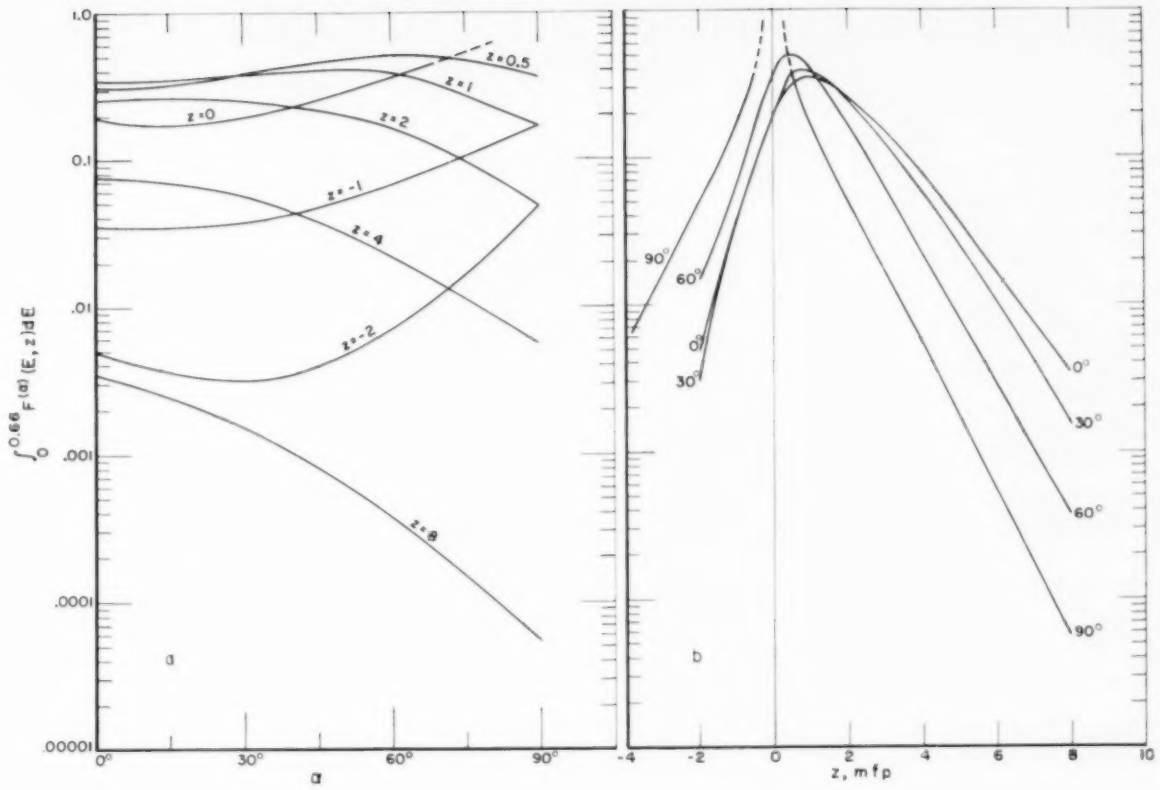

FIGURE 4. *Total scattered gamma-ray flux from a 0.66-Mev plane monodirectional oblique source in a scattering medium of water.*

The ordinate scale (in Mev/cm² sec) corresponds to a source emitting 1 photon/cm² sec.
a, Flux versus obliquity; b, flux versus distance from source plane (mfp).

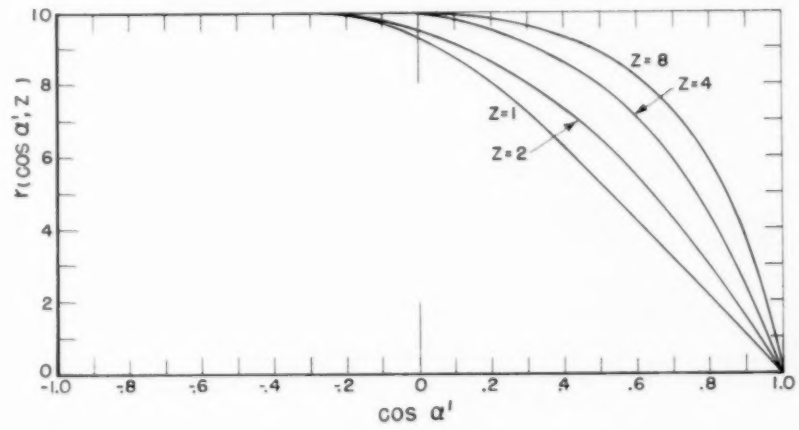

FIGURE 5. *Fraction of the scattered energy flux from a 0.66-Mev plane isotropic source in water that is due to source radiation emitted within a cone of opening α' around the normal to the source plane.*

375523—56——2

4. Checks and Comparisons

4.1. An Experimental Comparison

Experimental evidence with which the theory could be compared is unfortunately quite scarce, in fact is nonexistent for the exact conditions of the present problem. The only relevant published work seems to be that of Kirn, Kennedy, and Wyckoff [5], who measured the penetration of 0.66-Mev gamma radiation from oblique plane sources through slabs of concrete.

A comparison will be made by considering experimental and theoretical buildup factors. The energy buildup factor—a characteristic parameter widely used in shielding work—is defined as the ratio

$$\frac{\text{Total energy flux (scattered plus unscattered)}}{\text{Unscattered energy flux}}.$$

The fractional energy-transmission through a slab is the product of the buildup factor times the quantity $\exp(-z/\cos\alpha)$.

The experiment of Kirn et al. and the calculation differ in a number of respects: (a) The calculation for an infinite medium allows for the possibility that radiation can penetrate beyond the detector and then be backscattered into it. In the transmission experiment, however, with the detector behind a concrete slab and with no further backing behind the detector, such backscattering is impossible. The buildup factor for a slab is therefore smaller than that for an infinite medium. In a Monte Carlo calculation [6] it has been found that the ratio of the two buildup factors becomes nearly constant for penetrations greater than 4 mfp. (b) It is only approximately true that concrete may be considered a water-equivalent medium (by expressing all distances in mfp of the primary radiation). Actually, there is enough difference at low energies in the respective absorption coefficients (per electron) so that the buildup factors for concrete are appreciably lower than those for water. By referring to the extensive tabulations of Goldstein and Wilkins [2] it can be found that this reduction factor is a very slowly varying function of the penetration distance (except in the vicinity of the source).

The reason for the approximate constancy of the buildup reductions due to effects (a) and (b) lies in the fact that both are reductions of the low-energy end of the gamma-ray spectrum, but this part of the spectrum—as pointed out in section 3—is an approximate equilibrium spectrum, i. e., rather independent of the depth of penetration.

(c) The calculation assumes a monoenergetic source spectrum. In the experiment the source was physically large, and the source radiation was unfiltered, so that it presumably contained an appreciable amount of low-energy scattered radiation. Additional scattered radiation could have been introduced by the collimating arrangement.

(d) The calculation is for the energy flux, whereas the experimental detector response is proportional to the energy flux for energies down to 200 kev only, but rises somewhat more steeply at lower energies.

Figure 6 shows semilogarithmic plots of the experimental and theoretical buildup factors versus oblique penetration distance $z/\cos\alpha$ (in mfp), for obliquity angles $\alpha=0°$ and $\alpha=60°$. It can be seen that in both cases the experimental curves lie below the theoretical curves, and that for $(z/\cos\alpha)\gtrapprox 3$ the corresponding curves are almost parallel to each other, in conformity with the expectation of a constant buildup-factor reduction. For medium and deep penetration the theory therefore correctly predicts the relative attenuation of the energy flux at different depths.[4]

[4] For a more detailed quantitative comparison for obliquity $\alpha=0°$, taking into account the boundary effect according to the Monte Carlo method, see [6].

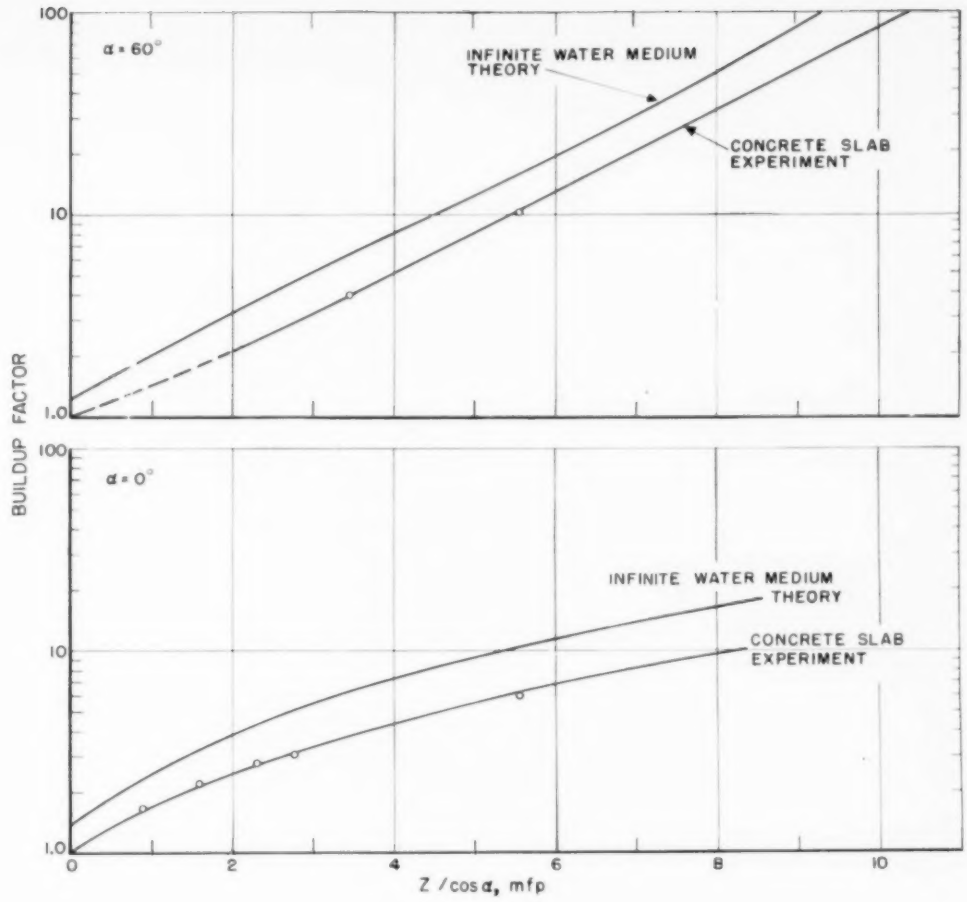

FIGURE 6. *Theoretical and experimental buildup factors for radiation from a 0.66-Mev plane monodirectional oblique source, plotted versus oblique penetration distance.*

The theoretical curves pertain to an infinite scattering medium of water, the experimental curves to a plane-parallel concrete barrier.

4.2. Comparison of Different Weight Functions and Moment-Fitting Procedures

In the absence of much experimental evidence that would provide a check on the theory, one is forced to rely heavily on tests of internal consistency. Hence a good deal of numerical experimentation has been accomplished, employing various weight functions to be used in the method of function-fitting, including also polynomial expansions whenever possible.

Listed below are the relevant properties of a few functions that were found to be useful as weight functions in fitting the flux distribution from monodirectional plane oblique sources. These functions were selected because they have the proper asymptotic behavior and are either available in tabulated form or easily evaluated directly. In the formulas below, z will be understood to mean $|z|$.

Bessel Functions:

$$\varphi(z)=L_p(z)=z^pK_p(z), \tag{15}$$

where K_p is a Bessel function of the second kind with imaginary argument.

$$m_{2n}=\int_{-\infty}^{\infty}dz z^{2n}\varphi(z)=2^{2n+p}\Gamma\left(\frac{1}{2}+n\right)\Gamma\left(\frac{1}{2}+n+p\right). \tag{16}$$

$$\lim_{z\to\infty} L_p(z)=\left(\frac{\pi}{2}\right)^{1/2} z^{p-1/2}e^{-z}. \tag{17}$$

If $p=q+\frac{1}{2}$, $(q=0,1,2,\ \ldots)$,

$$L_{q+1/2}(z)=\left(\frac{\pi}{2}\right)^{1/2} e^{-z}\sum_{i=0}^{q}\frac{(q+i)!}{(q-i)!\,i!}(1/2)^i\, z^{q-i}. \tag{18}$$

Generalized Exponential Integral:

$$\varphi(z)=E_p(z)=\int_1^\infty e^{-zt}\frac{dt}{t^p}. \tag{19}$$

(For $p=1$, this is the ordinary exponential integral).

$$\lim_{z\to\infty} E_p(z)=\frac{e^{-z}}{z} \tag{20}$$

$$m_{2n}=\frac{(4n)!}{2n+p}. \tag{21}$$

Error Function:

$$\varphi(z)=1-\operatorname{erf}(\sqrt{z})=1-\frac{2}{\sqrt{\pi}}\int_0^z e^{-t^2}\,dt, \tag{22}$$

$$\lim_{z\to\infty}\left[1-\operatorname{erf}(\sqrt{z})\right]=\frac{e^{-z}}{\sqrt{\pi z}}, \tag{23}$$

$$M_{2n}=\frac{(4n+1)!}{2^{4n}(2n+1)!}. \tag{24}$$

Gaussian Weight Function:

$$\varphi(z)=G(z)=\frac{e^{-z^2/2}}{\sqrt{2\pi}} \tag{25}$$

$$m_{2n}=\frac{(2n)!}{2^n n!} \tag{26}$$

Table 2 gives a comparison of moment-fitting results obtained at an energy of 0.184 Mev for obliquity angles $\alpha=0°$ and 60°. Results for the symmetric and antisymmetric components are shown separately. For comparative purposes the normalization has been chosen so that the results obtained with the weight function $L_{5/2}$ are the standard of comparison and have the value unity. The over-all conclusion can be reached from an inspection of table 2 that the various methods are in good agreement; nonnegligible discrepancies occur only very close to or very far from the source. It is to be noted that at $\alpha=0°$ there is a good agreement with the well-established method of polynomial expansion into U- and V-polynomials. Even a Gaussian weight function yields essentially the same results as the others at distances not too far from the source. The results of table 2 are typical and have been confirmed by other similar calculations.

It should be mentioned that function-fitting could also be carried out with the use of a larger number of moments than four by representing the flux by a functional series of more than two terms. If the use of the additional moments makes little difference, the fitting procedure is presumably accurate. Such a check would be equivalent to establishing the validity of a polynomial expansion by examining its convergence. In the sample calculation the number of available moments unfortunately was too small to do this.

TABLE 2. *Comparison of the results of moment fitting with different weight functions*

z	Weight function (normal incidence: $\alpha=0°$)					z	Weight function (oblique incidence: $\alpha=60°$)							
	$L_{3/2}$	$L_{7/2}$	$L_{9/2}$	G	e^{-z} (U-polynomial expansion)		$L_{1/2}$	$L_{3/2}$	$L_{5/2}$	$L_{7/2}$	$L_{9/2}$	E_4	E_5	$1-erf(\sqrt{z})$
0	1.00	0.981	0.970	0.918	1.66	0	1.15	1.04	1.00	0.976	0.961	1.30	1.12	1.09
0.5	1.00	.992	.986	.946	1.00	0.5	0.987	1.00	1.00	.999	.994	1.03	0.992	0.993
1	1.00	1.02	1.00	1.00	0.978	1	.936	0.962	1.00	1.01	1.02	0.920	.940	.939
2	1.00	0.998	1.01	1.07	.978	2	.998	.997	1.00	1.00	1.02	.911	.996	.992
4	1.00	.957	0.949	0.908	.974	4	1.03	1.02	1.00	0.984	0.974	.903	1.02	.963
8	1.00	.995	1.01	1.12	.977	8	0.904	0.926	1.00	.960	.972	.780	1.15	.901
16	1.00	.915	0.849	0.212	1.03	16	1.53	1.19	1.00	.680	.532	1.20	1.58	1.50
	$f^{(0)}$ (0.184, z)						$f^{(60)}$ (0.184, z)							
z	$zL_{3/2}$	$zL_{7/2}$	$zL_{9/2}$	ze^{-z} (V-polynomial expansion)		z	$zL_{1/2}$	$zL_{3/2}$	$zL_{5/2}$	$zL_{7/2}$	$zL_{9/2}$	zE_4	zE_5	
0.5	1.00	1.09	1.04	1.51		0.5	1.30	1.11	1.00	0.920	0.833	1.46	1.25	
1/2	1.00	1.12	1.09	1.25		1	1.02	1.02	1.00	.978	.951	0.992	1.06	
2	1.00	1.09	1.10	1.04		2	1.12	0.963	1.00	1.03	1.02	.910	0.877	
4	1.00	1.01	0.933	1.11		4	1.05	1.02	1.00	0.978	0.950	1.06	1.19	
8	1.00	0.825	1.11	0.811		8	0.947	0.975	1.00	1.06	.107	0.881	1.32	
16	1.00	.731	0.695	.846		16	1.47	1.20	1.00	0.823	0.698	1.63	1.78	
	$g^{(0)}$ (0.184, z)						$g^{(60)}$ (0.184, z)							

4.3. Other Comparisons

The penetration of radiation from a plane isotropic source can be determined through the superposition of results for plane monodirectional oblique sources. Good agreement has been found between the results of such a superposition and a direct calculation based on a polynomial expansion with the use of the appropriate plane isotropic moments. The ratio of the respective results for the total scattered energy flux at various distances from the source is shown in table 3.

As a further check, moment calculations were also carried out for singly-scattered radiation, which could be compared with the results of direct evaluations of the formulas of appendix A. Table 3 also contains sample results of such calculations; again, the agreement is good. It should be mentioned that the direct evaluation of the flux of singly-scattered radiation was rather laborious because of the necessary numerical integration. It would have been more expeditious, and would have involved only a minor loss of accuracy, to use moment-fitting making use of weight functions suggested by the exact analytical expressions or physical considerations.

TABLE 3. *Sample calculations to test the accuracy of the moment-fitting procedure*

z	A	B	C
0	0.922	----------	----------
0.5	.960	0.935	----------
1	1.09	.979	1.04
2	0.971	1.04	1.01
4	1.02	1.12	1.03
8	0.908	1.15	1.07

Ratio of results for singly-scattered flux from a monodirectional plane oblique source:

A: Moment calculation/direct calculation ($\alpha=0°$, $E=0.325$ Mev; weight function $L_{3/2}(z)$).

B: Moment calculation/direct calculation ($\alpha=90°$; $E=0.215$ Mev; weight function $E_4(z)$).

Ratio of results for scattered flux from plane isotropic source, $\int_0^{\pi} \sin\alpha d\alpha \int_0^{0.66} dE F^{(\alpha)}(E,z)$:

C: Superposition of plane oblique source results/direct calculation based on plane isotropic moments.

5. Appendix A. Singly-Scattered Radiation

Consider a photon emitted by a plane source at $z=0$, with energy E_0 and obliquity α. Assume that the photon travels to a depth s without interaction, undergoes a Compton scattering between s and $s+ds$ that changes its energy from E_0 to a value in the range $(E, E+dE)$, and crosses the z-plane with obliquity ω without further interaction. The probability for this contingency is

$$PdEds=\frac{K(E_0,E)}{\cos\alpha}\exp\left\{-\frac{\mu(E_0)s}{\cos\alpha}-\frac{\mu(E)(z-s)}{\cos\omega}\right\}U[(z-s)\cos\omega]dEds, \tag{A1}$$

where $\mu(E)$ is the narrow-beam linear total-absorption coefficient, $K(E_0, E)$ is the Klein-Nishina differential coefficient for Compton scattering with an energy change from E_0 to E, and $U(z)$ is the unit step function ($U=1$, if $z>0$; $U=0$, if $z<0$). According to the law of Compton scattering

$$\cos\omega=\cos\alpha\cos\left(1-\frac{mc^2}{E}+\frac{mc^2}{E_0}\right)+\sin\alpha\sin\left(1-\frac{mc^2}{E}+\frac{mc^2}{E_0}\right)\cos\varphi, \tag{A2}$$

where mc^2 is the electron rest energy, and φ is an azimuthal angle distributed uniformly between 0 and 2π.

In order to obtain the energy flux $F_1^{(\alpha)}(E,z)$ of singly-scattered radiation, one must multiply eq (A1) by E, integrate over all values of s between 0 and ∞ (assuming that $0\leq\alpha\leq\pi/2$), multiply the result by sec ω [7], and average over all possible azimuthal angles φ. With distances expressed in mean free paths of the primary radiation, the final result for the singly-scattered flux can be written

$$F_1^{(\alpha)}(E,z)=\frac{EK(E_0,E)}{\mu(E_0)\cos\alpha}e^{-(z/\cos\alpha)}\frac{1}{2\pi}\int_0^{2\pi}d\varphi H(z,E,\alpha), \tag{A3}$$

where

$$\begin{aligned} H(z,E,\alpha)&=\frac{1}{t\cos\omega}\{(e^{zt}-1)U(\cos\omega)-U(-\cos\omega)\} && (z>0)\\ &=-\frac{1}{t\cos\omega}e^{zt}U(-\cos\omega) && (z<0). \end{aligned} \tag{A4}$$

$$t=\frac{1}{\cos\alpha}-\frac{\mu(E)}{\mu(E_0)}\frac{1}{\cos\omega}.$$

The integral in eq (A3) has been evaluated numerically, except when $\alpha=0°$; in this case

$$\cos\omega=\cos\left(1-\frac{mc^2}{E}+\frac{mc^2}{E_0}\right), \tag{A5}$$

and the integration over φ is trivial.

6. Appendix B. Calculation of the Spatial Flux Moments

The following brief discussion of the moment equations is presented to make this paper self-contained. It will also bring out some minor points in which the procedure followed here differs in details from that given in the basic reference [1]. These are the use of an energy flux instead of a number flux, the separation of unscattered and singly-scattered flux, and the extension to plane sources with arbitrary angular distributions with cylindrical symmetry.

---

[7] Without the factor sec ω one would obtain an energy current across the z-plane instead of the energy flux through surface perpendicular to the direction of propagation of the radiation.

Let $F_k(z, \cos\theta, E)$ be the energy flux of photons that have been scattered k times. In terms of the F_k's, the transport equation has the form

$$\left.\begin{aligned}
&\frac{\partial F_k}{\partial z}\cos\theta+\mu F_0=S(z,E,\cos\theta)\\
&\frac{\partial F_k}{\partial z}\cos\theta+\mu F_k=\int_E^{E_0} dE'\,\frac{E}{E'}\,K(E',E)\cdot\\
&\qquad\int_0^{2\pi} d\varphi'\int_{-1}^{1} d\cos\theta'\,\frac{1}{2\pi}\,\delta\left(1-\frac{mc^2}{E}+\frac{mc^2}{E'}-\cos\theta\cos\theta'-\right.\\
&\qquad\left.\sin\theta\sin\theta'\cos\varphi'\right)F_{k-1}\qquad (k>0)
\end{aligned}\right\}\tag{B1}$$

where δ is the Dirac delta function, and S is the source function.

We shall consider a set of elementary source functions

$$S_L=E_0\delta(E-E_0)P_L(\cos\theta)\delta(z)\,\frac{2L+1}{4\pi}\qquad L=0,1,2,\ldots,\tag{B2}$$

where P_L is a Legendre polynomial. These elementary sources have no direct physical meaning except when $L=0$ but are convenient mathematical fictions.

We shall indicate the source type from which a given flux is derived by an index L.

We expand F_{kL} into a Legendre series in the angular variable and take spatial moments of the Legendre expansion coefficients; i. e., we introduce the transform

$$G_{kL}(n,l,E)=\int_{-\infty}^{\infty} dz\int_{-1}^{1} d\cos\theta\, z^n P_l(\cos\theta)\,F_{kL}(z,\cos\theta,E)\tag{B3}$$

and a similar transform for the source function

$$T_L(n,l,E)=\int_{-\infty}^{\infty} dz\int_{-1}^{2} d\cos\theta\, z^n P_l(\cos\theta)S_L(z,\cos\theta,E)=\frac{1}{2\pi}\,E_0\delta(E-E_0)\,\delta_{n0}\delta_{lL}.\tag{B4}$$

It follows from the transport eq (B1) and sundry properties of Legendre polynomials, that the transforms G_{kL} obey the equation

$$\left.\begin{aligned}
&(\Delta+\mu)G_{0L}=T_L &&(k=0)\\
&(\Delta+\mu)G_{kL}=\int_E^{E_0} dE\,\frac{E}{E'}\,K(E',E)P_l\left(1-\frac{mc^2}{E}+\frac{mc^2}{E'}\right)G_{k-1,L} &&(k>0),
\end{aligned}\right\}\tag{B5}$$

where Δ is an operator defined by the relation

$$\Delta G_{kL}(n,l,E)=n\,\frac{l+1}{2l+1}\,G_{kL}(n-1,l+1,E)+n\,\frac{l}{2l+1}\,G_{kL}(n-1,l-1,E).\tag{B6}$$

The transform of the multiply scattered flux is found by summation

$$H_1(n,l,E)=\sum_{k=2}^{\infty} G_{kL}(n,l,E).\tag{B7}$$

It follows from eq (B5) and (B7) that

$$(\Delta+\mu)H_L(n,l,E)=\int_E^{E_0} dE'\,\frac{E}{E'}\,K(E',E)P_l\left(1-\frac{mc^2}{E}+\frac{mc^2}{E'}\right)H_L(n,l,E')+T_L^*(n,l,E),\tag{B8}$$

where the source function

$$T_L^*(n,l,E)=\int_E^{E_0} dE' \frac{E}{E'} k(E',E) P_l\left(1-\frac{mc^2}{E}+\frac{mc^2}{E'}\right) G_{1L}(n,l,E'). \tag{B9}$$

The calculation thus proceeds as follows: One computes G_{0L} and G_{1L} with the use of eq (B5), then the source function according to eq (B9), and finally H_L according to eq (B7). The equation for G_{0L} is algebraic; all others are linear integral equations of the Volterra type, and are solved numerically on the NBS automatic computer (SEAC). The equations are interlinked, but the nature of the coupling operator Δ is such that they need not be solved simultaneously. Indicated below are the chains of equations that must be solved to calculate $H_L(n,l,E)$ or $G_{kL}(n,l,E)$; for the sake of brevity only the (n,l) values are shown.

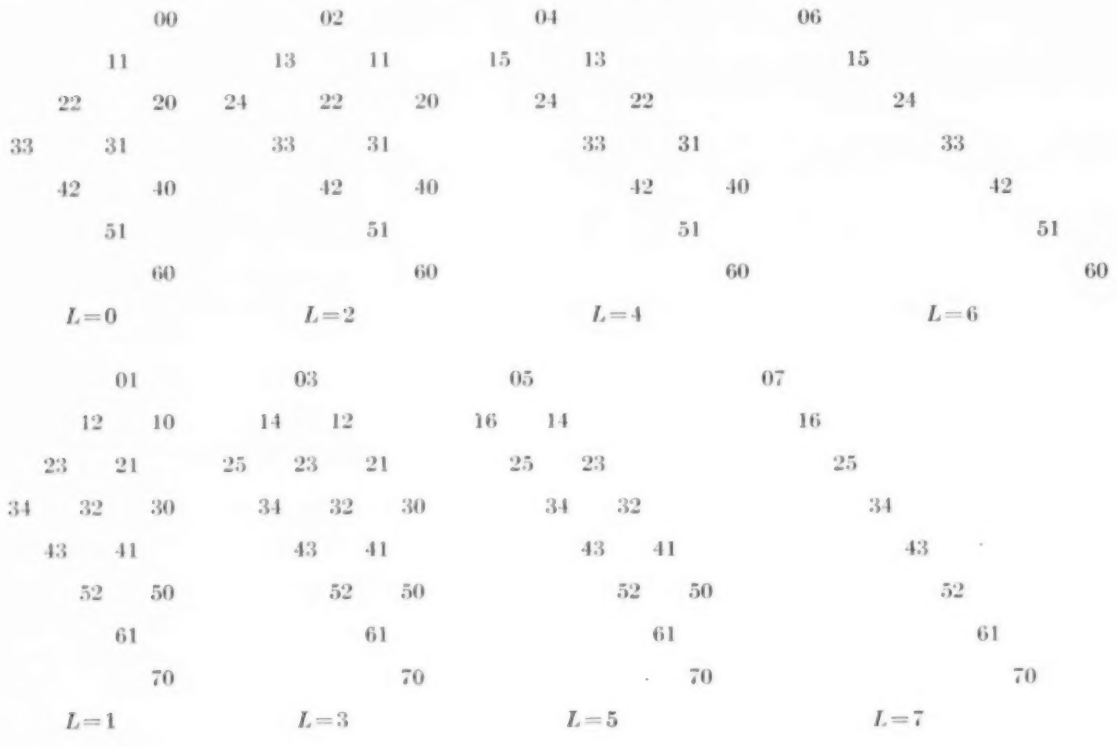

For example, in order to compute $H_0(4, 0, E)$, one must first calculate in turn the quantities $H_0(0, 0, E)$, $H_0(1, 1, E)$, $H_0(2, 2, E)$, and $H_0(3, 1, E)$.

It can be shown that

$$H_L(n,l,E)=G_{kL}(n,l,E)=0 \tag{B10}$$

unless $n-|L-l|$ is a nonnegative even integer.

Now consider a monoenergetic plane source with arbitrary distribution, expanded into a Legendre series:

$$S(z, \cos\theta, E)=E_0\delta(E-E_0)\delta(z)\sum_{L=0}^{\infty}\frac{2L+1}{4\pi} A_L P_L(\cos\theta). \tag{B11}$$

It follows from the linearity of the transport equation that the moments of the flux for such a source can be obtained through the addition of moments for "elementary" sources. Taking into account (B10), one finds that

$$\left.\begin{aligned}\overline{z^{2n}}(E)&=\sum_{L=0}^{n} A_{2L}H_{2L}(2n,0,E)\\ \overline{z^{2n+1}}(E)&=\sum_{L=0}^{n} A_{2L+1}H_{2L+1}(2n+1,0,E).\end{aligned}\right\} \tag{B12}$$

It is remarkable that in order to determine the first n even (odd) moments, one need specify the source only by its first n even (odd) expansion coefficients A_L.

Finally, we note that for a monodirectional source with angular part $\delta(\cos\theta-\cos\alpha)$,

$$A_L=P_L(\cos\alpha). \tag{B13}$$

7. Appendix C. Details of the Function-Fitting Procedure

For the solution of the moment eqs (9a, b) it is convenient to adopt the following notation:

$$\left.\begin{aligned}A_j&=\alpha_j B_j\frac{M_0}{m_0}\\ B_j&=\left[\frac{m_0}{m_2}\frac{M_2}{M_0}\beta_j\right]^{-1/2}\end{aligned}\right\}\quad(j=1,2) \tag{C1}$$

$$\left.\begin{aligned}C_j&=\gamma_j D_j^3\frac{M_1}{m_1}\\ D_j&=\left[\frac{m_1}{m_3}\frac{M_3}{M_1}\delta_j\right]^{-1/2}\end{aligned}\right\}\quad(j=1,2) \tag{C2}$$

Equations (9a, b) can then be written in the form

$$\left.\begin{aligned}\alpha_1+\alpha_2&=1\\ \alpha_1\beta_1+\alpha_2\beta_2&=1\\ \alpha_1\beta_1^2+\alpha_2\beta_2^2&=s\\ \alpha_1\beta_1^3+\alpha_2\beta_2^3&=t\end{aligned}\right\} \tag{C3}$$

$$\left.\begin{aligned}\gamma_1+\gamma_2&=1\\ \gamma_1\delta_1+\gamma_2\delta_2&=1\\ \gamma_1\delta_1^2+\gamma_2\delta_2^2&=\hat{s}\\ \gamma_1\delta_1^3+\gamma_2\delta_2^3&=\hat{t}\end{aligned}\right\} \tag{C4}$$

Equations (C3) and (C4) being formally the same, further discussion is confined to (C3). A solution can be obtained by a method given by Chandrasekhar [7]. Let

$$\omega_0=\frac{t-s^2}{s-1} \tag{C5}$$

$$\omega_1=\frac{s-t}{s-1} \tag{C6}$$

It follows from (C3) that β_1 and β_2 are the roots of the quadratic equation

$$\beta^2+\omega_1\beta+\omega_0=0, \tag{C7}$$

and that

$$\alpha_2=\frac{\beta_1-1}{\beta_1-\beta_2} \tag{C8}$$

$$\alpha_1=1-\alpha_2 \tag{C9}$$

B_1 and B_2 are real-valued if and only if β_1 and β_2 are real and positive. This requires that

$$\left.\begin{aligned}\omega_1&\leq 0\\ \omega_0&\geq 0\\ \omega_1^2-4\omega_0&\geq 0\end{aligned}\right\}. \tag{C10}$$

Equations (C5), (C6), and (C10) imply the following conditions on s and t:

If $0 \leq s \leq 1$, $0 \leq t \leq 1$, the allowed region lies between the parabola $s^2=t$, and the curve whose parametric representation is

$$\left.\begin{aligned} s &= \frac{1}{8}\{3+6u-u^2-[(3+6u-u^2)^2-64u]^{1/2}\} \\ t &= us \end{aligned}\right\} \qquad (C11)$$

$$(0 \leq u \leq 1)$$

If $s \geq 1$ and $t \geq 1$, the allowed region lies between the line $s=1$ and the parabola $s^2=t$.

The author expresses his gratitude to L. V. Spencer and U. Fano for helpful discussions and suggestions. He also is indebted to J. Doggett and J. Hubbell for their help with the numerical calculations.

8. References

[1] L. V. Spencer and U. Fano, J. Research NBS **46,** 446 (1951) RP2213.
[2] The most extensive set of such calculations is contained in: H. Goldstein and J. E. Wilkins, Jr., NDA Report 15C–41 (Nuclear Development Associates, White Plains, 1954).
[3] U. Fano, J. Research NBS **51,** 95 (1953) RP2439.
[4] This technique, as applied to diffusion problems, was first described by L. V. Spencer, Phys. Rev. **88,** 793 (1952).
[5] F. S. Kirn, R. J. Kennedy, and H. O. Wyckoff, Radiology **63,** 94 (1954).
[6] M. J. Berger and J. Doggett, J. Research NBS **56,** 89 (1956) RP 2653.
[7] S. Chandrasekhar, Radiative transfer, p. 59 (Oxford Press, 1950).

Washington, May 4, 1955.

Journal of Research of the National Bureau of Standards Vol. 56, No. 3, March 1956 Research Paper 2657

A Re-entrant Cavity for Measurement of Complex Permeability in the Very-High-Frequency Region

R. D. Harrington, R. C. Powell, and P. H. Haas

A re-entrant cavity, constructed for measuring the initial complex permeability of magnetic toroids in the very-high-frequency region, is described. Many of the electrical and mechanical problems associated with the development of an instrument of this type are considered. The general theory of permeability measurements, using a re-entrant cavity, is discussed, and the associated working equations are derived. Calibration techniques and results of measurements on several samples are also given.

1. Introduction

The increasing use of magnetic cores for high-frequency inductors and tuning applications has created a demand for information concerning the magnetic properties of materials in the very-high-frequency region. Research and production techniques are thus in need of a rapid and reasonably accurate method for measuring the initial complex permeability of toroidal samples in the region of 100 Mc.

Corresponding measurement problems in the frequency region below 30 Mc were solved at the National Bureau of Standards through the development of the radio-frequency permeameter [1].[1] Methods used in the analysis of the permeameter are not readily extended into the higher frequency ranges because it is well known that an accurate measurement of radio-frequency permeability in the VHF region requires distributed parameter systems. These techniques usually involve impedance measurements with coaxial lines or cavities containing a sample whose dimensions are small compared to the wavelength within it, and which is placed in a region of high magnetic field. When consideration is given to the study of permeability samples of very low loss, a cavity measurement is most readily utilized because of the attainable high Q of the instrument. For this reason, an investigation was undertaken for the development of a re-entrant resonant cavity for the measurement of initial complex permeability of toroids in the frequency range of 60 to 180 Mc. A schematic drawing of a re-entrant cavity of the type developed under this research program is shown in figure 1.

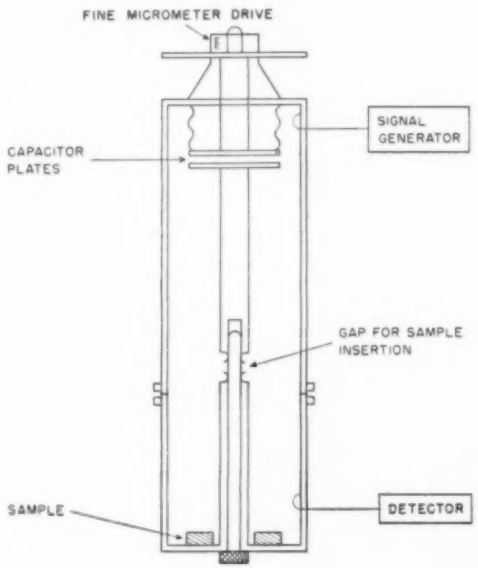

FIGURE 1. *Schematic drawing of re-entrant cavity for determining radio-frequency permeability of magnetic toroids.*

[1] Figures in brackets indicate the literature references at the end of this paper.

Cavities of this type have been constructed by other investigators [2, 3, 4], and as such the basic principles of these measurements are fairly well known. The design and analysis of the instrument developed at the National Bureau of Standards differs somewhat from these previous models. A description of the cavity and a brief discussion of the measurement methods and calibration techniques used in the determination of permeability with this instrument are given. Many of the electrical and mechanical problems that arise in the construction of a re-entrant cavity for magnetic measurements are discussed.

2. Description of Instrument

A re-entrant cavity is, essentially, a shorted section of coaxial transmission line with a lumped capacitance at one end, as can be seen in figure 1. The capacitor for the Bureau instrument consists of two parallel capacitor plates whose capacitance or separation distance can be adjusted by means of the vernier micrometer drive shown near the top of figures 1 and 2. The complex permeability of a sample is determined from a measurement of the variation in Q and the change in the resonant capacity of the cavity when a small toroidal sample is placed at the bottom of the instrument in a region of high magnetic field. It should be noted that measurements can also be obtained by holding the capacity fixed and determining the change in resonant frequency upon insertion of a sample [2]. However, this variation in frequency is quite small, and its measurement requires elaborate frequency-measuring equipment, such as counters or heterodyne systems. As an instrument was desired that

would give a fairly accurate permeability measurement for laboratory as well as production and quality control purposes, emphasis was placed on capacity-variation techniques that require only an oscillator and detector as associated equipment.

If the cavity is to cover a reasonably large frequency range, the tuning capacitance must be capable of a variation of the order of 10 or 20 to 1. However, to increase the frequency coverage further, the instrument was constructed in two lengths, as shown in figure 2. The longer instrument is used in the 60- to 110-Mc region, whereas the short cavity resonates in the 110- to 180-Mc region. The flange in the middle of the cavity facilitates the removal and interchange of the two bottom sections of different lengths. This makes it necessary to construct only one top unit, consisting of the capacitor plates and vernier unit.

In order to avoid making the unit excessively long, the maximum capacitance must be large if low frequencies are to be obtained. This capacitance was obtained on the National Bureau of Standards instrument by using capacitor plates 1.5 in. in diameter. Placing a toroid at the bottom of the cavity would require slipping it over these plates. This is undesirable as few representative cores have inside dimensions of 1.5 in. To insert the core through the bottom of the cavity would require removing some type of shorting plug in the bottom section of the instrument, which, in view of the need of a high reproducible Q, is impractical. That region of the cavity is, of course, a current maximum, and changes of resistance at the bottom cause large changes in cavity losses.

This problem was solved by using a hollow center conductor through which a copper rod could slide. A gap in the hollow conductor was placed at a considerable distance above the bottom of the cavity, and the center copper rod completed the circuit by making contact with beryllium-copper fingers on the inside of the hollow conductor. This opening in the center conductor may be seen in the lower window of the two cavities in figure 2 and, in more detail, in figure 3. A core may be inserted by removing the cap at the bottom of the cavity and withdrawing the copper rod. The sample is then placed on a small plastic platform held by nylon threads and

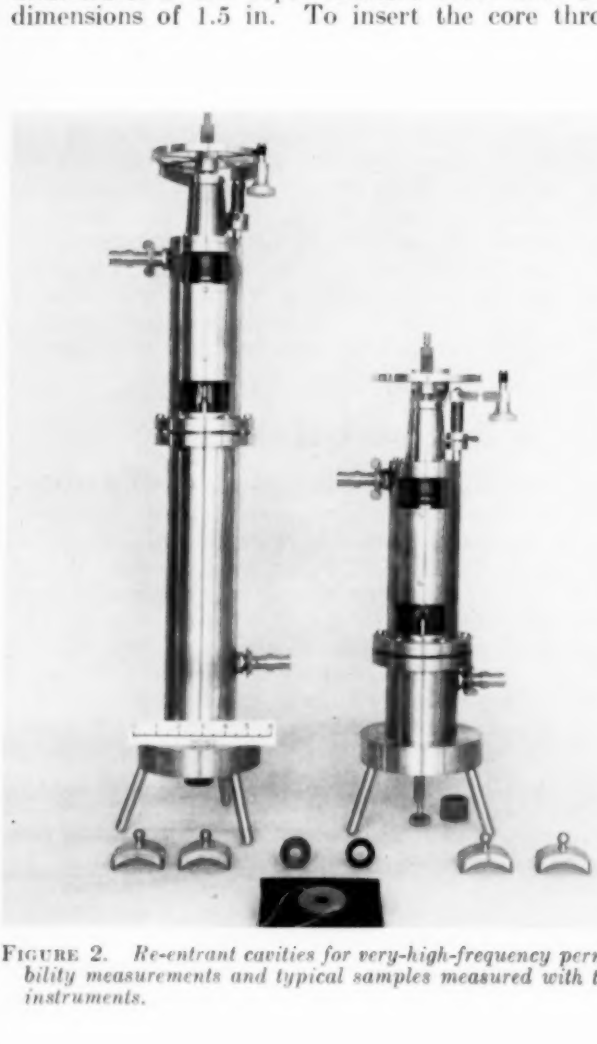

FIGURE 2. *Re-entrant cavities for very-high-frequency permeability measurements and typical samples measured with these instruments.*

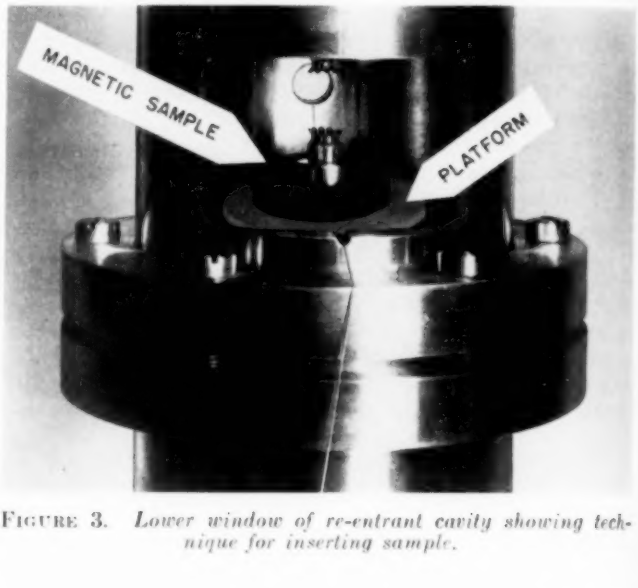

FIGURE 3. *Lower window of re-entrant cavity showing technique for inserting sample.*

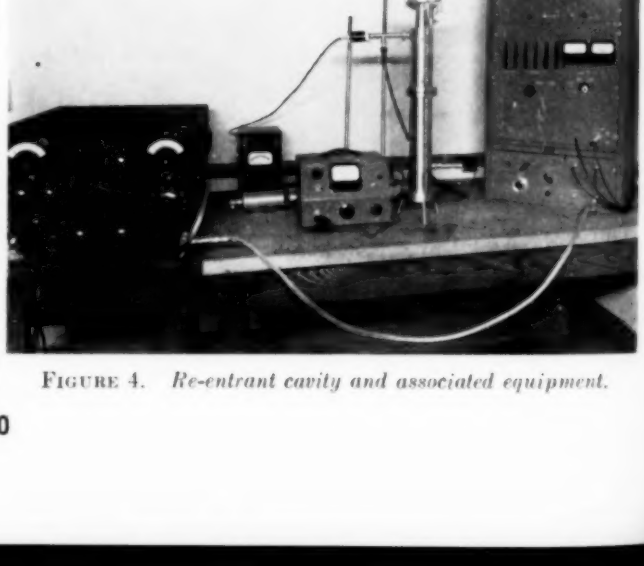

FIGURE 4. *Re-entrant cavity and associated equipment.*

lowered to the bottom of the cavity. This platform and a typical sample can be seen in figure 3. This method of sample insertion thus allows the center conductor to have a much smaller diameter than the condenser plates, and, of course, a more reproducible Q is obtained.

The capacitor plates can be seen in the top window of the cavities in figure 2. The removable window readily facilitates the cleaning and inspection of the condenser as the capacitance is quite sensitive to dust particles that may collect on the surfaces of the plates. The lower condenser plate is held in place by two dielectric slabs, and a bellows connection is made with the top plate in order to avoid any sliding contacts. The capacitor plates are lapped to within 0.0001 in. total indicator reading. The micrometer wheel can be read to 0.0001 in. directly and a vernier to 0.00001 in. This accurate dimensioning is necessary as small capacitance differences are used in the calculations. The calibration of the capacitor will be explained later.

Coupling to the cavity is obtained through two adjustable current loops. The input loop is located near the top of the cavity, and the pickup loop for the detector is placed a short distance above the sample, at the bottom of the instrument. Coupling must be loose in order that the input voltage and frequency remain unaffected as the cavity is tuned throughout the resonance curve. A $\frac{1}{32}$-amp fuse is used as a bolometer element in order to obtain a better square law characteristic than is possible with a crystal.

A typical equipment set up is shown in figure 4. A signal modulated with a 1,000-cps signal is passed through a filter and three-stub tuner. The input voltage is monitored with a vacuum tube voltmeter in order to assure loose coupling. The output is fed directly to a bolometer and amplifier. The frequency counter shown in the figure is used for calibration of the Q of the cavity. Once the Q calibration has been completed, the counter is no longer essential for a measurement and is removed from the circuit. The calibration details are given later.

3. Analysis

It has already been stated that a permeability measurement is based on the change in the inductive properties of the cavity when a sample is placed in a region of high magnetic field. The method is essentially a perturbation technique that enables one to disregard the effect of the dielectric constant of the specimen as long as the thickness of the sample is small compared to the wavelength within it. It should be noted that this situation is satisfied in the VHF region by many of the samples manufactured commercially. In all cases, however, one must still give consideration to the problems that may arise with certain samples because of dimensional resonance [5].

Consider the inner and outer radii of the internal volume of the coaxial section of the re-entrant cavity to be A and B, respectively. Let a, b, and h, respectively, be the corresponding inner radius, outer radius, and height of the sample being considered. If the thickness of the sample is small compared to the wavelength within it, and if the sample is placed against the shorted end of the cavity in a region of high magnetic field, one may consider the electric energy stored in the sample as negligible compared to the stored magnetic energy, and write for the latter quantity

$$U_{H1}=\frac{1}{2}(\mu'-1)L_a|I_1|^2 \tag{1}$$

where L_a is the geometrical or equivalent air inductance of a sample of permeability μ' and is given by $L_a=0.4606\ h\ \log_{10}\ (b/a)\times 10^{-6}$ henries, where h is in meters. I_1 is the current flowing in the vicinity of the sample and is essentially constant over the distance h.

If we similarly consider the annular region of the empty cavity of radii A and B and height Δl located at the shorted end of the instrument, where Δl is sufficiently small, so that the electric energy in this region is also negligibly small, then one may write for the stored magnetic energy for this case

$$U_{H2}=\frac{1}{2}\frac{\mu_0}{2\pi}ln\frac{B}{A}|I_1|^2\Delta l, \tag{2}$$

as the inductance per unit length of a uniform coaxial transmission line is given by

$$L=\frac{\mu_0}{2\pi}ln\frac{B}{A},$$

where μ_0 is the permeability of free space.

It can be seen that there will be some value of Δl for which $U_{H1}=U_{H2}$. By equating eq (1) and (2), this value of Δl is found to be

$$\Delta l=(\mu'-1)\frac{2\pi L_a}{\mu_0 ln\frac{B}{A}} \tag{3}$$

This equation essentially relates the effect of inserting a sample of permeability μ' into a region of high magnetic field in the cavity to a virtual change in length, Δl, of the instrument where both the sample thickness and Δl are small compared to the wavelength being considered.

This change may be transformed into a corresponding change in the lumped capacitance, C, located a distance, l, from the short by means of the approximate relation describing a short-circuited high-Q transmission line with a lumped capacitance at one end, which is given by

$$Z_0\tan\beta l=\frac{1}{\omega C}, \tag{4}$$

where

Z_0=characteristic impedance of the cavity considered as a coaxial transmission line

$\beta=2\pi$/wavelength

ω=angular frequency.

Holding the frequency constant and differentiating, we obtain

$$dl=-\frac{\omega Z_0}{\beta}\sin^2\beta l dC.$$

Substituting the value of Δl found in eq (3) for dl in the above equation, we get

$$(\mu'-1)\frac{2\pi L_a}{\mu_0 \ln\frac{B}{A}}=-\frac{\omega Z_0}{\beta}\sin^2\beta l dC.$$

Solving for $\mu'-1$ and using the expression for the characteristic impedance of a coaxial transmission line $Z_0=(1/2\pi)\sqrt{\mu_0/\epsilon_0}\ln(B/A)$, where ϵ_0 is the permittivity of free space, we obtain

$$\mu'-1=-\frac{dC}{k_2 L_a}, \tag{5}$$

where

$$k_2=(Z_0^2\sin^2\beta l)^{-1}.$$

The above relation gives the real permeability in terms of dC, which is the change in capacity necessary to reresonate the cavity upon insertion of the sample. The evaluation of k_2 is explained later.

The working equation for the measurement of the imaginary part of the permeability (μ'') may be obtained directly from an analysis of the energy associated with the magnetic field in the cavity. If the usual relations for the magnetic field energy stored, as well as that dissipated per cycle in both the cavity and the sample are substituted in the corresponding expression for the Q of the loaded cavity, a relation is obtained that readily leads to the expression [2]

$$\mu''=\frac{1}{Q_c}\left[(\mu'-1)\frac{Q_c}{Q_F}+\frac{k_1}{L_a}\left(\frac{Q_c}{Q_F}-1\right)\right], \tag{6}$$

where

$$k_1=\frac{Z_0[\frac{1}{2}\sin 2\beta l+\beta l]}{2\omega}, \tag{7}$$

and

Q_c=quality factor of empty cavity

Q_F=quality factor of cavity plus sample.

For a high-Q loaded cavity, the ratio of Q's may be replaced by the corresponding voltage ratio $Vr=V_c/V_F$, which is the ratio of the voltage output of the empty cavity to the output of the loaded cavity. Thus, the equation for μ'' is given by

$$\mu''=\frac{1}{Q_c}\left[(\mu'-1)Vr+\frac{k_1}{L_a}(Vr-1)\right]. \tag{8}$$

We therefore see that once $\mu'-1$ has been determined for a specimen, the only additional information necessary for calculating the magnetic loss is the voltage ratio Vr, the Q of the unloaded cavity, and the value of the quantity k_1, which is discussed shortly.

[2] See appendix.

4. Calibration of Cavity

The re-entrant cavity is calibrated directly against the primary standard of Radio-Frequency Permeability at the National Bureau of Standards, which is a precision variable-length coaxial line. There are essentially four quantities on the re-entrant cavity that require calibration.

1. The vernier micrometer drive, which must be calibrated in terms of capacitance.
2. The quantity k_2 in eq (5), which determines the real part of the permeability.
3. The value of k_1 in eq (8), which is the working equation for the magnetic loss measurement.
4. The Q of the unloaded cavity.

It is not necessary to have a calibration curve for Q if a frequency counter or similar instrument is readily available. However, as previously mentioned, it is preferred that measurements be obtained without relying on frequency-measuring instruments.

Consider first the capacitance calibration. The vernier micrometer could be evaluated in terms of the calculated capacitance between the condenser plates. However, the effects of fringing capacitance must not be neglected. The capacitor is thus calibrated at 1,000 cps, using extremely sensitive capacitance standards. This is done by removing the lower door in the cavity and opening the center conductor circuit by withdrawing the removable copper rod. The lower capacitor plate is now isolated from the body of the cavity and held in place by dielectric disks. The lower end of that portion of the center conductor in contact with the bottom capacitor plate may be seen in the lower window of the cavity in figures 2 and 3. An external wire connection may be made with the lower capacitor plate at this point. The upper capacitor plate is in contact with the body of the cavity. It is thus possible to connect the variable capacitor on the cavity in parallel with a precision variable capacitance standard. This parallel arrangement is placed across one arm of a capacitance bridge, and increments of capacitance in the cavity capacitor are compared directly with corresponding increments in the standard capacitor. The calculated capacitance of the variable capacitor in the cavity for a plate separation larger than that usually encountered in measurements is taken as a reference level. The exact location of this reference point is somewhat arbitrary as one is concerned only with differences in capacitance in this instrument. The above data enables a curve of capacitance versus vernier distance to be obtained; however, the capacitance covers a rather large range, which makes it difficult to obtain a precise graph. This difficulty is avoided by plotting only corrections to the calculated capacitance, which is obtained from the formula

$$C=\frac{\epsilon_0 A}{d},$$

where ϵ_0 is the permittivity of free space, and A and d are the cross-sectional area and separation distance, respectively, of the capacitor plates.

The expressions for the quantities k_1 and k_2 have already been given, but are repeated below:

$$k_2=(Z_0^2 \sin^2 \beta l)^{-1} \tag{9}$$

$$k_1=\frac{Z_0\left[\frac{1}{2}\sin 2\beta l+\beta l\right]}{2\omega}. \tag{10}$$

In order to evaluate these quantities, Z_0 is first calculated from the usual expression for the characteristic impedance of a coaxial transmission line ($Z_0=138 \log_{10}(B/A)$, where B and A are the outer and inner radii of the cavity). The value of the capacitance between the electrodes is then obtained at a low frequency, where the electrode separation is small and the resulting capacitance large enough to account for most of the cavity capacitance. Equation (4) is then used with the above values of Z_0 and C to calculate a value of l, the effective length of the cavity. A theoretical curve of k_2 and k_1 versus frequency may now be obtained. The operating eq (5) and (8) are solved for k_1 and k_2 in terms of μ', μ'', dC, Q_c, and Vr. The μ' and μ'' are obtained from a measurement of a sample in the primary standard. The remaining quantities dC, Q_c, and Vr are obtained from a measurement of the same sample, using the re-entrant cavity. This data is obtained at one frequency for each of the two different length cavities. The resulting experimental values of k_1 and k_2 are then used to adjust the theoretical values. It can be seen that this procedure gives an effective value for the characteristic impedance of the cavity.

The Q of a resonant circuit may be obtained from either of the relations

$$Q=\frac{f_0}{\Delta f}=\frac{2C_0}{\Delta C}, \tag{11}$$

where f_0 and C_0 are the resonant frequency and total effective capacity, and Δf and ΔC are corresponding 3-db band widths. In the case of a distributed parameter system such as a cavity, the total effective capacitance cannot be calculated. Thus, the frequency relation is more meaningful.

However, the Q of a cavity is quite sensitive to temperature variations, and a more accurate answer is obtained if the Q could be obtained at the time of each measurement instead of using one original calibration of Q versus frequency. In order that only capacitance variations be necessary for a measurement, it was decided to make an initial measurement of Δf, f_0, and ΔC. Equation (11) can then be used to calculate $2C_0$, which may be plotted as a calibration curve. Any future determination of Q may then be obtained from the calibration curve and a measurement of ΔC.

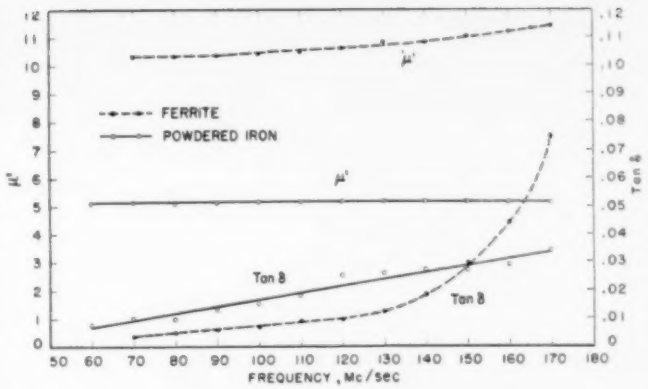

FIGURE 5. *Typical data obtained with re-entrant cavity, using two different samples.*

5. Measurements and Results

The cavity was normalized against the primary standard by using a sample having a permeability in the order of 8, which is a typical value for several samples in this frequency range. A comparison of results obtained at 130 Mc, using three samples measured in the primary standard and re-entrant cavity, are shown in table 1.

TABLE 1. *Comparison of results, using a re-entrant cavity and primary standard at 130 Mc*

Sample	Primary standard		Re-entrant cavity	
	μ'	$\tan\delta=\frac{\mu''}{\mu'}$	μ'	$\tan\delta$
1	8.102	0.067	8.119	0.065
2	10.645	.090	10.768	.083
3	5.08	.027	5.16	.034

A typical curve of permeability versus frequency, using the re-entrant cavity, is shown in figure 5 for a powdered-iron sample and a ferrite.

The above data and curves show the instrument to be capable of good precision and fairly accurate results. This conclusion, along with the simple measurement procedure, gives strong support to the use of a re-entrant cavity for very-high-frequency permeability measurements.

6. References

[1] P. H. Haas, A radio frequency permeameter, J. Research NBS **51**, 221 (1953) RP2454.

[2] H. J. Lindenhovius and J. C. van der Breggen, The measurement of permeability and magnetic losses of non-conducting ferromagnetic material at high frequencies, Philips Research Reports **3**, 37–45 (Feb. 1948).

[3] D. Polder, Ferrite materials, Proc. Inst. Elec. Engrs. (London), **97II**, 246–256 (1950).

[4] C. M. van der Burgt, M. Gevers, and H. P. J. Wijn, Measuring methods for some properties of ferroxcube materials, Philips Tech. Rev. **14**, 245–280 (March 1953).

[5] Brochman, Dowling, and Steneck, Dimensional effects resulting from a high dielectric constant found in a ferromagnetic ferrite, Phys. Rev. **77**, 85–93 (Jan. 1950).

7. Appendix. Derivation of Loss Equation

Definition of terms:

V = volume of cavity including space occupied by sample.
v = volume of sample.
Ec_1 = total energy stored in volume $V-v$.
Es_1 = total energy stored in space occupied by sample of volume v.
Ec_2 = energy dissipated per cycle in cavity without sample.
Es_2 = energy dissipated per cycle in space occupied by sample of volume v.
A, B, l = inner radius, outer radius, and length of cavity.
a, b, h = inner radius, outer radius, and height of sample.
t = length measured along axis of cavity or sample.
r = radial distance measured in cavity or sample.
β = phase constant in cavity.
$Q_c = Q$ of empty cavity.
$Q_s = Q$ of sample.
$Q_F = Q$ of cavity plus sample.

The Q of the loaded cavity may be written

$$Q_F = 2\pi \frac{Ec_1 + Es_1}{Ec_2 + Es_2}. \tag{12}$$

Let

$$H = \frac{H_0}{r} \cos \beta t,$$

where H is the magnetic field at a distance t from the shorted end of the cavity.

If we assume the thickness of a sample is small compared to the wavelength within it, then we may consider $\cos\beta t$ as being essentially unity over the dimensions of the sample, as the sample is always located at the shorted end of the instrument.
Thus

$$Ec_1 = \frac{\mu_0}{2}\int_V \frac{H_0^2}{r^2}\cos^2 \beta t dV - \frac{\mu_0}{2}\int_v \frac{H_0^2}{r^2} dv$$

$$= \pi\mu_0 H_0^2 \left[\frac{1}{\beta}\left(\ln\frac{B}{A}\right)\left(\frac{1}{2}\beta l + \frac{1}{4}\sin 2\beta l\right) - h \ln\frac{b}{a}\right] \tag{13}$$

$$Es_1 = \frac{\mu_0}{2}\int_v \frac{\mu' H_0^2}{r^2} dv = \pi\mu_0 H_0^2 \mu' h \ln\frac{b}{a} \tag{14}$$

$$Ec_2 = \frac{2\pi}{Q_c}\left(\frac{\mu_0}{2}\int_V \frac{H_0^2}{r^2}\cos^2 \beta t dV\right), \tag{15}$$

and

$$Es_2 = \frac{2\pi Es_1}{Q_s}. \tag{16}$$

Let

$$K = \left(\frac{1}{2}\beta l + \frac{1}{4}\sin 2\beta l\right).$$

Substituting the above values in eq (12), we obtain

$$Q_F = \frac{\frac{1}{\beta}\left(\ln\frac{B}{A}\right)K - \ln\frac{b}{a}h + \mu'\left(\ln\frac{b}{a}\right)h}{\frac{1}{Q_c\beta}\ln\frac{B}{A}K + \mu'\frac{1}{Q_s}\ln\frac{b}{a}h}.$$

Solving for $\mu'' = \mu'/Q_s$, we get

$$\mu'' = \frac{1}{\beta h}\frac{\ln\frac{B}{A}}{\ln\frac{b}{a}}\frac{K}{Q_F} + (\mu' - 1)\frac{1}{Q_F} - \frac{1}{Q_c\beta h}\frac{\ln\frac{B}{A}}{\ln\frac{b}{a}}K$$

$$\mu'' = \frac{1}{Q_c}\left[(\mu' - 1)\frac{Q_c}{Q_F} + \frac{1}{\beta h}\frac{\ln\frac{B}{A}}{\ln\frac{b}{a}}K\left(\frac{Q_c}{Q_F} - 1\right)\right]. \tag{17}$$

Now

$$\beta = \omega\sqrt{\mu_0\epsilon_0}.$$

The geometrical inductance of the sample is

$$L_a = \frac{\mu_0}{2\pi}\left[\ln\frac{b}{a}\right]h.$$

The characteristic impedance of the cavity is

$$Z_0 = \frac{1}{2\pi}\sqrt{\frac{\mu_0}{\epsilon_0}}\ln\frac{B}{A}.$$

Thus

$$\frac{1}{\beta h}\frac{\ln\frac{B}{A}}{\ln\frac{b}{a}} = \frac{1}{\omega\sqrt{\mu_0\epsilon_0}}\frac{2\pi Z_0\sqrt{\frac{\epsilon_0}{\mu_0}}}{2\pi\frac{L_a}{\mu_0}} = \frac{Z_0}{\omega L_a}.$$

Substituting in eq (17)

$$\mu'' = \frac{1}{Q_c}\left[(\mu' - 1)\frac{Q_c}{Q_F} + \frac{Z_0 K}{\omega L_a}\left(\frac{Q_c}{Q_F} - 1\right)\right]. \tag{1}$$

Letting

$$k_1 = \frac{Z_0 K}{\omega} = \frac{Z_0}{2\omega}\left(\frac{1}{2}\sin 2\beta l + \beta l\right),$$

we obtain eq (6)

$$\mu'' = \frac{1}{Q_c}\left[(\mu' - 1)\frac{Q_c}{Q_F} + \frac{k_1}{L_a}\left(\frac{Q_c}{Q_F} - 1\right)\right].$$

Boulder, October 11, 1955.

Journal of Research of the National Bureau of Standards Vol. 56, No. 3, March 1956 Research Paper 2658

Fundamental Factors Controlling Electrical Resistivity in Vitreous Ternary Lead Silicates

Simon W. Strauss,[1] Dwight G. Moore, William N. Harrison, and Lloyd E. Richards

The resistivities of selected vitreous ternary lead silicates containing ions of groups I, II, III, IV, and also the ions chromium, manganese, iron, cobalt, and nickel were measured in the range 200° to 500° C and at an applied direct-current field of 525 volts per centimeter. In addition, the resistivities of vitreous silica and of quartz, with optic axis parallel and perpendicular to the applied field, were measured over the same temperature range. The resulting data are given as log resistivity-composition isotherms for the alkalies and alkaline earths and as log resistivity-temperature curves for the other ions. Correlations between resistivity and bonding energy and between frequency factor and heat of activation are presented. The resistivities of the alkali lead silicates were interpreted from the standpoint of the activation energy principle.

1. Introduction

Studies of the high-temperature electrical resistivities of ceramic coating materials have become important from the standpoint of both theory and technology. The current investigation was an outgrowth of a project begun in 1951. At that time a request had been received from Army Ordnance to develop a high temperature, electrically insulating ceramic coating suitable for the replacement of the more strategic natural sheet mica in special electronic components which must operate at elevated temperatures. A literature survey revealed that conduction in vitreous silicates was believed to be caused mostly by the migration of alkali ions. Using this information as well as some empirical considerations, a number of alkali-free, high-resistivity ceramic coatings were developed. A paper discussing some of the results was published [1] [2] and the data showed that ceramic coatings merit serious consideration in the field of high-temperature electrical insulation.

Although the ceramic coatings that were developed and tested proved suitable for a specific application, it was thought that a thorough study of fundamental factors controlling electrical resistivity in simple glass systems should be undertaken, to provide knowledge that could be applied not only in the design of ceramic coatings for use as high-temperature insulation, but also in the elucidation of the conduction mechanism. With these objectives in mind, a fundamental study was begun in 1952 under the sponsorship of the Office of Ordnance Research. This report covers the first phase of the study.

2. Review of Conduction Theory in Glasses

Investigations of the electrical properties of vitreous silicates were made as early as 1854 [2,3]. Seddon, Tippet, and Turner [4] have summarized the status in this field of study up to 1932. More recent ideas regarding the conduction mechanism have been presented in articles by Morey [5], Murphy and Morgan [6], Stevels [7], Stanworth [8], and Eitel [9].

It is generally agreed by these investigators that conduction in glasses is ionic. It has been established that the electrical conductivity of a soda-lime-silica glass, at room temperature and up to the strain point,[3] is essentially the result of transport of sodium ions, which are believed to migrate through the interstitial positions in the silicate network. In this temperature region the mobility of the calcium ion is considered to be negligible. The thermal energy is thought to be sufficient to detach a sodium ion from its interstitial position and cause it to move to a neighboring position [10]. As long as no external field is applied, the probability of such migration is equal in all directions. However, in the presence of an imposed field the sodium ions will show a tendency to move with the direction of the field, thus causing an electric current. The sodium ion has either a lower charge or a smaller radius than the other network modifiers [4] in a glass, with the exception of lithium; for this reason its movement through the lattice may be less restricted. Nevertheless, at sufficiently high temperatures the other network modifiers are said to contribute to the conductivity [7]. Relatively few systematic studies have heretofore been made on the conduction of simple glasses at temperatures exceeding 200° C. Moore and DeSilva [11] studied the electrical properties of ternary and quaternary alkali lime glasses at temperatures up to 320° C, and Gehlhoff and Thomas [12] measured electrical conduction of ternary soda silicates at temperatures up to 400° C. The purpose of the present investigation was to provide information which might contribute to a better understanding of the conduction process in silicate structures.

[1] Present address, Naval Research Laboratory, Washington, D. C.
[2] Figures in brackets indicate the literature references at end of this paper.

[3] Lillie, J. Am. Ceram. Soc. [3] **37**, 117 (1954), recommended the strain point to be defined as that temperature at which the data from the annealing point test, when plotted logarithmically against temperature, extrapolate to a viscosity of $10^{14.5}$ poises.
[4] Network modifier ions usually occupy the interstitial positions in the glassy structure.

3. Selection of Compositions

One of the objectives of the current investigation was to study the composition dependency of electrical resistivity of ceramic coating materials. It appeared that a logical approach was to select a simple silicate system for initial experimentation, and then to increase the complexity of the system by the gradually increasing partial replacement of one component ion at a time by other ions. In selecting a base composition, the system chosen should have a high solubility for various oxides and should yield workable glasses. Careful consideration of these and other problems involved, resulted in the selection of $PbO:SiO_2$ as the base composition. In a given composition series, increasing amounts of lead oxide were replaced by one of the other oxides.

The structure of a glass may be modified considerably if the composition is changed over a wide range even if the same constituents are used throughout. To avoid such structural changes, the specimens were composed according to the formula $xMeO:(1-x)PbO:SiO_2$. The value of x ranged from 0 to 0.4 for the alkali and alkaline earth ions and for iron, cobalt, and nickel and was fixed at 0.4 for the other ions. The 0.4 mole replacement was selected because this was the maximum concentration for glass formation for some of the oxides, and volatilization losses could be kept to reasonable values. Equivalent replacement was used so as to keep a constant ratio of Si/O and thus avoid any structural changes which might be caused by changes in the Si/O ratio.

Resistivity measurements were made on quartz and silica glass and also on complex lead silicates in which part of the lead oxide was replaced by oxides of lithium, sodium, potassium, rubidium, cesium, beryllium, magnesium, calcium, strontium, barium, zinc, cadmium, boron, aluminum, lanthanum, titanium, germanium, zirconium, cerium, thorium, chromium, manganese, iron, cobalt, and nickel. The compositions of these glasses are given in table 1.

4. Materials and Preparation of Specimens

All glasses were prepared from reagent grade chemicals (oxides, nitrates, carbonates, or oxalates); the source of silica was quartz crystals pulverized to pass a US Standard No. 40 sieve. Each raw batch was mixed intimately and ground in a mortar until all of the powdered material passed through a No. 40 sieve. The batches were melted in platinum crucibles placed in an electric furnace. Each melt was periodically stirred with a platinum rod to aid in the elimination of occluded gases and to produce a homogeneous glass. Test specimens were cast in a steel mold in the shape of a disk, 1½ in. in diameter by about ¼ in. thick. The disk, after casting, was transferred to a preheated ceramic mold and was then placed in an annealing furnace where it was allowed to cool overnight. After cooling, the disk was ground flat on a grinding lap using SiC No. 150 and No. 320 as abrasives, and the thicknesses measured to the nearest 0.0001 in.

TABLE 1. *Batch compositions of ternary lead silicates containing elements of groups I, II, III, and IV, and chromium, manganese, iron, cobalt, and nickel*

Composition No.	Oxide added	Amount of oxide	PbO	SiO_2
		Moles	*Moles*	*Moles*
1	Li_2O	0.01	0.99	1.0
2	Li_2O	.10	.90	1.0
3	Li_2O	.20	.80	1.0
4	Li_2O	.30	.70	1.0
5	Li_2O	.40	.60	1.0
6	Na_2O	.01	.99	1.0
7	Na_2O	.10	.90	1.0
8	Na_2O	.20	.80	1.0
9	Na_2O	.30	.70	1.0
10	Na_2O	.40	.60	1.0
11	K_2O	.01	.99	1.0
12	K_2O	.10	.90	1.0
13	K_2O	.20	.80	1.0
14	K_2O	.30	.70	1.0
15	K_2O	.40	.60	1.0
16	Rb_2O	.40	.60	1.0
17	Cs_2O	.40	.60	1.0
18	BeO	.40	.60	1.0
19	MgO	.01	.99	1.0
20	MgO	.10	.90	1.0
21	MgO	.20	.80	1.0
22	MgO	.30	.70	1.0
23	MgO	.40	.60	1.0
24	CaO	.01	.99	1.0
25	CaO	.10	.90	1.0
26	CaO	.20	.80	1.0
27	CaO	.30	.70	1.0
28	CaO	.40	.60	1.0
29	SrO	.01	.99	1.0
30	SrO	.10	.90	1.0
31	SrO	.20	.80	1.0
32	SrO	.30	.70	1.0
33	SrO	.40	.60	1.0
34	BaO	.01	.99	1.0
35	BaO	.10	.90	1.0
36	BaO	.20	.80	1.0
37	BaO	.30	.70	1.0
38	BaO	.40	.60	1.0
39	ZnO	.40	.60	1.0
40	CdO	.40	.60	1.0
41	B_2O_3	.133	.60	1.0
42	Al_2O_3	.133	.60	1.0
43	La_2O_3	.133	.60	1.0
44	TiO_2	.20	.60	1.0
45	GeO_2	.20	.60	1.0
46	ZrO_2	.20	.60	1.0
47	CeO_2	.20	.60	1.0
48	ThO_2	.20	.60	1.0
49	Cr_2O_3	.133	.60	1.0
50	FeO	.40	.60	1.0
51	CoO	.40	.60	1.0
52	NiO	.40	.60	1.0
53	MnO	.40	.60	1.0

Specimens were prepared for test by spraying a thin layer of "silver paint"[5] onto each face. A template was used during the spraying to leave an exposed circular area of silver ¾ in. in diameter evenly centered on each face of the specimen. The paint was cured by air drying at room temperature for several hours. The resulting silver contacts were smooth and continuous before and after test. Results of a previous investigation [1] had shown that resistivity of alkali borosilicate and alkali-free borosilicate ceramic coatings appeared to be independent of thickness. It was therefore assumed that the contact resistance was small in comparison to the resistance of the specimen.

[5] A term applied to a preparation used for decorative purposes in the ceramic industry and more recently in making printed circuits; after curing, it consists of nearly pure silver.

5. Chemical Analyses

Several of the glasses were analyzed chemically. The compositions were chosen to represent high, intermediate, and low resistivity glasses. A comparison between the compositions calculated from the batch materials used and the compositions as determined analytically is given in table 2.

TABLE 2. *Chemical analysis of ternary lead silicates prepared by the equivalent substitution of beryllium, manganese, cobalt and zinc oxide for lead oxide in* $PbO:SiO_2$

Composition	Weight percent [a]			Weight percent		
	Oxide	Calculated	Found	Oxide	Calculated	Found
18	BeO	4.9	4.3	PbO	65.6	65.7
39	ZnO	14.4	14.4	PbO	59.1	59.3
53	MnO	12.8	12.1	PbO	60.2	60.5
51	CoO	13.4	11.8	PbO	59.8	59.5

[a] Chemical analysis performed in the analytical laboratory of the Mineral Products Division under the supervision of L. Bean. The silica content was assumed to remain constant and was not determined.

6. Test Equipment and Procedure

A photograph of the equipment used for determining the resistivity of the specimens is shown in figure 1. The furnace, A, had a heating element consisting of Nichrome wire wound on a ceramic core. Within the core were located two circular stainless steel electrodes ¾ in. in diameter. An iron-constantan thermocouple was embedded in the top electrode, and the control thermocouple was embedded in the insulation. This second thermocouple activated the temperature control unit, B. The temperature of the top electrode was determined by the use of a potentiometer, F. A recording potentiometer, E, was used with a preamplifier, D, to graph the current passing through the specimen, in ranges 10^{-6} to 10^{-11} amp. An Ayrton shunt, C, was used in the input to the preamplifier to extend the range of the recorder to 10^{-3} amp. The resistance of the preamplifier input was 1,000 ohms.

The specimen to be tested was placed in the furnace so that the stainless steel electrodes were in contact with the silvered area on either side of the coated specimen (figs. 1 and 2). The furnace was heated at the rate of about 10 deg C per min and the current through the specimen was measured at 10 deg C intervals. The voltage was applied during the entire heating period, polarity being reversed at least once each 20 deg C. All determinations were made on at least triplicate specimens, one at a time. The current through the specimen was measured in amperes and the resistivity (ohm-cm) calculated from the current, voltage, and dimensions of the specimen. When the voltage drop across the shunt exceeded 1 percent of the input voltage or 2 v, this voltage drop was taken into consideration in calculating the resistivity. Edge effects were not included in calculating the effective area of the specimen because of the general inaccuracy in this type of measurement. The silvered area was assumed to be the effective area. In this type of measurement where the resistivity values are high, a 100-percent difference between duplicate determinations may be obtained. The precision was found to be, in general, of this order of magnitude or better. Above about 200° C the same values for the current were obtained with and without use of a guard ring. The surface conduction was therefore assumed to be negligible above 200° compared to that of the volume.

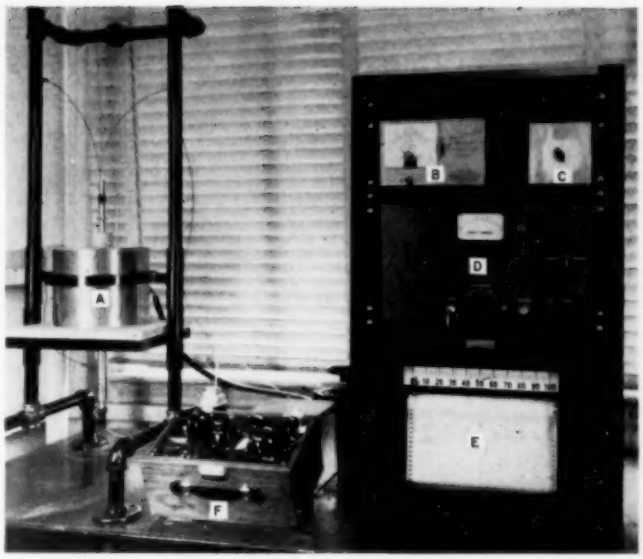

FIGURE 1. *Testing arrangement for the measurement of electrical resistivity of ceramic coating materials at elevated temperatures.*

A, Furnace; B, temperature control unit; C, Ayrton shunt; D, d-c amplifier; E, recording potentiometer; F, potentiometer.

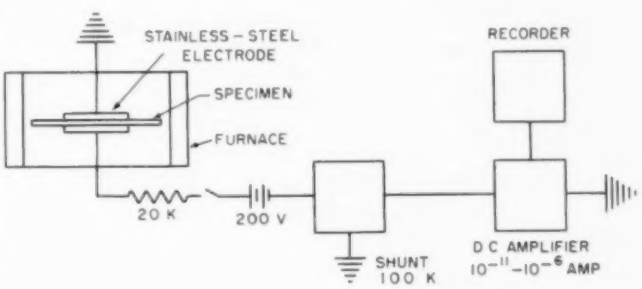

FIGURE 2. *Testing arrangement for the measurement of electrical resistivity of ceramic coating materials at elevated temperatures.*

The effect of polarization was directly observable in the values of current before and after reversal of the direction of flow through the specimen. In a specimen containing 0.4 mole of sodium, where polarization effects must be expected to be high, a maximum difference of about 6 percent was observed on reversal at the highest temperatures above about 300° C. This level of error introduces no observable error into the activation energies calculated from these data, and has therefore been ignored.

7. Results and Discussion

7.1. Silica Glass and Quartz

A comparison between the resistivity of silica glass and quartz is given in figure 3. These experiments were performed, (a) to measure the resistivity of silica glass because it is one end member of the $PbO:SiO_2$ system, and (b) to compare the resistivity of two allotropic forms of silica in order to obtain information regarding the conduction mechanism.

The observed conduction through both quartz and silica glass might well be due, in part at least, to the presence of traces of impurities since a trace of impurity would yield many potential conduction ions. For example, an impurity of one part sodium per billion of silica would be equivalent to about 10^{13} sodium ions per gram of silica. The results of spectrochemical analyses (table 3) indicate that each gram of silica glass or quartz actually contained 10^{15} to 10^{19} ions of various impurities. While these ions would seek the lowest available potential energy holes in the silicate structure, it is quite conceivable that at least some of them might still contribute towards electrical conduction, especially at higher temperatures. Warburg and Tegetmeier [13] reported that when a quartz specimen was electrolyzed, sodium amalgam being used as the anode, sodium migrated through the specimen in amounts in accordance with Faraday's law, while the weight of the specimen remained unchanged. These investigators concluded from this result and from additional experiments that the conduction was due to the presence of sodium silicate in the quartz; their analysis showed 1 part in 2,300, hence the quartz was regarded as a very dilute solution of sodium silicate.

As shown in figure 3, the resistivity of quartz measured perpendicular to the optic axis is greater than that of the same material measured parallel to the optic axis, over the range 200° to 500° C. Quartz has two crystalline modifications, α and β. For alpha quartz, the existence of tunnels parallel to the optic axis has been suggested in the literature, while similar tunnels are postulated to be absent in the directions perpendicular to the optic axis [14]. This tunnellike structure is supposedly responsible for the

TABLE 3. *Qualitative spectrochemical analysis of silica glass and quartz*

Impurity	Quartz		Silica glass	
	Percentage by weight [a]	Ions per gram of silica	Percentage by weight [a]	Ions per gram of silica
Ag	0.0001	10^{15}	0.0001	10^{15}
Al	0.01 to 0.1	10^{18} to 10^{19}	0.001 to 0.01	10^{17} to 10^{18}
Ca	0.0001 to 0.001	10^{16} to 10^{17}	0.0001 to 0.001	10^{16} to 10^{17}
Cr	0.0001 to 0.001	10^{16} to 10^{17}	?	
Cu	0.0001	10^{16}	0.0001	10^{16}
Fe	0.001 to 0.01	10^{17} to 10^{18}	0.0001 to 0.01	10^{17} to 10^{18}
Mg	0.001 to 0.01	10^{17} to 10^{18}	0.001 to 0.001	10^{16} to 10^{17}
Na	0.001 to 0.01 ?	10^{17} to 10^{18} ?	0.001 to 0.01	10^{17} to 10^{18}

[a] Analysis performed in the Spectrochemistry Section of the Chemistry Division under the supervision of B. F. Scribner.

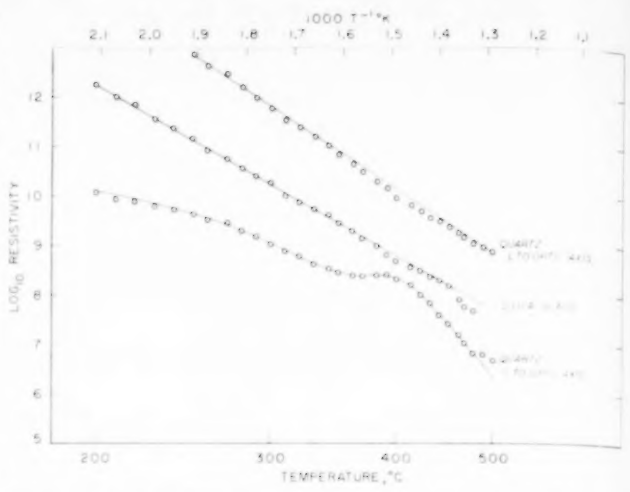

FIGURE 3. *Resistivity-temperature curves for silica glass and for quartz with optic axis parallel and perpendicular to applied field.*

ease of ion migration in quartz plates with optic axis parallel to the applied field [15]. This hypothesis is in agreement with the results plotted in figure 3.

From figure 3 it is also seen that the resistivity curve for quartz measured parallel to the optic axis does not follow the Rasch-Hinrichsen law, $\log R = (A/T) + B$, over the entire temperature range that was studied. This effect was observed on four independent determinations using four different specimens. The change in slope of the temperature-resistivity curve indicates that there is a change in the mechanism of conduction in the quartz whose optic axis is parallel to the applied field when the temperature exceeds about 360° C.

The transition temperature of α to β quartz is given as 573° C. However, X-ray diffraction studies performed on quartz [16] indicate that a partial reversible transition from the α to the β form may occur between room temperature and 573° C. If this apparent behavior of quartz is further substantiated by additional X-ray studies, the results may be helpful in explaining the observed change in slope in the temperature-resistivity curve.

It is not within the scope of this paper to discuss the conduction mechanism in silica in any greater detail. The results do, however, indicate that a more critical study of the electrical properties of allotropic modifications of silica might yield important information regarding the mechanism by which ions migrate through a structure composed of SiO_4 groupings. In addition such a study might throw further light on the exact structural arrangements of the various modifications of silica.

7.2. Alkali-Lead Silicates

Figure 4 shows the resistivity-composition isotherms at 200°, 300°, and 400° C that were obtained when lead oxide was replaced with equivalent amounts of lithium oxide, sodium oxide, or potassium oxide. Crossover of curves which are similar to the ones shown in this figure are reported in the

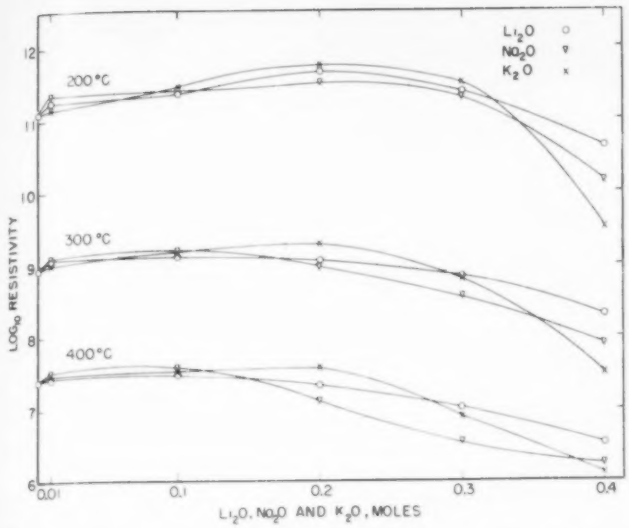

FIGURE 4. *Resistivity-composition isotherms for lithium, sodium, and potassium lead silicates prepared by equivalent substitution of* Li_2O, Na_2O, *or* K_2O *for* PbO in $PbO:SiO_2$.

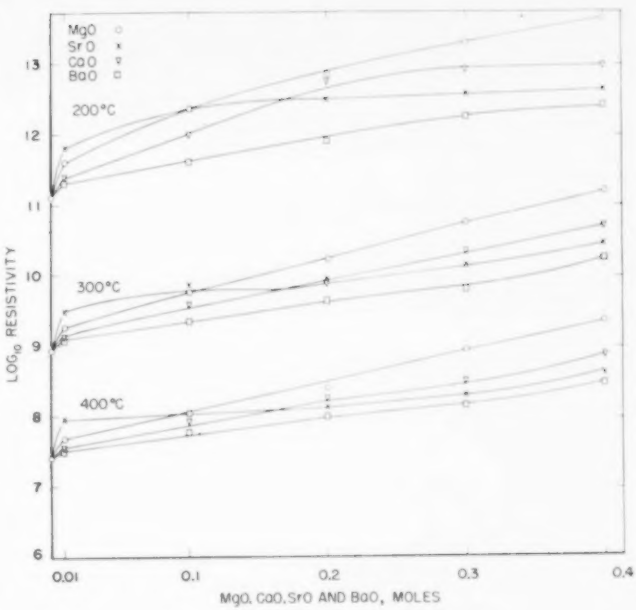

FIGURE 5. *Resistivity-composition isotherms for magnesium, calcium, strontium, and barium lead silicates prepared by equivalent substitution of* MgO, CaO, SrO, or BaO *for* PbO *in* $PbO:SiO_2$.

literature for resistivity-composition isotherms as well as for viscosity-composition curves for alkali silicates [17]. It will be noted in figure 4, that replacement up to about 0.3 mole at 200° C, 0.2 mole at 300° C, and 0.1 mole at 400° C yield glasses whose resistivities are somewhat greater than the resistivity of the base composition. Such behavior suggests that additions of alkali at the expense of lead up to a certain optimum amount actually tightens the structure, thereby making migration of ions more difficult. A tightening of this type may be expected if the lead is acting as a network former, a role that it is reported to assume at high concentrations [18]. As more alkali ions are substituted for lead, however, a point should be reached where the presence of extra alkali ions would more than compensate for the tightening effect resulting from the removal of lead from the network positions. The resistivity should then decrease upon further addition of alkali ions and figure 4 shows that such a decrease does occur.

7.3. Alkaline Earth and Transitional Element Lead Silicates

Figure 5 shows the resistivity-composition isotherms for alkaline earth lead silicates, while the resistivity-temperature curves for iron, cobalt, and nickel lead silicates are given in figure 6.

In figure 5, there is a definite trend toward increased resistivity with increasing concentration of the alkaline earth oxide. A behavior of this type might indicate a general tightening of the structure from the replacement of lead with the alkaline earth ion, making it more difficult for alkali ions, present as trace impurities, to migrate through the structure. A second interpretation might be based on the possibility that lead and the alkaline earth ions are themselves responsible for at least part of the conduction. However, such an interpretation would be

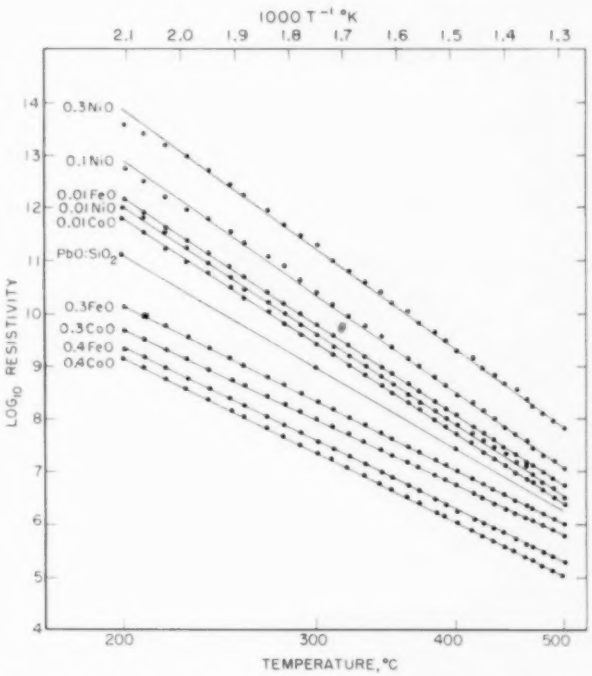

FIGURE 6. *Resistivity-temperature curves for* xFeO:$(1-x)$ $PbO:SiO_2$, xCoO:$(1-x)PbO:SiO_2$ *where* x *ranges from 0 to 0.4 and for* yNiO:$(1-y)PbO:SiO_2$ *where* y *ranges from 0 to 0.3.*

meaningless until it can be demonstrated by some suitable experimental technique that ions other than alkalies are free to move in a rigid silicate network.

The slopes on the curves in figure 6 show that while iron and cobalt tend to decrease the heat of activation when 0.3 and 0.4 mole of these oxides

are added to the base composition, nickel tends to increase the heat of activation at all concentrations studied. The addition of small amounts of iron and cobalt appears to have the same effect upon heat of activation as a small amount of nickel. One possible reason for this behavior may be that at small concentrations these ions (also the nickel ion), which are about as small as a lithium ion, enter deep potential energy holes and cause a tightening of the structure. The nickel glasses were also much more difficult to prepare than the iron or cobalt glasses, in that they showed a greater tendency to devitrify.

8. Interpretation of Resistivity Data in Terms of Energy Considerations

In view of the finite conductivity found in the quartz used as the raw material, it seems probable that the major part of the conduction in all the glasses studied may have been due to alkali ions, either added or present as impurities.[6] This assumption will be implicit in the following discussions which will apply to ternary lead silicates in which 0.4 mole PbO in a base composition $PbO:SiO_2$ was replaced by oxides the ions of which are given in figure 7.

8.1. Electrostatic Bonding Energy Considerations

Various investigations [19] have used charge and ionic radius to obtain a semiquantitative classification of glass constituents. Such expressions as e/r, e/r^2, Ze/r, or Ze/r^2 (Z, e, and r representing valence, charge of the electron, and ionic radius) have been used to express the relative magnitude of cation-oxygen bond energy in vitreous silicates. When other ions were introduced into the base composition one of the results may have been a tightening or loosening of the silicate framework. The extent of this tightening (or loosening) of the structure was probably dependent, in part at least, upon the size, charge, and the position occupied by the cation added to the base composition. The electrostatic bonding energy was therefore used as a first approximation to estimate the relative tightening (or loosening) effect produced by introducing other ions into the base composition. The equation for electrostatic bonding energy [20] is $E=-Z_1Z_2e^2/R_{12}$; where E=electrostatic bonding energy, Z_1 and Z_2 are the valences of the cation and the oxygen ion respectively, e is the charge of the electron, and R_{12} is the cation to oxygen distance. This equation states that the magnitude of the bonding energies increases with the valences and decreases with the atomic separation. Figure 7[7] is a plot of the logarithm of the resistivity at 200° C against the logarithm of the quantity $(-e^{-2}E)$ which is proportional to the electrostatic bonding energy.[8] Possible oxidation states

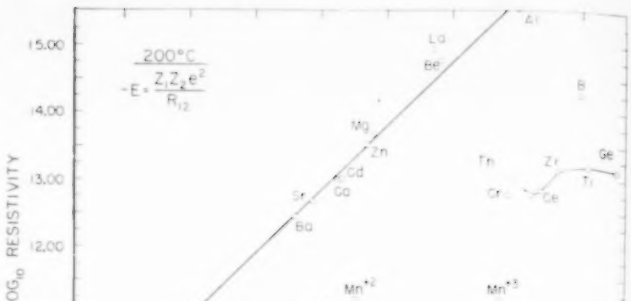

FIGURE 7. *Resistivity-bonding energy isotherm for lead silicate and for ternary lead silicates prepared by the equivalent replacement of 0.4* PbO *in the base composition* $PbO:SiO_2$ *by each of the ions listed on the curves.*

In the bonding energy expression, E=electrostatic bonding energy, e=charge of the electron, Z_1 and Z_2 are the valences of the cation and oxygen ion, respectively, and R_{12}=cation-oxygen distance.

are indicated for iron and manganese to illustrate the variable valency of transitional element ions.

It is interesting to note that the ions added to the base composition, seem to fall into three general classes. The first class contains ions of groups I, II, and the ions Al and La, the second group contains tetravalent ions, and the third, less defined group, contains the ions chromium, manganese, iron, and cobalt. With the exception of iron and cobalt only the alkali ions added to the base composition decreased the resistivity. This observation appears to be consistent with the assumption that the major part of the conduction may be due to the alkali ions.

Figure 8 gives a plot of upper and lower limits of heats of activation against composition for lead silicate and for lithium, sodium, and potassium lead silicates. The heats of activation were calculated from the slopes of curves obtained by plotting the logarithm of the experimentally determined resistivity values against the reciprocal of the absolute temperature. The data indicate that there is an initial rise in heat of activation followed by a drop at the 0.4 mole composition. An initial rise in heat of activation is in accord with the suggestion made earlier that initial replacement of lead by alkali might yield a tightening of the structure.

A plot of heat of activation, ΔH^*, against the logarithm of the frequency factor, log A, is given in figure 9. The quantities log A and ΔH^* appear as parameters in the equation $\log \rho=\log A+(\Delta H^*/2.3RT)$ where ρ is the resistivity. Although the scatter is relatively large and log A is a complex quantity, the decrease in log A observed with the alkali ions contrasted to the constancy or slight increase in log A for the other ions is consistent with the alkali ions alone providing additional charge carriers.

[6] Since all glasses contain some water it is of course possible that hydrogen ions may also contribute towards conduction.

[7] Similar curves were obtained at 300, 400, and 500° C.

[8] Crystal radii were used in the calculation of electrostatic bonding energies. It is realized that these ionic radii values are relative. In a glass, which is sometimes described as a supercooled liquid, absolute values for ionic radii may be expected to be different from crystal radii values. Changes in coordination number may also affect the sizes of ionic radii.

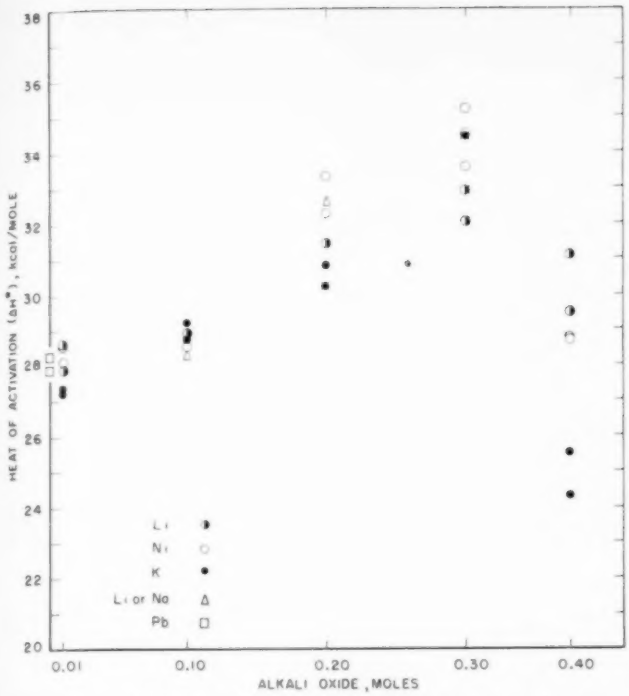

FIGURE 8. *Upper and lower limits of heat of activation—composition data for lead silicate and for lithium, sodium, and potassium lead silicates prepared by equivalent substitution of* Li_2O, Na_2O, *or* K_2O *for* PbO *in* $PbO:SiO_2$.

Figure 10 shows heat of activation-ionic radius curves. For the alkali ions, ΔH^* decreases from lithium to potassium and then begins to increase from potassium to rubidium. The minimum or at least change in slope at potassium appears to be real and beyond experimental error. It can be explained in the following way.

Before an alkali ion can migrate, the free energy of activation must be exceeded. This involves overcoming the chemical binding energy (breaking the cation-oxygen bond) and, in addition, sufficient energy (network repulsion energy term) must be supplied to the alkali ion so that it can pass through the interstitial hole. From the standpoint of the chemical binding energy term, the smaller the cation the more energy it will take to break the cation-oxygen bond. On the other hand, the smaller the cation the smaller will be the network repulsion energy term required to move it into the next interstitial hole. Assuming that the approximate structure of glass does not differ appreciably from a model such as is depicted by Poncelet [21], the average diameter of the opening between interstices is approximately equal to that of an oxygen ion. Anderson and Stuart [22] in discussing the structure of glass state "Although it is true that the volume of the interstice may change when an ion is added, there are four doorways connecting the interstice containing the ion to adjacent interstices and the average size of the doorway through which the ion must pass will not change significantly."[9] An ion smaller than

[9] It is of course possible that some of the openings between interstitial holes may be larger than the circumference of an oxygen ion. Even if this would be the case the discussion would still be generally the same as the one presented.

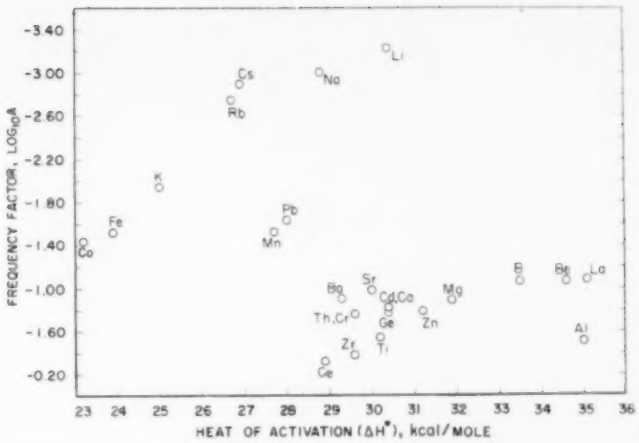

FIGURE 9. *Heat of activation—frequency factor data for lead silicate and for ternary lead silicates prepared by the equivalent replacement of 0.4* PbO *in the base composition* $PbO:SiO_2$ *by each of the ions listed.*

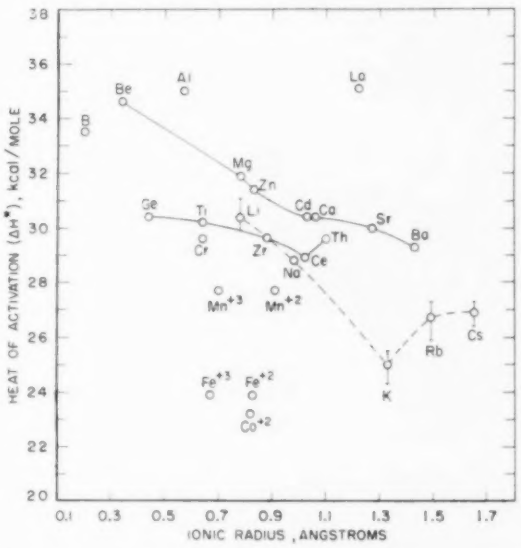

FIGURE 10. *Heat of activation—ionic radius curves for ternary lead silicates prepared by the equivalent replacement of 0.4* PbO *in the base composition* $PbO:SiO_2$ *by each of the ions listed on the curves.*

oxygen should pass through the opening to the interstitial hole with considerable ease whereas ions larger than oxygen have to expand the entrance to the interstitial hole before they can pass through. Hence, in the latter case the network repulsion energy term may become a large fraction of the total energy requirement and the ion would have to surmount a higher energy barrier before it could migrate into the next interstice. The ions rubidium and cesium are larger than oxygen therefore the network repulsion energy term for each of these cations may be appreciably larger than that for any of the first three alkali ions. This increase in the network repulsion energy term apparently more than compensates for the decrease in the chemical binding energy term with a net result that the total energy of activation is

greater for rubidium or cesium than for potassium. This explanation should be accepted with some reservation until additional experimental data are available.

The preceding discussions may be summarized as follows: The data indicate that the ions added to the base composition fall into four groups: (a) alkali ions tend to decrease log A and to vary the heat of activation, with an indication of decreasing the heat of activation with increasing radius, and with a possible minimum or a change in slope at potassium; (b) iron and cobalt do not appear to affect log A but decrease the heat of activation; (c) manganese affects neither log A nor the heat of activation; and (d) the other ions increase log A, and increase the heat of activation, with an indication that within a group of isovalent ions the heat of activation decreases with increasing radius (see fig. 10). A more complete interpretation of the data cannot be given until such time as experimental evidence is obtained to determine conclusively whether or not nonalkali ions (also hydrogen ions from water in the glass) take part in the conduction process and if so, under what conditions and to what extent. In this connection diffusion and transference number data should yield valuable information.

9. Summary

Resistivity data were presented for silica glass, for quartz, and for ternary lead silicates prepared by the partial substitution of 25 oxides, one at a time, for lead oxide in a base composition of $PbO:SiO_2$.

The results of this investigation were discussed on the basis that alkali ions may have been the only conducting ions. For the nonalkali glasses studied, the nonalkali ions introduced into the base composition were assumed to affect the migration of alkali ions, present as impurities, by altering the silicate structure.

The resistivity of silica glass was found to be less than that for quartz measured perpendicular to the optic axis but greater than that for quartz measured parallel to the optic axis.

For quartz measured parallel to the optic axis the data indicate that a change in the conduction process occurs at about 360° C.

Results on the ternary lead silicates investigated indicate that the relative change in resistivity produced by substituting different ions for lead in the base composition is dependent on the nature of the ions added.

Relative to the base composition, substitution for 0.4 mole Pb^{+2} of alkali ions, iron, and cobalt decreased the resistivity, manganese did not affect the resistivity, and the other ions increased it.

The authors thank J. D. Hoffman of the Polymer Structure Section and A. Franklin of the Porcelain and Pottery Section of the Bureau for their helpful discussions on certain aspects of the problem.

10. References

[1] S. W. Strauss, L. E. Richards, and D. G. Moore, Effect of temperature on the electrical resistivity of several ceramic and silicone-type coatings, ASTM Special Tech. Publ. No. 153, p. 101 (1953).
[2] H. Buff, Liebig Ann. **90,** 257 (1854).
[3] W. Beetz, Liebig Ann. **92,** 452 (1854).
[4] E. Seddon, E. J. Tippet, and W. E. S. Turner, J. Soc. Glass Tech. **16,** 451 (1932).
[5] G. W. Morey, The properties of glass, ch. XVII, XVIII (Reinhold Publishing Corp., New York, N. Y., 1954).
[6] E. J. Murphy and S. O. Morgan, Bell System Tech. J. **16,** 493 (1937); **17,** 640 (1938); **18,** 502 (1939).
[7] J. M. Stevels, Progress in the theory of the physical properties of glass, ch. III, IV (Elsevier Publishing Co. Inc., 1946).
[8] J. E. Stanworth, Physical properties of glass, pt. II, ch. 6 (Oxford Univeristy Press, 1950).
[9] W. Eitel, The physcial chemistry of the silicates, pt. A, section II (Univeristy of Chicago Press, 1954).
[10] R. Smoluchowski, J. E. Meyer, and W. A. Weyl, Phase transformation in solids, p. 307 (John Wiley & Sons, Inc., New York, N. Y., 1951).
[11] H. Moore and R. C. DeSilva, J. Soc. Glass Tech. **36,** 168, 5(T) (1952).
[12] G. Gehlhoff and M. Thomas, Z. Tech. Phys. **6,** 544 (1925).
[13] Mellor's Comprehensive Treatise on Inorganic and Theoretical Chemistry, **6,** 265 (Longmans, Green & Co., 1947).
[14] R. E. Gibbs, Proc. Roy. Soc., London [A] **110,** 443 (1926).
[15] P. M. Harris and C. E. Waring, J. Phys. Chem. **41,** 1077 (1939).
[16] Private communication from A. Van Valkenberg of NBS Constitution and Microstructure Section.
[17] W. Eitel, The physical chemistry of the silicates, p. 214, 236 (University of Chicago Press, 1954).
[18] J. M. Stevels, Progress in the theory of the physical properties of glass, p. 18 (Elsevier Publishing Co., Inc., 1946).
[19] N. J. Kreidl, Ceramic Age **57,** 256 (1948).
[20] B. E. Warren and A. G. Pincus, J. Am. Ceram. Soc. [10] **23,** 301 (1940).
[21] E. F. Poncelet, Verres et Refractaires **2,** 208 (1948).
[22] O. L. Anderson and D. A. Stuart, J. Am. Ceram. Soc. [12] **37,** 579 (1954).

Washington, November 3, 1955.

Journal of Research of the National Bureau of Standards Vol. 56, No. 3, March 1956 Research Paper 2659

Some Factors Affecting the Precision of Polarographic Half-Wave Potential Measurements

John K. Taylor and Stanley W. Smith

The experimental conditions required for the precise determination of polarographic half-wave potentials have been investigated and are discussed. The values of half-wave potentials vary with the characteristics of the dropping-mercury electrode in the case of reduction of metal ions to metal soluble in mercury. Consequently, it is necessary to specify the experimental condition whenever values for half-wave potentials are reported. With proper precautions it is possible to attain reproducibility within ±0.2 millivolt in the measurements.

1. Introduction

The polarographic half-wave potential is of interest because of its use in the qualitative identification of electrode reactions. Of even greater interest, however, is its thermodynamic significance and its application to the problem of determining the complexity constants for complex ions [1,2].[1] In most cases the half-wave potential data presented in the literature have been precise to less than plus or minus several millivolts. While this is sufficient for qualitative purposes, it is not of the required precision for the other applications. The purpose of this investigation was to determine the precision with which it is possible to measure half-wave potentials and also to study the factors affecting the measurements. As the purpose of the work was to investigate methods by which precise values may be obtained and not to establish a precise half-wave potential spectrum, relatively few reducible materials were examined.

2. Experimental Measurements

All half-wave potential measurements were made with a manual arrangement, the circuit diagram of which is shown in figure 1. The voltage was applied to the cell by means of the slide wire (S) of a Sargent model XII or model XXI polarograph. The potential of the dropping-mercury electrode (DME) with respect to the saturated calomel reference electrode (REF) was measured with a precision potentiometer (Pot). The current was measured with an Ayrton shunt (SH) and a lamp and scale galvanometer (G_1). Galvanometer (G_2), the null indicator on the potentiometer, was a "spotlight" type of instrument. A system of B_2, R_2, R_3, R_4, and R_5 was included for the calibration of the galvanometer (G_1). This calibration current could be calculated from the voltage drop across R_1 and its known value of resistance.

The cell arrangement shown in figure 2 consisted of a 100-ml beaker fitted with a rubber stopper that contained inlet tubes for nitrogen for the removal of oxygen from the solution and holes for the access

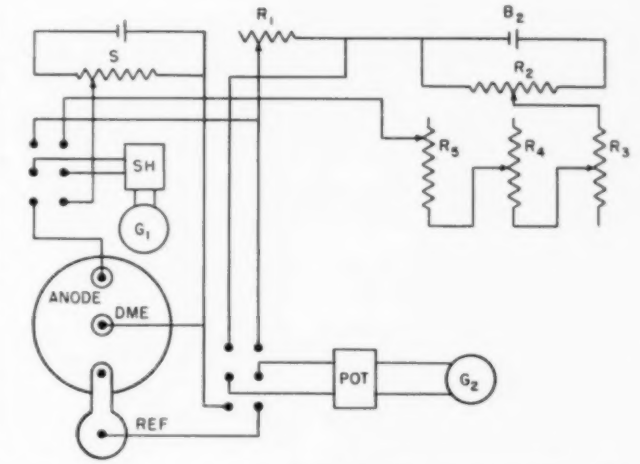

FIGURE 1. *Manual arrangement for the measurement of half-wave potentials.*

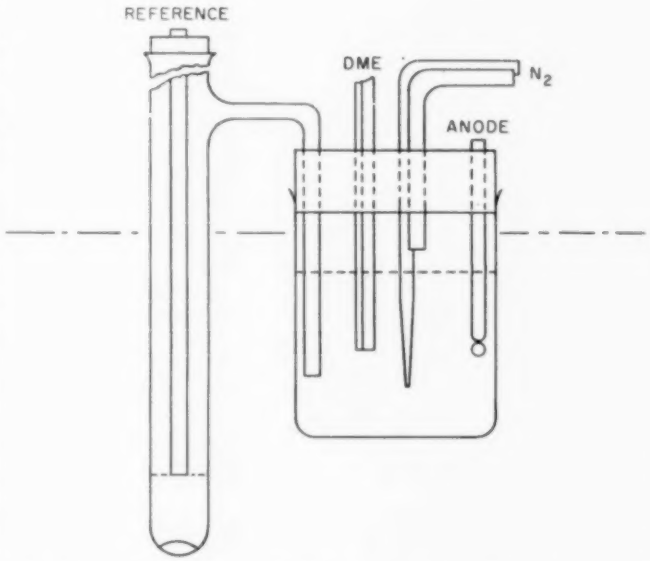

FIGURE 2. *Polarographic cell used in half-wave potential measurements.*

[1] Figures in brackets indicate the literature references at the end of this paper.

of the dropping-mercury electrode, the silver–silver-chloride working electrode (Anode), and the sidearm of the saturated calomel reference electrode (Ref). The Ag-AgCl anode, of the thermal-electrolytic type [3], had a large surface area to minimize polarization effects under the conditions of the measurements. This electrode was used because it was found that the silver-wire anodes frequently recommended were of insufficient surface area to prevent polarization effects. The saturated calomel electrode (S. C. E.) was so constructed that a large portion of it was immersed in the bath. The sidearm contained an agar plug saturated with KCl. All potential measurements were made with respect to this reference electrode.

A number of capillaries were used during the course of the investigation. A capillary of marine barometer tubing producing drops having a mass of 6.9 mg (*mt* value) was used in the investigation of the dependence of half-wave potential on concentration. In the determination of the dependence of the half-wave potential on capillary characteristics, the capillaries had *mt* values of 6.8, 8.8, 10.2, 32, and 64 mg, respectively. The first three of these were of marine barometer tubing and the last two were of the constricted type described by Taylor and Smith [4].

Before each series of runs, the cell was cleaned in a hot sulfuric-acid–potassium dichromate solution and then steamed for about 15 min. The stopper assembly was rinsed in distilled water and allowed to dry before it was placed in the cell. The Ag-AgCl electrode was stored between runs in 0.01 *N* HCl and before use was rinsed with distilled water and dried with a filter paper. The calomel electrode was stored with the sidearm immersed in saturated KCl and was treated in a similar manner before insertion in the cell.

Nitrogen was used to remove oxygen from the solutions. The gas was passed over hot copper to remove any traces of oxygen before introduction into the cell. While the measurements were being made, the nitrogen flowed over the surface to prevent oxygen from reentering the solution.

All measurements were made in a constant temperature bath maintained at $25\pm0.01°$ C.

Stock solutions of the metal ions used were made by dissolving weighed portions of the pure metals in acid, evaporating the solution to dryness several times to remove all of the acid, and then dissolving the residue in distilled water and diluting to the desired concentration. All other materials were reagent grade chemicals used without further purification.

The capacitance-conductance bridge network shown in figure 3 was assembled to measure the resistance of the cells and the change of resistance with applied voltage, drop time, etc. R_1 and R_2 are the ratio arms of the bridge and were equal to 500 ohms for the sensitivity used. The measuring arm of the bridge consisted of R_3 and C, a mica condenser variable in 0.001-μf steps from 0 to 1.11 μf.

A 1,000-ohm resistance, R_4, was inserted to reduce the shunting effect of the potentiometer (P) on the detector (D). (P) was the slide wire of the model

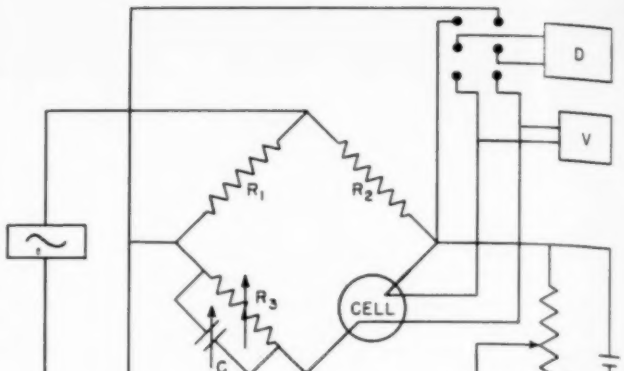

FIGURE 3. *Circuit for the measurement of the resistance of the polarographic cell.*

XII polarograph with the voltage increased to 5 v. The signal source was a beat frequency oscillator with an output voltage necessary to give 0.04 v across the cell. The voltmeter (V) used to measure the d-c voltage drop across the cell was a Beckman H–2 *p*H meter. The detector (D) was a cathode-ray oscillograph connected to the circuit so that it could be used as an a-c voltmeter across the cell, as well as the null point detector for the bridge. To study the variation of cell resistance with time, the bridge was set at some value greater than the minimum resistance and the time was recorded from the beginning of the drop until a balance was indicated. This was repeated at a series of R values until the curve shown in figure 4 was obtained.

Measurements of the half-wave potential, E_{i_d}, were made in the following manner. The current and voltage were measured at a point about 0.1 v or more preceding the half-wave potential to establish a zero point for the wave, and at appropriate voltage increments up to and including the diffusion current plateau. Measurements on the supporting electrolyte alone at corresponding voltages gave values of the residual current, which were subtracted from the current readings above to give values of i. For values several tenths of a volt greater than the half-wave potential, the current is practically independent of the applied voltage (diffusion current plateau) and is designated the diffusion current, i_d. From these values of the current, $\log i/(i_d-i)$ was calculated and plotted with respect to the measured voltage. From this plot, the value of E at $\log i/(i_d-i)=0$, when corrected for the voltage drop in the cell, corresponds to the half-wave potential. A typical plot is shown in figure 5. It may be seen that the curve is linear and that the reciprocal of the slope is 0.0306 v, in satisfactory agreement with the theoretical value of 0.0295 v. The value of R used in the correction for the iR drop is four-thirds of the minimum cell resistance corresponding to the average R during the life of the mercury drop.

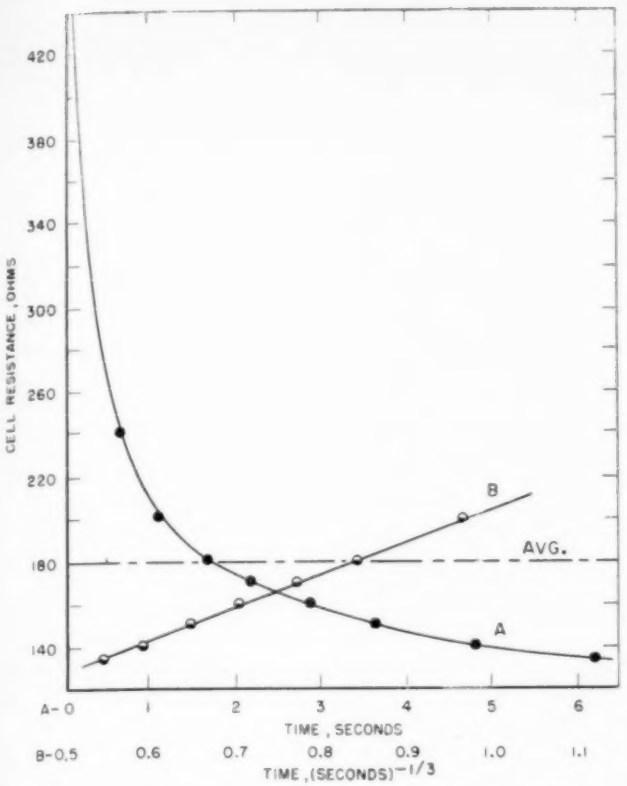

FIGURE 4. *Electrical resistance of a dropping-mercury electrode.*

(a) Plot of resistance-time variation during the life of a 7-mg drop and at a drop time of 6.2 sec.
(b) Demonstration that the resistance varies with (time)$^{-1/3}$.

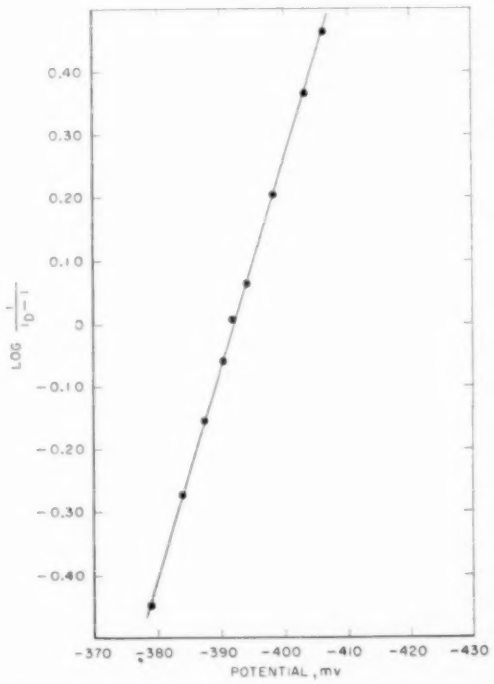

FIGURE 5. *Plot of potential of the DME versus log $i/(i_d - i)$ from which the half-wave potential is obtained.*

3. Results

3.1. Variation of $E_{1/2}$ With the Characteristics of the Galvanometer Used on the Potentiometer

Measured values of the potential of the dropping electrode with respect to a reference electrode vary with time during the growth of the mercury drop due to the variation of voltage drop (iR) in the cell. It is not feasible to measure either the maximum or minimum value of this potential. Accordingly, the potentiometer is balanced at some average value as evidenced by the symmetrical deflection of the "null" galvanometer around its rest point. It is evident that such a potentiometric reading will be influenced by the characteristics of the null galvanometer and will approach the time average value when the characteristics are such that it can integrate the voltage variation that exists.

It was found that for the conditions given below, when the damping was near critical and the period of the galvanometer was of the same order as or greater than the drop time, there was no significant variation of $E_{1/2}$ with period of the galvanometer or with the damping. If the period was short or the damping resistance was very large, the values obtained for the half-wave potential were increased. Under these conditions the galvanometer does not integrate the voltage-time curve [5, 6], and the voltage read is no longer the average voltage corresponding to the average current. The conditions for the measurements were as follows: Drop time, 5.7 sec; reducible ion, 1 mM Cd; supporting electrolyte, 0.1 *N* HCl, 0.01 percent gel; $t = 25°$ C; head 70 cm; marine barometer capillary; reference, S. C. E. The galvanometers and characteristics are listed below.

NBS galvanometer	Period	Critical damping resistance	Damping resistance
	sec	*Ohms*	*Ohms*
3568	1.85	43	10; 43; ∞
16350	3.83	2,700	700; 2,700; ∞
10442	5.26	43,000	10,000; 43,000; ∞
5705	15.5	21,000	21,000; ∞

The magnitude of the error from this source is not large but is significant in precise measurements. The maximum error to be expected is of the order of one-half of the iR correction and would be obtained when using a balance indicator of very short period, for example, an oscilloscope. When using the galvanometer with period of 1.85 sec and infinite damping resistance, errors in the half-wave potential of 1 mv were observed. On the other hand, with the galvanometer of 15.5-sec period, half-wave potential measurements were practically independent of the damping resistance used.

3.2. Measurement of Resistance

It was found that, as a practical matter, the resistance measurements needed for the iR drop correction may be made with sufficient accuracy on the supporting electrolyte, by the use of a small 1,000-cps conductance bridge with an "electronic-eye" detector, provided that the capacity balance is closely maintained. As shown in figure 4, the resistance varies as the minus one-third power of time, in accord with theory. The average value of the resistance is four-thirds of the minimum value, occurring at the time of dislodgment of the drop.

Measurements of resistance with no applied d-c potential were found to be applicable over the range of potential used, since the variation of resistance with potential is small, and the accuracy of measurement decreases with the potential. The resistance was found not to vary significantly with drop time. For example, with a capillary for which $mt=8.8$ at drop times of 3.92, 3.12, 2.58, 2.22, 1.94, and 1.74 sec, the resistances were 195, 196, 197, 196, 197, and 197 ohms, respectively.

With a reducible ion in the solution, the behavior of the resistance and capacitance at the half-wave potential was generally in accord with the observations of other investigators [7, 8]. However, as this phenomenon had no direct bearing on this investigation, it was not pursued in detail.

3.3. Variation of $E_{\frac{1}{2}}$ With the Concentration of Reducible Ion

Measurements of half-wave potentials for this study were made with a marine barometer capillary with a drop weight of 6.9 mg and at a drop time of 5.8 sec. The temperature was held at 25 $\pm$0.01° C. for all runs. Measurements made on Cd^{++} in 1.0 N KCl and 0.1 N HCl, and on Pb^{++} in 0.1 N KCl and 0.1 N HCl show no significant variation of $E_{\frac{1}{2}}$ with concentration of reducible ion from 0.5 mM to 5.0 mM. However, the correction for the iR drop is very important in these measurements, being as large as 5 mv for the most concentrated solutions. A typical plot in figure 6 shows curves before (A) and after (B) the iR correction has been made.

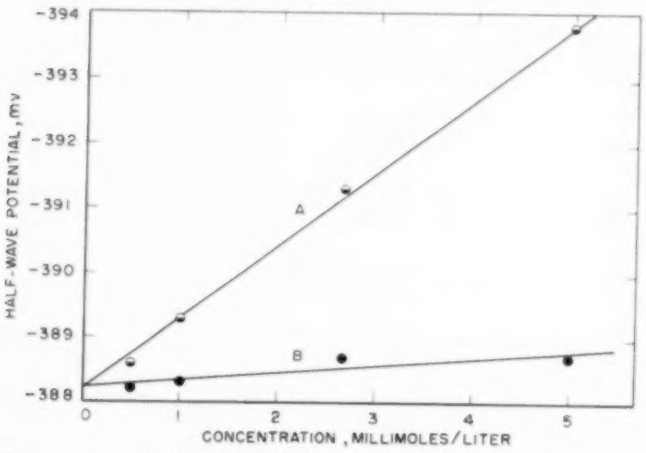

FIGURE 6. *Variation of $E_{1/2}$ with concentration (A) and the same data after the iR drop has been corrected (B).*

It was found that moving the reference electrode from one position to another in the cell did not affect the potential measured with respect to the dropping-mercury electrode. A separate experiment was performed, using a cell in which three compartments filled with 0.1 N KCl were separated by tubes containing agar plugs of several hundred ohms resistance. Silver–silver-chloride electrodes were placed in the end compartments and a potential was applied. It was found that the portion of the fall of potential between the electrodes, as measured by a reference electrode, depended on its distance between them. In this case, however, the resistance at the surface of the Ag–AgCl electrodes is small, whereas that of the intervening medium is large; therefore, the greater part of the potential drop occurs across the solution and not at the electrode interface. In the case of the DME, the resistance of the drop interface is large and that of the intervening medium is relatively small, so that the greater part of the potential drop occurs across the interface. It is not possible, therefore, to place the reference electrode close enough to the drop to exclude measuring this fall of potential. For this reason the half-wave potential must be corrected for iR drop, although no cell current is involved.

3.4. Variation of $E_{\frac{1}{2}}$ With Capillary Characteristics

In the reduction of a metal ion to metal soluble in mercury, the half-wave potential has been found to vary with the drop time and size of drop of the electrode, other factors remaining constant. This variation is approximately linear with drop time for a given electrode, as is shown in figure 7. However,

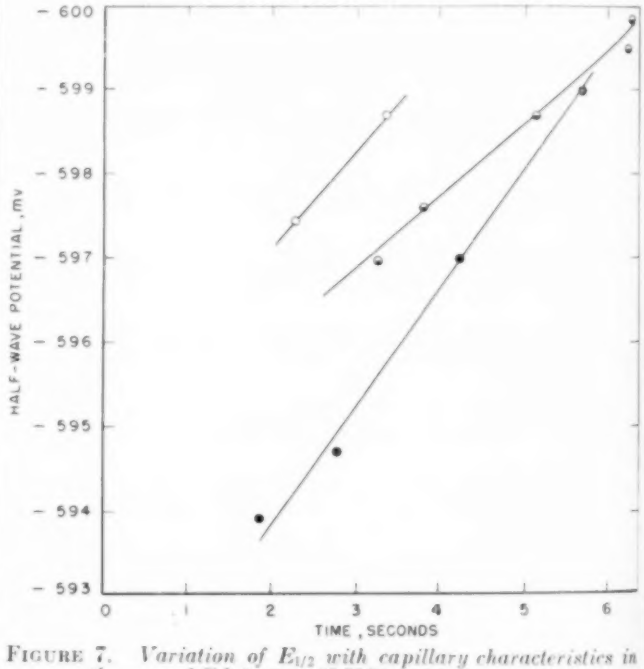

FIGURE 7. *Variation of $E_{1/2}$ with capillary characteristics in the case of* Cd *in 0.1 N* KCl, *0.01 percent gel.*

●, Capillary 8.8; ◒, capillary 32; ○, capillary 64.

no simple relation appears to exist between the curves obtained for the several electrodes studied. The metal ions Cd^{++}, Pb^{++}, and Tl^{++} have been used in this investigation with capillaries having *mt* values of 6.8, 8.8, 10.2, 32, and 64 mg, respectively. In the case of homogeneous electrode reactions involving reduction from a higher to a lower oxidation state, in which the dropping electrode acts as an indicator electrode, there is no variation with drop time and only slight variation with drop size, as is shown in figure 8. The supporting electrolytes were: for Pb, Cd, and Tl, 0.1 *N* KCl, 0.01 percent gel; for Fe, 1.0 *M* $K_2C_2O_4$, 0.01 percent gel; for quinhydrone, 0.04 *M* Na_2HPO_4, 0.027 *M* NaH_2PO_4. The $E_{1/2}$ values obtained for all cases are shown in tables 1, 2, 3, 4, and 5.

TABLE 1. *Half-wave potential of* Cd *for a series of capillaries and drop times*

The supporting electrolyte is 0.1 *N* KCl and 0.01 percent gelatin, except where noted. (Temperature, 25.0° C)

Capillary (*mt* value)	Drop time	$E_{1/2}$
mg	*sec*	*v*
8.8	1.90	−0.5939
8.8	2.82	−.5947
8.8	4.25	−.5970
8.8	5.70	−.5990
32	3.26	−.5970
32	3.78	−.5976
32	5.14	−.5987
32	6.38	−.5995
32	6.68	−.5999
64	2.32	−.5974
64	3.36	−.5987
6.9	5.8	−.5958
6.9 (0.1 *N* HCl)	5.8	−.6015
6.9 (1.0 *N* KCl)	5.8	−.6432

TABLE 2. *Half-wave potential of* Pb *for a series of capillaries and drop times*

The supporting electrolyte is 0.1 *N* KCl and 0.01 percent gelatin, except where noted. (Temperature, 25.0° C)

Capillary (*mt* value)	Drop time	$E_{1/2}$
mg	*sec*	*v*
8.8	1.92	−0.3882
8.8	2.90	−.3891
8.8	4.30	−.3906
8.8	5.74	−.3923
32	3.20	−.3918
32	4.32	−.3917
32	4.86	−.3921
32	6.38	−.3927
64	2.28	−.3913
64	3.42	−.3922
6.9 (0.1 *N* HCl)	5.8	−.3953
6.9	5.8	−.3885

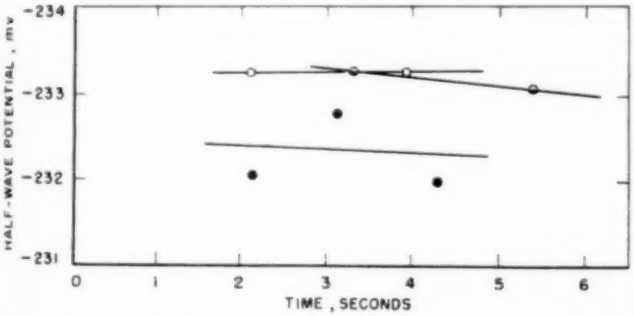

FIGURE 8. *Variation of $E_{1/2}$ with capillary characteristics in the case of the Fe^{+2}, Fe^{+3} system in 1.0 M $K_2O_2O_4$, 0.01 percent gel.*

●, Capillary 8.8; ◒, capillary 32; ○, capillary 64.

TABLE 3. *Half-wave potential of* Tl *for a series of capillaries and drop times*

The supporting electrolyte is 0.1 *N* KCl and 0.01 percent gelatin. (Temperature 25.0° C)

Capillary (*mt* value)	Drop time	$E_{1/2}$
mg	*sec*	*v*
6.8	4.24	−0.4573
6.8	5.30	−.4601
6.8	6.56	−.4629
8.8	2.88	−.4519
8.8	4.82	−.4560
8.8	5.64	−.4598
10.2	2.14	−.4538
10.2	3.10	−.4555
10.2	4.24	−.4584
32	3.28	−.4587
32	4.34	−.4593
32	5.34	−.4600
64	2.22	−.4593
64	3.22	−.4598

TABLE 4. *Half-wave potentials of the Fe^{++}, Fe^{+++} system for a series of capillaries and drop times*

The supporting electrolyte is 1.0 *M* $K_2C_2O_4$ and 0.01 percent gelatin. (Temperature 25.0° C)

Capillary (*mt* value)	Drop time	$E_{1/2}$
mg	*sec*	*v*
10.2	2.14	−0.2321
10.2	3.08	−.2328
10.2	4.26	−.2320
32	3.28	−.2333
32	5.42	−.2331
64	2.10	−.2333
64	3.92	−.2333

TABLE 5. *Half-wave potential of the Quinhydrone system for a series of capillaries and drop times*

The supporting electrolyte is 0.04 *M* Na_2HPO_4 and 0.027 *M* NaH_2PO_4 *p*H=7.0. (Temperature 25.0° C)

Capillary (*mt* value)	Drop time	$E_{1/2}$
mg	*sec*	*v*
10.2	2.06	+0.0510
10.2	2.98	+.0518
10.2	4.18	+.0507
32	3.24	+.0498
32	5.38	+.0493
64	1.98	+.0500
64	2.68	+.0499

4. Discussion

The results of this investigation show that the half-wave potential may vary significantly with the characteristics of the dropping electrode. Because variations of several millivolts can occur, it is important that the characteristics of the electrode be reported, in addition to information concerning the supporting electrolyte and temperature, to give the measurements their full significance. The importance of the correction for the iR drop in the cell is also emphasized.

Strehlow and Stackelberg [9] have predicted variation in $E_{\frac{1}{4}}$ with drop time caused by stirring effects within the Hg drop and the resultant disturbance of diffusion conditions for the amalgam. The variation of $E_{\frac{1}{4}}$ observed in this investigation in the case of the reduction of metal ions to an amalgam, and the lack of such variation in oxidation-reduction systems are in accord with this theory. The order of magnitude is such that a few percent change in the concentration of the amalgam at the surface would account for the variation observed. The problem of a quantitative treatment of this phenomenon is under study.

It has been shown by other investigators [10] that the half-wave potential is dependent on the capillary in the case of irreversible reactions. In the present case, however, the linearity of the log $i/(i_d-i)$ versus E plot, and the near theoretical slope obtained, attest to the reversibility of the reactions studied and eliminate irreversibility as the cause of the variations.

In order to attain reproducibility within ± 0.2 mv in half-wave potential measurements, several sources of error must be considered. The temperature of the cell and of the reference electrode must be known and held constant to within $\pm 0.1°$ C, since the temperature coefficients are approximately 0.8 mv/° C in each case. The residual current must be determined from measurements on a cell containing supporting electrolyte only, and the corresponding correction applied to the limiting current at each point. Fortunately, moderate errors in the residual current can be tolerated, as it is only a small fraction of the total current in the usual case.

The largest sources of error arise in the evaluation of the log $i/(i_d-i)$ versus E relationship and in the determination of the voltage drop in the cell. With respect to the first, comparison of graphical methods with least squares adjustment of the data shows agreement in the two methods to ± 0.1 mv. The simple plotting procedure can thus be relied on within this limit of precision. The magnitude of the iR correction depends on both the current and the cell resistance. In measurements of half-wave potential, cells should be designed to offer minimum electrical resistance, and the design used in this work appears to approach the optimum from this point of view. Such cells have resistances of the order of a few hundred ohms (largely interfacial resistance) which can be readily measured with ordinary equipment to within 3 to 4 percent. The magnitude of the diffusion current depends on both the size of the dropping electrode and the concentration of the electrolyzable material. However, since the resistance of the cell decreases with increase of the size of the drop, with corresponding increase in the current, it is not difficult to choose a combination so that the uncertainty in the iR correction will not exceed ± 0.1 mv, except in the case of the largest electrodes, where errors of several times this amount may result.

An important source of error in the measurement of half-wave potentials is the junction potential of the reference electrode-solution interface. This error may be of the order of several tenths of a millivolt and has been recently discussed by Vlcek [11]. No corrections for junction potentials have been made in this study, as they would be only approximate and would not affect the precision.

5. Summary

The sources of error in half-wave potentials have been investigated and found to lie chiefly in the correction for the iR drop in the solution and in the actual reproducibility of current and voltage measurements. When proper precautions are exercised, it is possible to obtain values reproducible to within ± 0.2 mv.

The half-wave potential is shown to vary with the size of drop and with the drop time of the electrode in the case of the reduction of metallic ions to metal soluble in the mercury electrode. On the other hand, much less variation was observed in homogeneous electrode reactions in which the dropping-mercury electrode acts as an indicator electrode. Accordingly, the observed variations are attributed to stirring effects within the drop and the resulting disturbance of diffusion conditions for the amalgam formed in heterogeneous reactions. In view of the large variations found, values of half-wave potential are not significant unless the characteristics of the electrode used for the measurements are reported.

6. References

[1] M. von Stackelberg and H. von Freyhold, Z. Elektrochem. **46,** 120 (1940).
[2] J. J. Lingane, Chem. Rev. **29,** 1 (1941).
[3] A. A. Noyes and J. H. Ellis, J. Am. Chem. Soc. **39,** 2532 (1917).
[4] J. K. Taylor and Roberta E. Smith, J. Research NBS **48,** 172 (1952) RP2302.
[5] J. K. Taylor, Roberta E. Smith, and I. L. Cooter, J. Research NBS **42,** 387 (1949) RP1978.
[6] F. K. Harris, Electrical Measurements, p. 302 (John Wiley & Sons, Inc., New York, N. Y., 1952).
[7] D. C. Graham, Chem. Rev. **41,** 441 (1947).
[8] B. Breyer and F. Gutman, Trans. Faraday Soc. **42,** 645 (1946).
[9] H. Strehlow and M. von Stackelberg, Z. Elektrochem. **54,** 51 (1950).
[10] P. Kivalo, K. B. Oldham, and H. A. Laitinen, J. Am. Chem. Soc. **75,** 4148 (1953).
[11] A. A. Vlcek, Collection Czechoslav. Chem. Communs. **19,** 862 (1954).

Washington, October 25, 1955.

Journal of Research of the National Bureau of Standards Vol. 56, No. 3, March 1956 Research Paper 2660

Infrared Measurements From 50 to 125 Microns[1]

Earle K. Plyler and Nicolo Acquista

A prism spectrometer has been changed to a long wavelength grating spectrometer by removing the prism and by replacing the Littrow mirror with a grating. Gratings of 320 and 180 lines per inch were used for the region 50 to 125 microns. A thermocouple with a crystal quartz window served as the detector. Stray radiation was greatly reduced by the use of reflection filters. Three types of reflection filters were found to be efficient. They were gratings with 2,000 lines per inch, roughened silver mirrors, and reststrahlen plates of NaCl, KBr, and CsBr. The absorption lines of water vapor were used to calibrate the spectrometer. The spectra of several substituted ethylenes and ethanes have been measured, and absorption bands have been found between 50 and 100 microns.

1. Introduction

During the last 2 years prisms of CsI have been available, and it is now possible to make measurements to 50 μ [1].[2] As quartz has its strongest reststrahlen band at 9 μ, it should transmit radiation at 100 μ. For thicknesses less than 1 mm, quartz has a good transmission of infrared radiation in the long wavelength region. However, with prisms of crystal quartz of a refracting angle of 7.5°, it was found that no appreciable energy was transmitted in the region 50 to 100 μ. Energy was recorded in the 150-μ region, but the resolution was low. Diamond is another material which is transparent in the long-wavelength region, but the expense and difficulty in obtaining material of sufficient size for a prism for infrared measurements would make its use impracticable. However, windows of diamond for detectors are useful for the infrared region.

2. Experimental Procedure

In order to extend measurements beyond 50μ, experiments were carried out by the use of small gratings. Large-grating spectrometers for the far infrared have been built in several laboratories [2], and it was felt that sufficient energy would be available with small gratings. A grating was installed in a spectrometer in place of the Littrow mirror with the prism removed. At first the observations were made with an 18° off-axis collimating mirror, which was rotated a few degrees in order to fill the grating with the radiation. A small improvement in the resolution was obtained later on by installing a 14° off-axis mirror. Two gratings were used in the spectrometer, which had ruled surfaces of about 2¼ by 3 inches and were ruled with 320 lines per inch and 180 lines per inch. The spectrometer is able to accommodate slightly larger gratings, which would give an increase in energy and resolution. The grating was placed in a holder which allowed adjustments of its position, so that a mercury line in a higher order could be brought sharply in focus at the exit slit.

The curvature of the entrance slit was not proper for the grating, but this did not reduce the resolution much because slits of 0.5 mm or larger were used for the region from 50 to 125 μ. However, better resolution will be obtained with straight slits. A thermocouple with a CsI window was used from 25 to 56 μ, and another thermocouple with a crystal quartz window was found to be suitable from 50 to 125 μ. It is planned to use a thermocouple with a diamond window from 25 to 125 μ, thus avoiding the changing of the thermocouple for the different regions of the spectrum.

Special attention is necessary to the problem of stray radiation in the long-wavelength region. The stray radiation was reduced to a few percent by the use of reflection filters and reststrahlen plates in place of the mirrors in the spectrometer. The optical system of the grating spectrometer is shown in figure 1 after the grating had been installed and the plane mirrors replaced by reflection filters. The two small plane mirrors, immediately in front of and behind the exit slit of the spectrometer, were replaced by two plane gratings, and the plane mirror in the source box of the spectrometer was replaced by a reststrahlen plate of NaCl, KBr, or CsBr. Also, three gratings could be used in place of the mirrors, but the reststrahlen plates are very useful in reducing second order spectra. A system which was as effective as the gratings and the reststrahlen plates in the removal of stray radiation consisted in the use of blackened silver mirrors which were first roughened with fine emory cloth. These reflection filters have been described previously [1].

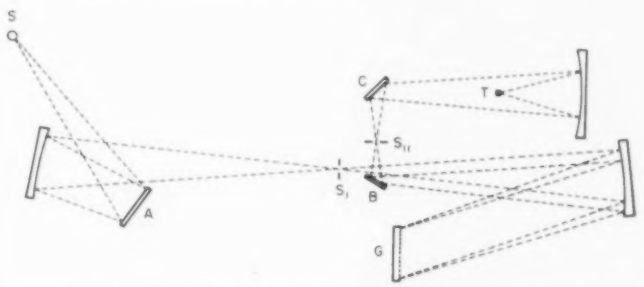

FIGURE 1. *The optical system of the grating spectrometer.*

A, B, and C are reflection filters which have replaced the mirrors of the spectrometer. G is the dispersion grating which is placed on the Littrow mirror mount, and T is the thermocouple with a quartz window.

[1] This work was done under a program of basic instrumentation, supported in part by the Office of Naval Research, Air Research and Development Command, and the Atomic Energy Commission.

[2] Figures in brackets indicate the literature references at end of this paper.

A study has been made of the efficiency of different types of filters for removal of stray radiation. The water-vapor spectrum from 45 to 70 μ was observed by the alternate use of several reflectors for the filter A of figure 1, the other parts of the spectrometer being unchanged during the comparisons. Figure 2 shows the results obtained for two gratings with 1,000 lines per inch, one roughened silver mirror, and a plate of NaCl. The zero line represents the recorder reading when an opaque shutter is placed in the beam. The water-vapor absorption at 139 cm^{-1}, under the atmospheric conditions of the observations, was 100 percent. By measuring how much the bottom of this absorption line is above the zero line an estimate of the stray radiation can be obtained. An estimate of the amount of the desired radiant energy reflected from the filter can be determined by measuring the difference between the deflection at the minimum of the line at 139 cm^{-1} and the maximum at 163 cm^{-1}. Grating 1 is the most efficient of the four filters tested. It has 1,000 lines per inch and the plane surface was almost completely cut away in the ruling so that the central image had about 1 percent reflection. The other grating

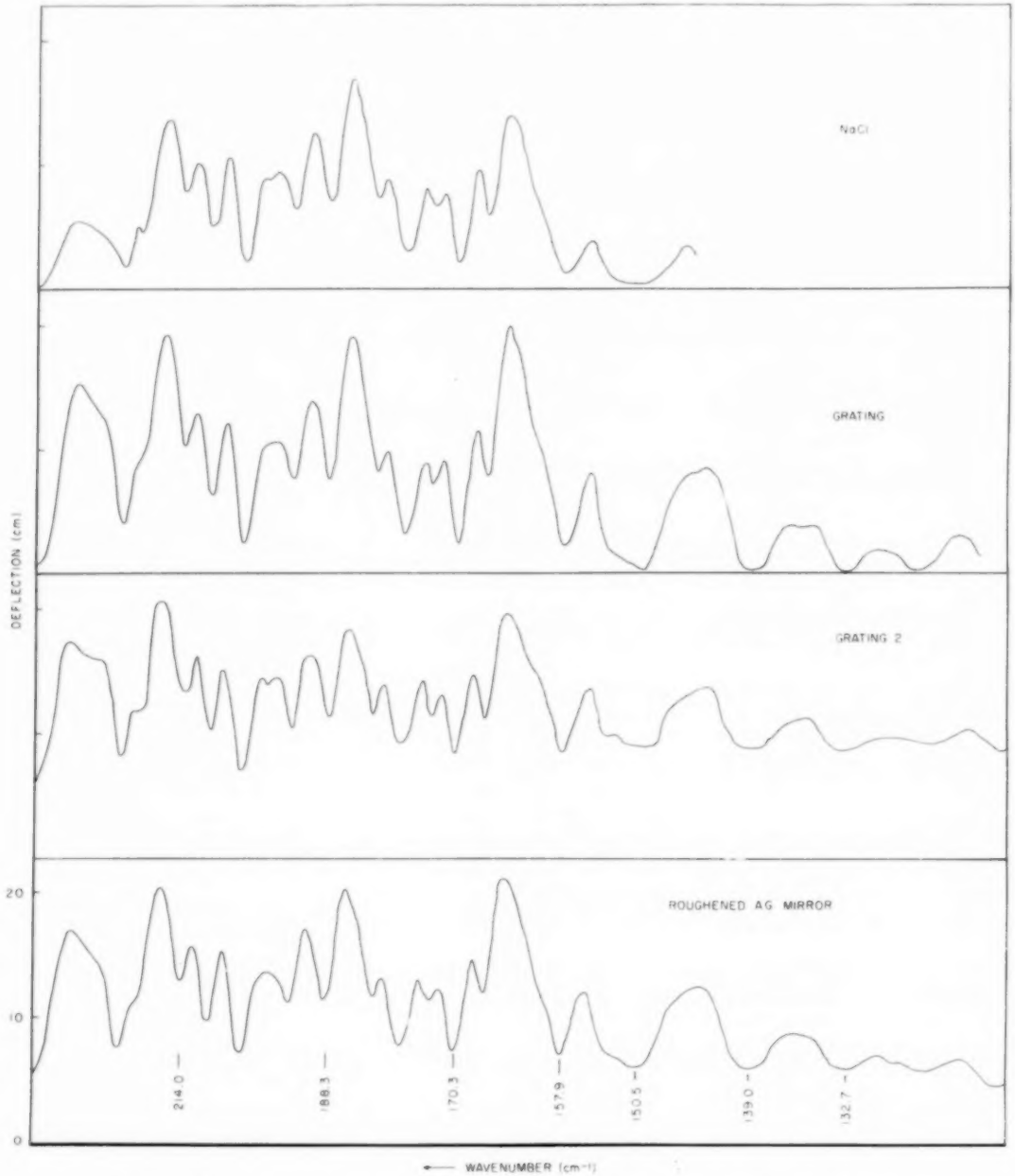

FIGURE 2. *A comparison of the efficiencies of different types of reflection filters.*

The base line for each filter represents the deflection with an opaque shutter in the beam.

(grating 11) had 1,000 lines per inch and the reflection for normal incidence was about 5 percent. Grating 11 is much less efficient in reducing the stray radiation. The roughened silver mirror does not reduce the desired energy appreciably but does allow considerable stray radiation to enter the spectrometer. The stray radiation can be made less for the silver filter by producing a greater amount of roughening on the surface, but this also reduces the desired energy. Reststrahlen plates of NaCl, KCl, KBr, and CsBr are efficient filters for the region from 45 to 125 μ. The spectral region of high reflection is limited to narrow bands and one material will not cover a wide range of the infrared spectrum. The CsBr reststrahlen plate is useful in measurements from 100 to 125 μ. The second-order spectrum is intense in this region from the 180-lines-per-inch grating and it is not removed by the grating filters or the roughened silver mirror.

Since the quartz window on the thermocouple absorbed the radiation from 5 to 40 μ, the second order from the grating did not overlap the first order except in the region from 90 to 125 μ when the roughened silver reflectors were used.

With these changes of the mirrors in the optical system just mentioned, it was found that sufficient energy for measurement could be observed from the globar source with the same amplifier that was used for the near infrared region.

The instrument has been tested and calibrated by the use of the water-vapor spectrum in the region from 25 to 125 μ. It has been found that the instrument can be used in three ways. First, by the use of the second and third orders of the 320- and 180-lines-per-inch gratings, high resolution can be obtained in the region from 25 to 50 μ. Second, the 320-lines-per-inch grating, with the thermocouple having a quartz window, gives good resolution in the first order from 50 to 70 μ. Third, the 180-lines-per-inch grating can be used from 50 to 125 μ. Gratings with various spacings can be used to obtain the best resolution in a particular region. One grating with 240 lines per inch would be suitable for the region from 50 to 100 μ.

3. Results

Figure 3 shows the water-vapor absorption lines from 23.5 to 33.5 μ as observed with the 320-lines-per-inch grating. The top curve is the second-order

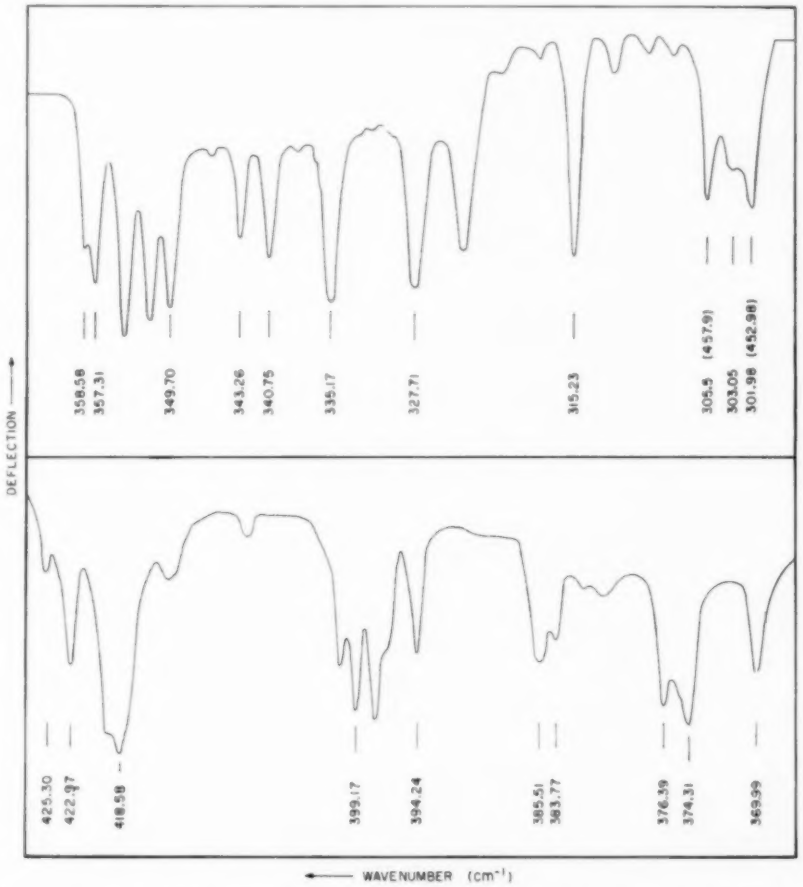

FIGURE 3. *The water vapor spectrum recorded with a 320-lines-per-inch grating.*

The upper curve is the second-order spectrum and the lower curve is the third-order spectrum. Overlapping of the two orders occurs at 305 cm^{-1}.

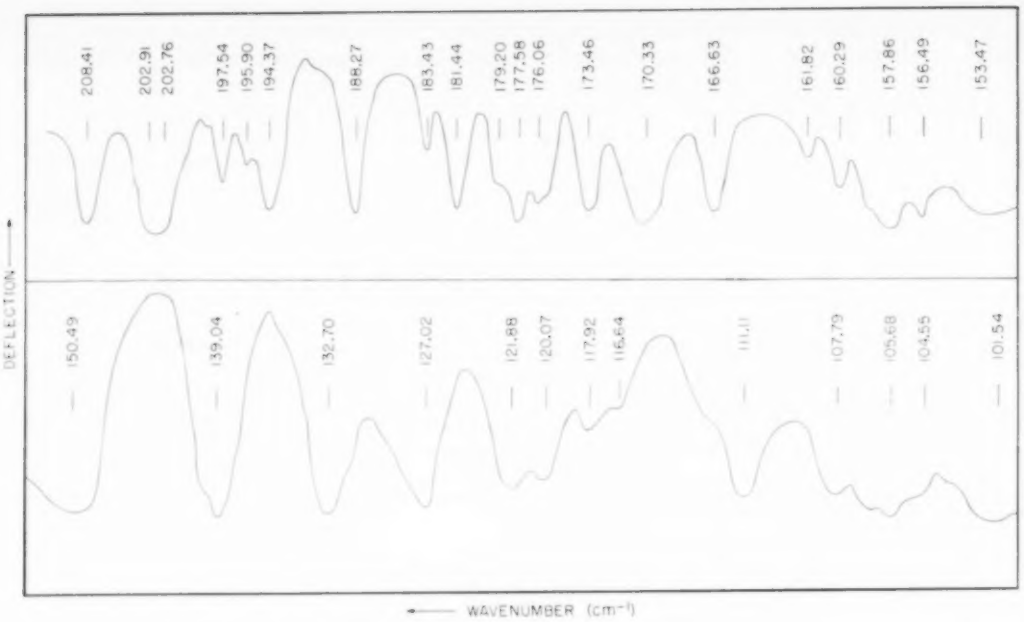

FIGURE 4. *The water vapor spectrum from 100 to 200 cm^{-1}.*

The upper curve is the first-order spectrum of water vapor from 150 to 200 cm^{-1} as observed with the 320-lines-per-inch grating. The lower curve is the water-vapor spectrum from 100 to 150 cm^{-1} as observed with a 180-lines-per-inch grating.

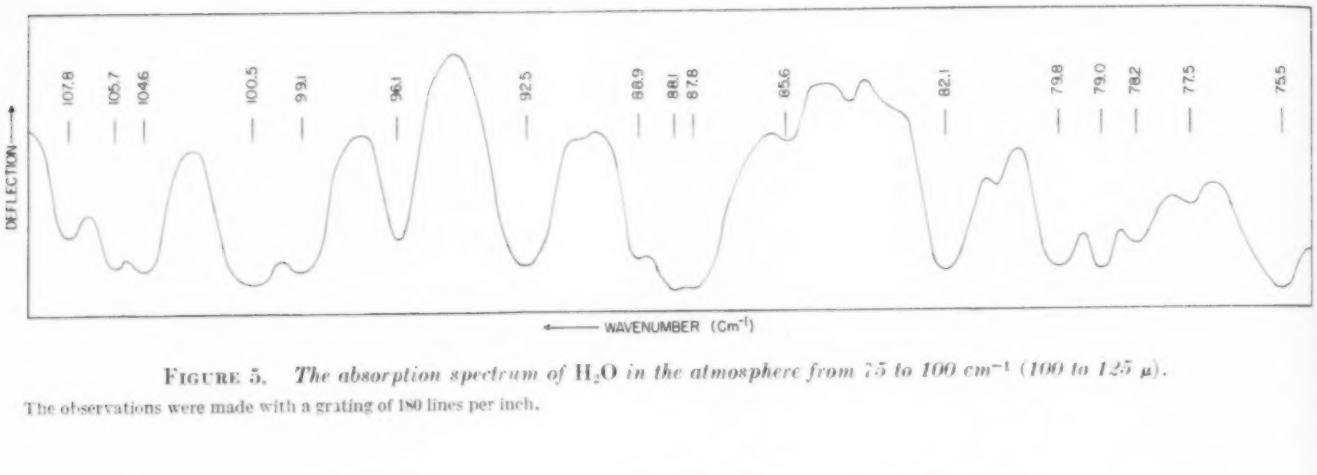

FIGURE 5. *The absorption spectrum of* H_2O *in the atmosphere from 75 to 100 cm^{-1} (100 to 125 μ).*

The observations were made with a grating of 180 lines per inch.

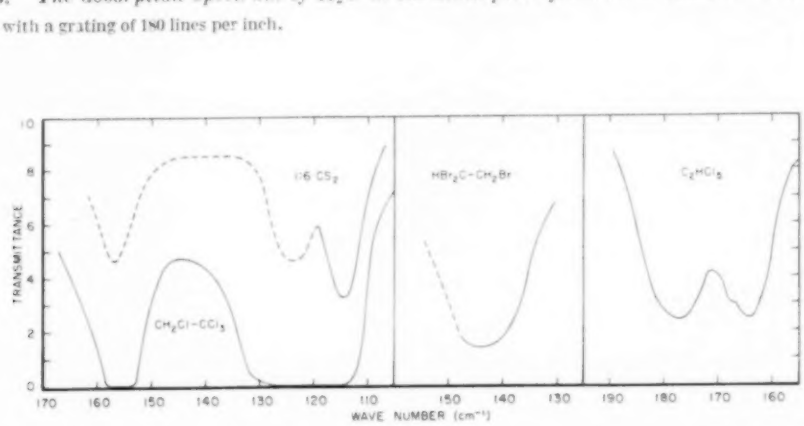

FIGURE 6. *Absorption bands of* CH_2 Cl–CCl_3, HBr_2 C–CH_2Br, *and* C_2 HCl_5 *in the region from 110 to 190 cm^{-1}.*

The cell thickness was 1 mm.

spectrum, and the bottom curve is the third-order spectrum. The five lines in the region of 395 cm^{-1} are well resolved by the instrument. The strong absorption line at 340 cm^{-1} was not reported in the earlier experimental work for this region, and this transition is predicted from the energy levels involved to have appreciable intensity. In the region of 300 cm^{-1} the third-order spectrum is overlapped by the second-order spectrum; this overlapping can be avoided by the use of a NaF reflector for this region.

Figure 4, upper curve, shows the region from 50 to 65 μ as observed with the 320-lines-per-inch grating, and the lower curve is for the region from 65 to 100 μ which was measured with the 180-lines-per-inch grating. Also the region from 100 to 125 μ, measured by the use of a CsBr reflector, is shown in figure 5. Slits of 1.8 mm were necessary for the measurements in this region.

The lines drawn above or below the spectrum represent the positions of the water-vapor lines as calculated from their energy levels. These wavenumbers are reduced to vacuum and have been published by Benedict, Claassen, and Shaw [3]. Only strong single lines have been used for the calibration, but the approximate positions of some complex lines are also listed on the figure. The lines were identified by using the wavenumbers obtained from the grating constant. While the water-vapor spectrum is of great value for calibration and testing of the instrument, it should be removed for the measurement of other spectra. This can be best accomplished by placing the spectrometer in a vacuum chamber. The absorption of the water vapor was greatly reduced by circulating dry nitrogen in the enclosure of the spectrometer. In the measurement of the absorption bands of liquids and vapors the removal of the water-vapor spectrum is essential to obtain band shapes.

The primary purpose of developing this instrument was to have available a spectrometer for measuring the absorption spectra of materials in the region from 50 to 125 μ. In the study of the vibrational bands of many molecules it was found that it was difficult to make a complete assignment of the different modes of vibration because several of the bending vibrations would be between 50 and 125 μ. Since the instrument has been in operation the long-wavelength spectra of C_2Cl_4, C_2Br_4, C_2F_3Br have been measured and their spectra analyzed. Cells with windows of crystal quartz, 0.2 mm in thickness, were used for these measurements. Many of the spectra of the substituted ethylenes, ethanes, and benzenes which contain fluorine, chlorine, bromine, or iodine will contain bands beyond 50 μ, and an instrument of this type will be of great value in obtaining sufficient data for a complete vibrational analysis. As an example of measurements on long-wavelength spectra figure 6 shows the absorption bands of CH_2Cl-CCl_3, $CHBr_2$-CH_2Br, and C_2HCl_5 between 50 and 100 μ. The longest wavelength band which was observed for these materials appeared at 114 cm^{-1}. With a cell of 1 mm thickness it was necessary to dilute CH_2Cl-CCl_3 with carbon disulfide in ratio 1 part to 6 so that the bands could be resolved.

The results that have been obtained demonstrate that spectra can be measured in the region from 50 to 125 μ with small gratings. For the arrangement with one grating of 200 to 240 lines per inch and a thermocouple with a quartz window, the costs should not be greater than $1,000. Where several gratings are employed and a vacuum enclosure with the necessary external controls is made, the cost would be greater. The number of gratings which will be employed and the changes in the filters for different regions will of necessity depend on the nature of the measurements which are being made. For the measurement of vibrational spectra and the transmittances of solids and liquids a single grating is adequate.

4. References

[1] N. Acquista and Earle K. Plyler, J. Opt. Soc. Am. **43,** 977 (1953).

[2] H. M. Randall, Rev. Sci. Instr. **3,** 196 (1932); T. King McCubbin and Wm. M. Sinton, J. Opt. Soc. Am. **40,** 537 (1950); R. A. Oetjen, W. H. Haynie, W. M. Ward, R. L. Hansler, H. E. Schauwecker, and E. E. Bell, J. Opt. Soc. Am. **42,** 559 (1952); L. Genzel and W. Eckhardt, Z. Physik **139,** 578 (1954).

[3] W. S. Benedict, H. H. Claassen, and J. H. Shaw, J. Research NBS **49,** 91 (1952) RP2347.

Washington, November 30, 1955.

Journal of Research of the National Bureau of Standards Vol. 56, No. 3, March 1956 Research Paper 2661

Surface Tension of Molten Glasses in the System Barium Oxide-Boric Oxide-Silica

Herman F. Shermer

The surface tension of 154 compositions in the system BaO-B_2O_3-SiO_2 were measured by a maximum pull-on-cylinder method, over the approximate range 900° to 1,300° C. The region of glass formation was investigated along with the adjacent regions. Several compositions were studied in the two-immiscible-liquid region. In this two-liquid region the lines of constant surface tension followed the tie lines in the phase diagram. Outside the two-liquid region the surface tension was increased by the addition of BaO and to a lesser degree by SiO_2. At 900° C the surface tension was relatively high near the composition corresponding to the $3BaO{\cdot}3B_2O_3{\cdot}2SiO_2$ compound, which has a melting point of 1,009° C.

1. Introduction

A study of the surface tension of the system BaO-B_2O_3-SiO_2 was undertaken as part of a comprehensive investigation of various physical properties of simple glass-forming systems [1 to 13].[1] The surface tension of the binary system, BaO-B_2O_3, has been reported as part of a previous investigation of the properties of the binary alkaline-earth borates [10]. The range of compositions studied was limited by crystallization and by relatively high viscosity in the region of high silica. The phase diagrams for the systems BaO-B_2O_3 and BaO-B_2O_3-SiO_2 show a two-liquid region at low concentrations of alkaline-earth oxide.

The system BaO-B_2O_3-SiO_2 is of fundamental importance in the ceramic field and especially in the glass industry, as it serves as a starting point for investigations of a large class of barium-crown glasses.

2. Experimental Procedure

2.1. Preparation of Glasses

The composition of the glasses used in this investigation is shown in table 1. The glasses were made by melting at 1,300° to 1,500° C the required amounts of chemicals in platinum crucibles and stirring the melts with platinum stirrers until they appeared homogeneous. The melts varied in weight from 100 to 500 g.

Chemical-analysis samples were taken from the melts before and after surface-tension measurement. The reported compositions are the average of the two determinations unless otherwise noted in table 1. The BaO and SiO_2 contents were determined gravimetrically and the B_2O_3 by difference. Small changes were noted between the batch composition and the first analysis. A further loss of a few tenths of a percent of B_2O_3 was noted between the two analyses, indicating volatilization during the tests. The estimated probable errors of the gravimetric determinations are about ±0.1 weight percent.[2]

2.2. Method of Test

The method of measuring surface tension used in this investigation has been previously described in detail [14]. It consists in determining the pull exerted by the test surface on a thin-walled platinum cylinder during the removal of its lower edge from contact with the liquid. The first determination of the surface tension of any melt was made at 1,300° C. Subsequent measurements were made at 100-deg C intervals, decreasing the temperature until the glass was too viscous to yield in a reasonable time or until crystallization occurred.

The density values used in the correction of the surface-tension calculations were determined by interpolation between room-temperature values for each composition and a few known values in the temperature and composition range of interest. For convenience in presenting the data, all values of surface tension have been adjusted to even 100-deg intervals. The temperature of any measurement may have been 4 deg C from that given in table 1.

3. Results and Discussion

Surface-tension data are given in table 1. Differences in batch materials and source of glasses are indicated in the footnotes. Figure 1 shows the isoepitatic [15], or constant surface-tension, lines at 1,300° C and the locations of the compositions investigated. The surface tension increased with decrease in B_2O_3 content. This figure also contains an outline of the two-immiscible-liquid region and the conodes, i. e., the tie lines connecting the two conjugate compositions in the phase diagram as determined by Levin and Ugrinic [16].

In the two-liquid region the isoepitatic lines approximate the conodes. This is in accord with the

[1] Figures in brackets indicate the literature references at the end of this paper.

[2] The samples were analyzed by Ralph I. Cohen, Ernest B. Clark, and J. Richard Spann of the Bureau.

TABLE 1. *Surface tension of composition in the system* $BaO-B_2O_3-SiO_2$

Composition[a]			Surface tension[b]				
BaO	B_2O_3	SiO_2	1,300° C	1,200° C	1,100° C	1,000° C	900° C
wt %	*wt %*	*wt %*	*d/cm*	*d/cm*	*d/cm*	*d/cm*	*d/cm*
[c] 0.0	100.0	.....	.....	.....	88.2	83.5	80.5
[c] 4.3	95.7	.....	96.3	93.4	88.6	84.0	80.0
[c] 4.9	95.1	.....	94.8	90.9	86.3	82.8	.....
[c]15.5	84.5	.....	96.3	91.8	87.2	82.4	79.4
[c]24.9	75.1	.....	106.3	99.8	92.1	89.9	88.1
30.1	69.9	.....	121.6	119.8	116.4	114.7	115.3
[c]32.3	67.7	.....	122.2	123.0	117.8	116.2	.....
35.0	65.0	.....	134.3	133.4	133.3	136.9	140.7
[c]35.8	64.2	.....	135.4	137.6	137.5	141.0	145.7
36.6	63.4	.....	139.7	140.7	142.1	145.8	150.5
[c]40.8	59.2	.....	156.0	157.9	161.1	165.8	171.4
41.8	58.2	.....	163.8	166.6	170.4	174.7	.....
41.9	58.1	.....	163.5	168.9	172.4	177.0	.....
[c]45.3	54.7	.....	180.6	183.3	187.3	192.3	197.2
47.2	52.8	.....	190.0	192.2	197.0	202.4	211.0
[c]47.6	52.4	.....	190.7	193.7	198.0	202.9	207.3
[c]51.0	49.0	.....	203.5	207.4	211.2	216.1	220.6
51.4	48.6	.....	206.5	210.1	213.8	218.9	.....
51.5	48.5	.....	207.3	211.0	214.6	219.3	224.1
52.4	47.6	.....	208.9	212.1	216.8	221.3	.....
53.6	46.4	.....	212.5	216.6	221.2	226.9	.....
[c]55.6	44.4	.....	220.7	224.8	228.9	233.7	239.0
56.1	43.9	.....	219.6	224.5	229.4	235.4	.....
56.4	43.6	.....	221.1	227.0	232.0	238.3	.....
60.0	40.0	.....	234.0	239.1	244.4	251.2	.....
60.2	39.8	.....	234.8	240.4	246.0	252.7	.....
[c]60.4	39.6	.....	231.9	237.3	243.2	248.4	.....
[c]65.1	34.9	.....	242.9	251.1	257.4	263.4	.....
[c]70.1	29.9	.....	252.4	261.7	269.0	275.1	.....
[c]74.2	25.8	.....	263.4	274.0	282.4	288.9	.....
[c]79.5	20.5	.....	263.9	305.2	314.6	321.6	.....
2.1	92.9	5.0	99.3	93.3	.....	87.1	84.9
4.9	84.1	11.0	107.1	103.3	97.9	92.8	93.9
[d]10.4	77.2	12.4	113.8	108.2	103.8	100.5	97.0
[d]10.4	65.0	24.6	133.5	128.7	121.5	117.9	116.0
[d]10.6	52.9	36.5	152.5	148.6	145.7	143.8	.....
[d]22.8	65.0	12.2	133.4	126.7	118.8	114.8	114.0
[d]23.5	52.9	23.6	146.5	140.4	141.0	140.2	137.3
[d]22.0	41.4	36.6	174.1	175.2	.....	.....	.....
29.8	67.2	3.0	123.7	119.6	113.8	110.9	110.1
29.6	61.2	9.2	132.8	128.9	123.5	118.2	124.9
30.7	57.7	11.6	142.0	138.9	135.7	132.6	135.4
31.2	63.2	5.6	132.4	128.9	126.5	125.5	124.9
33.8	20.4	45.8	241.9	.....	.....	.....	.....
[d]35.5	40.2	24.3	185.2	182.9	178.1	.....	.....
36.9	57.4	5.7	153.2	155.2	155.2	158.8	167.2
37.0	45.9	17.1	178.7	179.8	181.3	182.6	187.0
37.3	51.6	11.1	164.0	165.6	167.0	170.2	179.8
37.4	39.2	23.4	193.4	194.2	193.5	193.7	.....
42.1	55.3	2.6	172.4	175.6	178.7	184.0	.....
42.2	52.5	5.3	178.5	181.7	185.9	191.1	197.6
42.3	49.6	8.1	182.5	186.2	187.5	193.8	200.9
42.3	46.8	10.9	188.8	193.7	197.7	202.5	212.0
42.7	43.6	13.7	196.1	199.6	202.7	207.7	216.4
42.6	43.6	13.8	196.6	199.0	202.2	206.1	216.8
42.7	40.7	16.6	203.6	206.6	209.7	214.3	221.3
42.8	37.8	19.4	211.6	212.5	215.5	219.8	226.2
43.0	34.3	22.7	219.2	220.5	221.8	225.2	231.2
43.0	31.9	25.1	224.0	225.7	226.0	229.8	235.1
43.2	28.9	27.9	233.7	235.6	236.6	241.5	.....
43.1	28.9	28.0	232.9	234.3	235.1	238.5	.....
43.2	26.0	30.8	241.4	241.6	241.1	.....	.....
47.6	47.2	5.2	202.7	205.7	210.2	214.4	221.1
47.6	44.6	7.8	206.2	211.0	214.8	219.6	227.6
47.8	41.7	10.5	213.2	216.9	220.6	225.9	234.5
48.1	36.0	15.9	227.1	229.6	232.2	236.9	243.6
48.5	30.5	21.0	241.2	243.8	246.9	251.6	260.3
48.1	30.4	21.5	240.4	243.1	246.6	252.4	260.5
48.3	27.7	24.0	245.8	248.7	252.6	257.5	264.6
48.4	27.4	24.2	246.4	249.8	252.7	257.5	264.2
48.5	24.7	26.8	254.1	257.1	255.8	262.8	272.8
48.7	21.6	29.7	261.9	264.1	265.3	269.9	274.9
48.9	18.7	32.4	270.0	272.0	273.4	277.3	282.6
49.5	12.5	38.0	291.9	291.8	291.4	294.6	.....
49.3	9.7	41.0	302.1	301.9	302.0	.....	.....
49.7	6.2	44.1	318.4	.....	.....	.....	.....
51.4	15.3	33.3	284.0	285.5	286.2	290.5	.....
51.7	46.4	1.9	212.1	215.7	219.6	225.4	229.3
51.8	44.7	3.5	215.9	219.4	223.2	228.2	233.6
50.5	43.2	5.3	219.6	223.3	227.0	231.4	238.7
52.0	42.3	5.7	220.3	224.0	227.6	232.7	239.6
52.0	39.1	8.9	226.6	230.7	234.3	239.7	247.7
52.2	37.8	10.0	228.1	231.9	235.8	241.2	248.3
52.0	36.9	11.1	230.9	234.3	238.2	242.6	249.5
52.3	36.6	11.1	228.8	232.1	236.5	240.6	247.6
52.2	36.4	11.4	231.4	235.0	238.7	243.3	246.3
52.5	35.3	12.2	229.0	231.9	235.8	240.5	245.9
52.4	33.7	13.9	235.3	240.7	244.3	249.3	256.9
52.7	31.9	15.4	242.5	246.1	250.3	254.6	260.6
52.8	30.7	16.5	243.3	248.1	251.7	256.4	264.2
53.1	26.5	20.4	255.2	258.7	262.2	266.5	271.5
53.1	25.0	21.9	257.1	260.5	263.9	269.0	274.6
52.7	24.1	23.2	261.3	264.2	267.1	272.4	280.9
53.3	22.4	24.3	265.0	267.4	270.3	275.4	279.5
53.5	19.4	27.1	272.9	275.6	278.8	282.8	294.6
53.4	18.3	28.3	276.9	279.2	282.2	284.9	289.1
53.6	16.9	29.5	270.3	273.0	275.7	279.0	282.8
53.6	15.5	30.9	283.9	283.3	285.1	287.1	297.3
53.7	12.6	33.7	292.6	.....	.....	.....	.....
54.1	8.2	37.7	313.0	.....	.....	.....	.....
54.7	24.3	21.0	265.1	265.5	268.9	273.0	278.1
55.2	25.9	18.9	258.3	261.8	265.7	270.6	276.0
56.1	41.6	2.3	227.6	231.4	236.1	242.1	247.8
56.4	38.7	4.9	232.4	236.5	241.9	246.8	253.5
56.9	35.9	7.2	238.8	243.2	247.3	252.0	257.7
56.9	33.2	9.9	241.5	246.2	251.1	256.7	264.3
57.3	33.7	9.0	244.8	249.6	254.3	259.6	268.0
56.9	30.8	12.3	248.3	253.0	258.3	263.0	269.0
57.1	30.7	12.2	248.5	252.6	257.5	261.8	267.3
57.1	28.1	14.8	254.2	258.9	263.4	268.2	275.1
57.3	28.0	14.7	254.4	259.3	264.1	269.0	275.1
57.4	25.3	17.3	261.7	266.5	270.3	274.8	282.0
57.5	22.8	19.7	268.0	271.5	274.7	279.5	286.7
58.6	19.9	21.5	277.1	281.2	284.9	288.9	297.3
57.5	20.1	22.4	272.6	277.2	280.5	285.5	294.0
58.8	17.4	23.8	287.8	290.1	.....	.....	.....
57.7	17.4	24.9	277.1	282.2	285.4	288.8	296.1
58.5	26.3	15.2	260.9	265.7	270.6	276.0	283.4
58.0	12.2	29.8	297.8	301.6	304.7	.....	.....
58.5	6.2	35.3	325.6	.....	.....	.....	.....
58.4	35.7	5.9	242.7	247.7	253.0	258.8	265.6
59.6	37.5	2.9	238.3	243.9	249.6	255.4	.....
60.4	37.4	2.2	239.0	246.6	252.2	257.6	.....
60.5	34.9	4.6	244.0	250.1	255.9	261.3	268.3
60.7	32.4	6.9	249.5	255.3	261.0	267.1	272.6
60.8	29.8	9.4	254.2	260.5	266.8	272.3	277.8
61.1	27.0	11.9	260.8	266.5	271.9	277.5	284.1
61.2	24.4	14.4	265.7	271.7	277.5	282.5	290.0
61.5	21.6	16.9	272.8	278.7	283.9	287.4	295.4
61.7	19.2	19.1	279.5	284.9	289.5	293.2	304.0
61.5	18.3	20.2	284.2	289.4	292.5	297.5	304.0
61.8	16.7	21.5	287.6	292.6	296.9	299.5	.....
62.0	14.2	23.8	286.2	290.9	304.3	.....	.....
62.0	11.6	26.4	306.6	311.1	313.5	.....	.....
62.4	9.0	28.6	318.8	322.1	.....	.....	.....
62.6	5.8	31.6	335.5	.....	.....	.....	.....
64.1	31.3	4.6	252.8	259.3	265.5	271.7	.....
64.3	28.9	6.8	256.2	263.5	269.8	270.1	.....
64.9	26.1	9.0	262.9	269.9	276.3	281.6	288.1
65.2	21.1	13.7	275.7	282.2	288.1	293.0	299.4
64.9	21.2	13.9	275.3	282.1	287.9	293.0	299.6
65.2	18.8	16.0	280.6	286.6	292.6	296.4	307.9
65.2	18.7	16.1	283.0	288.7	293.3	297.9	311.4
65.5	16.1	18.4	289.0	295.3	300.3	305.4	.....
65.6	16.1	18.3	289.2	296.1	300.5	305.6	.....
65.5	13.7	20.8	299.9	305.3	309.0	.....	.....
65.8	10.9	23.3	309.7	314.3	324.4	.....	.....
67.8	19.9	12.3	280.2	287.0	293.0	298.2	302.7
68.0	17.3	14.7	287.7	294.2	299.8	304.4	.....
67.8	15.4	16.8	295.8	302.0	307.6	311.9	.....
69.8	19.3	10.9	282.9	290.1	296.3	302.5	.....
70.0	17.0	13.0	289.9	297.4	303.6	309.2	.....
70.6	14.1	15.3	298.3	305.8	311.6	316.9	.....

[a] Average composition of before and after analyses except for two-liquid compositions, which are batch compositions except as noted by footnote d.

[b] Interpolated values. The temperature of any measurement may have been ±4°C from that given here.

[c] Glasses from binary alkaline-earth borate investigation [10].

[d] Average composition of two-liquid glasses made primarily for this investigation. Analyzed values before surface-tension measurement. Glasses not indicated by footnotes c or d were from an investigation of various properties of the system $BaO-B_2O_3-SiO_2$ by Hamilton, Cleek, and Grauer [17].

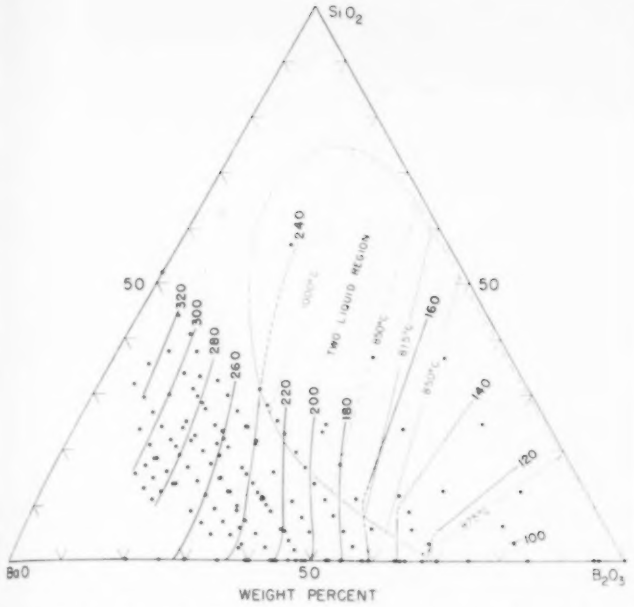

FIGURE 1. *Isoepitatic (constant surface-tension) lines of the system* $BaO\text{-}B_2O_3\text{-}SiO_2$ *at 1,300° C and locations of compositions studied.*

The outline of the two-liquid immiscibility region after Levin and Ugrinic [16].

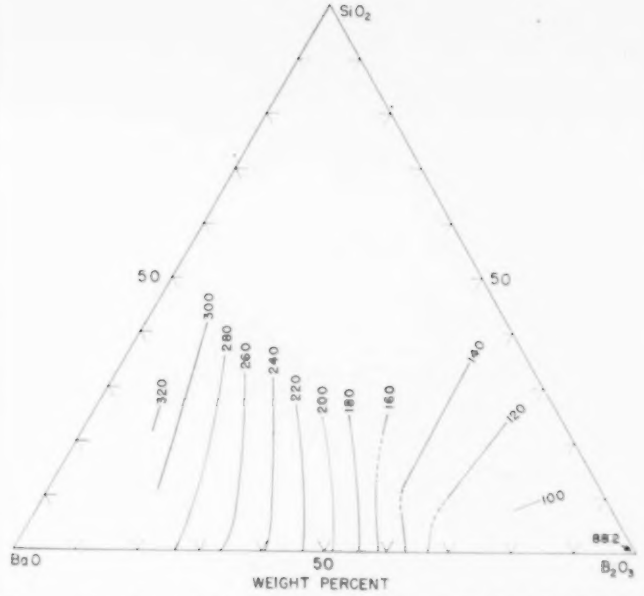

FIGURE 2. *Isoepitatic lines of the system* $BaO\text{-}B_2O_3\text{-}SiO_2$ *at 1,100° C.*

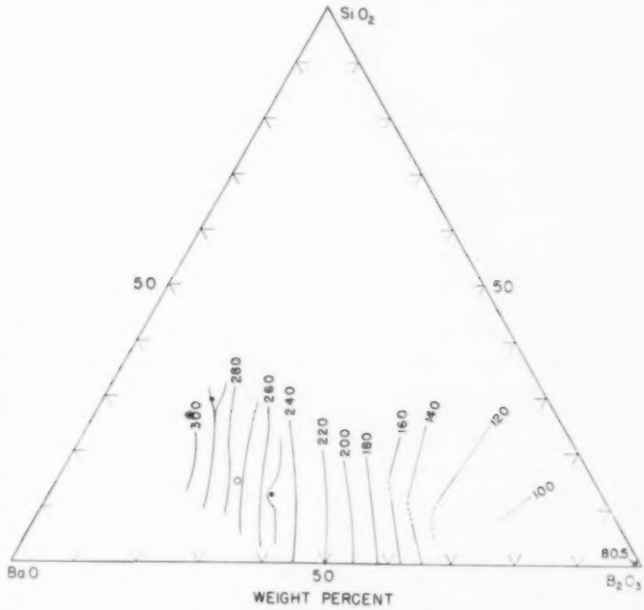

FIGURE 3. *Isoepitatic lines of the system* $BaO\text{-}B_2O_3\text{-}SiO_2$ *at 900° C.*

The open circle indicates the location of the $3BaO\text{-}3B_2O_3\text{-}2SiO_2$ compound, identified by Levin and Ugrinic [16]. The two closed circles indicate the locations of the low-surface-tension areas.

fact that at any given temperature the upper layer of all compositions along a conode is identical. The lighter liquid will tend to rise to the surface, but if there were incomplete separation, there may be some of the lower liquid in the upper layer. The completeness of separation becomes greater as one departs from the two-liquid interface; and at the surface, where the surface tension is measured, the minimum amount of the lower layer will be present. The presence of lower liquid in the upper liquid is indicated by opacity. The glass that adhered to the ring was clear, indicating the probable absence of any of the lower liquid in the surface under test. Therefore, surface measurements may give a good indication of the direction of the conodes in the two-liquid region, and surface-tension measurements may offer another approach to the study of phase equilibria in the two-liquid region.

Figure 2 shows the isoepitatic lines at 1,100° C. A comparison with the previous figure shows a slight counterclockwise rotation of the lines within the two-liquid region. This is in accord with the rotation of the conodes with temperature reported in the phase work.

Figure 3 shows a plot of the isoepitatic lines at 900° C. The changes in surface tension between 1,100° and 900° C are similar to those between 1,300° and 1,100° C.

The constant surface-tension lines near the composition corresponding to the $3BaO\text{-}3B_2O_3\text{-}2SiO_2$ compound deviate from simple curves. This compound was characterized by Levin and Ugrinic [16] as one that melts congruently at 1,009° C and whose primary field occupies a large portion of the glass-forming region of the system. This is 109 deg C above the temperature of the present measurement. The deviation of the isoepitatic lines is associated with an irregular surface-tension region near the compound (indicated by the open circle) and two relatively low surface-tension areas (closed circles).

Above the liquidus temperature (1,009° C) at the compound composition no departures of the isoepitatic lines were observed. The possibility of the formation of crystals may be the cause of these

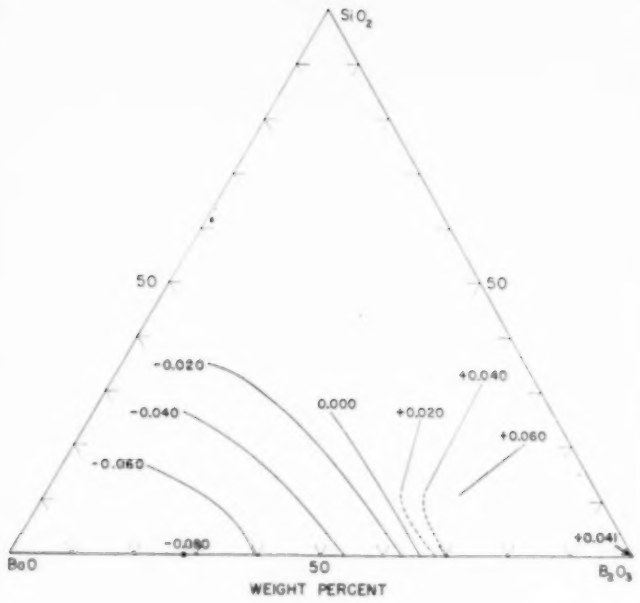

FIGURE 4. *Constant coefficient of surface-tension lines of the system* $BaO\text{-}B_2O_3\text{-}SiO_2$ *across the range 1,000° to 1,300° C.*

deviations from simple curves. Microscopic examination of the glasses has shown no sign of crystallization, and the region about the compound is known to produce quite stable glasses, i. e., the rate of crystal growth in this region is very low. No explanation is available for the minima.

Figure 4 shows the lines of constant-temperature coefficient of surface tension over the range 1,000° to 1,300° C. With decreasing temperature there is a decrease in surface tension within the two-liquid region and an increase over most of the area exterior to this region. The scatter of the points and the small range of the coefficients made it difficult to determine the exact position of the lines. For example, points with the value −0.040 (dyne/cm)/° C are found in about three-fourths of the area between the −0.020 and −0.060 (dyne/cm)/° C lines. The lines shown are correspondingly uncertain. The two-liquid region is characterized by the similarity between the constant coefficient lines and the conodes in the phase diagram. There is a maximum coefficient in this region, and a zero coefficient near the boundary. The values indicated in this figure are the average over the temperature range.

The surface-tension versus temperature curve for any particular composition is not a straight line and may contain inflections. In the region around the 0.000 (dyne/cm)/° C line the curves may show maxima, minima, or both. It may also be seen from this figure that a change in composition in a given direction does not always cause a similar change in the coefficient of surface tension, and as noted earlier, it does not always cause a similar change in surface tension.

4. Summary and Conclusions

The surface tension of a series of $BaO\text{-}B_2O_3\text{-}SiO_2$ compositions was measured over the range 900° to 1,300° C. In the two-liquid region the values of surface tension and the coefficients of surface tension followed the conodes in the phase diagram, indicating a possible new technique for phase study in this type of region. In general, the surface tension increased with decrease in B_2O_3 content. At 900° C the lines of constant surface tension reflected an irregularity near the composition corresponding to the $3BaO.3B_2O_3.2SiO_2$ compound, which has a melting point of 1,009° C.

5. References

[1] Leo Shartsis, Sam Spinner, and Alden W. Smock, Surface tensions of compositions in the systems $PbO\text{-}B_2O_3$ and $PbO\text{-}SiO_2$, J. Am. Ceram. Soc. **31,** 23 (1948); J. Research NBS **40,** 61 (1948) RP1855.

[2] Leo Shartsis and Edwin S. Newman, Some energy relationships in the systems $PbO\text{-}B_2O_3$ and $PbO\text{-}SiO_2$, J. Am. Ceram. Soc. **31,** 213 (1948); J. Research NBS **40,** 471 (1948) RP1893.

[3] Leo Shartsis and Rodrigo Canga, Surface tension of molten zinc borates, J. Research NBS **43,** 221 (1949) RP2023; Ceram. Abstr. p. 110i. (1950).

[4] Leo Shartsis and Sam Spinner, Surface tension of molten alkali silicates, J. Research NBS **46,** 385 (1951) RP2209.

[5] Leo Shartsis, Sam Spinner, and Webster Capps, Density, expansivity, and viscosity of molten alkali silicates. J. Am. Ceram. Soc. **35,** 155 (1952).

[6] Leo Shartsis and Webster Capps, Surface tension of molten alkali borates, J. Am. Ceram. Soc. **35,** 169 (1952).

[7] Leo Shartsis, Webster Capps, and Sam Spinner, Density and expansivity of alkali borates and density characteristics of some other binary glasses, J. Am. Ceram. Soc. **36,** 35 (1953).

[8] L. Shartsis, W. Capps, and S. Spinner, Viscosity and electrical resistivity of molten alkali borates, J. Am. Ceram. Soc. **36,** 319 (1953).

[9] L. Shartsis, and W. Capps, Energy relations in binary alkali borates, J. Am. Ceram. Soc. **37,** 27 (1954).

[10] Leo Shartsis and H. F. Shermer, Surface tension, density, viscosity, and electrical resistivity of molten binary alkaline-earth borates, J. Am. Ceram. Soc. **37,** 544 (1954).

[11] C. E. Weir and L. Shartsis, Compressibility of binary alkali borate and silicate glasses at high pressures, J. Am. Ceram. Soc. **38,** 299 (1955).

[12] C. E. Weir and L. Shartsis, Compressibility of binary alkaline-earth borate glasses at high pressures (unpublished manuscript).

[13] Herman F. Shermer, Thermal expansion of binary alkaline-earth borate glasses, J. Research NBS **56,** 73 (1956) RP2650.

[14] Leo Shartsis and A. W. Smock, Surface tensions of some optical glasses, J. Am. Ceram. Soc. **30,** 130 (1947).

[15] Edward W. Washburn, George Reed Shelton, and Earl E. Libman, The viscosities and surface tensions of the soda-lime-silica glasses at high temperatures (University of Illinois, Engineering Experiment Station Bulletin 140, 1924).

[16] Ernest M. Levin and George M. Ugrinic, The system barium oxide-boric oxide-silica, J. Reserach NBS **51,** 37 (1953) RP2430.

[17] Edgar H. Hamilton, G. W. Cleek, and O. H. Grauer, Some properties of $BaO\text{-}B_2O_3\text{-}SiO_2$ glasses and a theory of glass structure (unpublished manuscript).

WASHINGTON, December 2, 1955.

Journal of Research of the National Bureau of Standards Vol. 56, No. 3, March 1956 Research Paper 2662

Relationship Between Crystal Orientation and Stress-Corrosion Cracking in Alpha and Beta Brasses

Hugh L. Logan

The crystallographic planes bounding intercrystalline stress corrosion cracks in two large-grained Alpha brasses and those followed by transcrystalline stress-corrosion cracks in large-grained beta brass were determined by X-ray diffraction methods. Intercrystalline stress-corrosion cracking in the alpha brasses originated between grains that, because of their relative orientation, had high interfacial energy contents. It is the relative orientation, not the crystallographic type, that determines the susceptibility to stress-corrosion cracking of alpha brass in grain boundaries approximately normal to the applied stress. Transcrystalline stress-corrosion cracking of beta brass occurred in grains that were oriented most favorably for slip, and in planes that were approximately normal to the applied stress. No plane or family of planes in beta brass was found to be particularly susceptible to stress-corrosion cracking. It is postulated that in each case cracking progressed by a film rupture mechanism.

1. Introduction

Stress-corrosion cracking, or season cracking, in brass was first reported in 1906 [*1*].[1] It has been the subject of many investigations and several comprehensive bibliographies have been published [*2*, *3*]. The study of the stress corrosion of brass is particularly important from a mechanistic point of view because stress-corrosion cracking is predominantly intercrystalline in the face-centered alpha brass and mainly transcrystalline in the body-centered, ordered beta brass.

If corrosion occurs in unstressed alpha brass, it is generally of the pitting type; only two reports [*4*, *5*] of intercrystalline corrosion have come to the author's attention. However, if the material is exposed under sufficiently high residual or applied tensile stress in an atmosphere containing ammonia and water vapor (the specific corrodent for brass), predominantly intercrystalline stress-corrosion cracks will develop.

An excellent discussion of the mechanism of stress corrosion in alpha brass was presented by Read, Reed, and Rosenthal [*6*] at the ASTM–AIME Symposium on Stress Corrosion in 1944. Read et al proposed the hypothesis that the grain-boundary regions in this brass have higher energy contents than the grain interiors, and therefore the grain boundaries have a greater susceptibility to corrosion. These workers discounted the possibility of a grain-boundary precipitate but suggested that lattice imperfections may explain the higher energy at the grain boundaries. In 1950 Robertson [7] suggested that relative grain orientation could be a factor in materials susceptible to intercrystalline stress-corrosion cracking. So far as the author knows, explanations of the mechanism of the transcrystalline stress-corrosion cracking of beta brass have not reached the same stage of development as those for alpha brass.

Following World War II a great deal of interest developed in the study of metal boundaries or interfaces and the results of a number of investigations were summarized in a symposium, "Metal Interfaces" [*8*], published in 1952. In this symposium it was pointed out that interfacial or grain-boundary energy is a function of the difference in orientation between the grains [*9*]. A number of investigators have shown that the interfacial energy increased to maximum values with increased difference in angular orientation between pairs of crystals for angles ranging from 12° for tin [*10*] to 29.8° for an iron-silicon alloy [*11*]. If the grain-boundary energy, and therefore the chemical activity of grain boundaries in alpha brass, increases with increased difference in orientation of adjacent grains, it is to be expected that the probability that a stress-corrosion crack would develop at a particular grain boundary would depend on the relative orientation (or degree of misfit) of the crystals meeting at that boundary. Cracks should occur most frequently between crystals whose relative orientations were in the range in which maximum grain-boundary energies have been obtained for other metals and may be expected for brass.

It is postulated that there is a greater probability of corrosive attack at the grain boundaries having the highest interfacial energies than at other points on the surface of the brass. The corrosive attack at these grain boundaries would form sharp notches. Those notches that were most favorably oriented with respect to the stress pattern in the metal would then act as points of stress concentration that would produce eventual rupturing of the protective film on the metal at the root of the notch. Stress-corrosion cracking would then proceed by a film-rupture mechanism, as discussed in an earlier paper [*12*].

As a part of the current study of the mechanism of stress-corrosion cracking, the crystallographic planes bounding stress-corrosion cracks at their origin and the angles between the crystallographic planes in the crystals on opposite sides of stress-corrosion cracks have been determined for specimens of two compositions of alpha brass.

[1] Italic figures in brackets indicate the literature references at the end of this paper.

375523—56——4

It is generally accepted that, in the two-phase alloy, stress-corrosion cracks will be intercrystalline in the alpha phase and transcrystalline in the beta phase. The stress corrosion of beta brass has not been as extensively studied as that of alpha brass. However, from the observations of stress-corrosion cracking in the two-phase system it has generally been considered that stress-corrosion cracking would be transcrystalline in a single-phase beta alloy. As a part of a study to determine why stress-corrosion cracking was intercrystalline in alpha brass and transcrystalline in beta brass, the crystallographic planes on which the transcrystalline stress-corrosion cracks had their origin were also determined for several specimens of large-grained beta brass.

2. Materials and Experimental Procedure

The two alpha brass alloys studied had the nominal compositions of 90 percent Cu-10 percent Zn (commercial bronze) and 70 percent Cu-30 percent Zn (cartridge brass). The beta brass had a composition of approximately 50 percent Cu-50 percent Zn. Ingots of these alloys approximately 1 by 1 by 8 in., cast in sand molds, had grain diameters ranging from ⅛ to ¼ in. Sections containing equiaxial crystals were selected from these ingots for this investigation. In addition to these three cast alloys, large-grained specimens of the 90 percent Cu-10 percent Zn alloy were prepared by the strain-anneal method and were also used in this investigation.

Specimens having the shape and dimensions shown in figure 1 were machined from the ingots and the rod. The flat surfaces of the specimens were repeatedly polished (using 000 metallographic polishing paper) and etched until Laue back reflection X-ray patterns indicated that the surfaces were free from cold-work. The end sections were then coated with a waterproof lacquer, leaving only the central 2 in. exposed to the corrosive medium. The specimens were loaded in tension under a stress of 5,000 to 6,000 lb/in.^{2} and exposed in an atmosphere containing ammonia, water vapor, carbon dioxide, and air until stress-corrosion cracks appeared. Two surfaces, at right angles to each other, of a specimen of alpha brass containing stress-corrosion cracks are shown in figure 2.

To determine the crystallographic plane or planes bounding or followed by stress-corrosion cracks, the cracks studied should extend continuously from one surface of the specimen into an adjoining surface at right angles to the first. It is also necessary that the two crystals bounding the crack be continuous, so that surfaces A_1 and A_2, figure 3, be surfaces of the same crystal machined at right angles to each other. Laue back reflection X-ray photographs were made of the crystal surfaces A_1 and A_2 of crystal A and projections of these surfaces, relative to their respective cubic axes, were plotted on stereographic nets, using the method described by Greninger [13]. The plot of surface A_2, figure 3, was rotated through 90 deg about the N–S axis of the net, and the net was then superimposed on that for surface A_1. If the cubic poles of the two nets coincided (within the experimental error), the surfaces A_1 and A_2 were

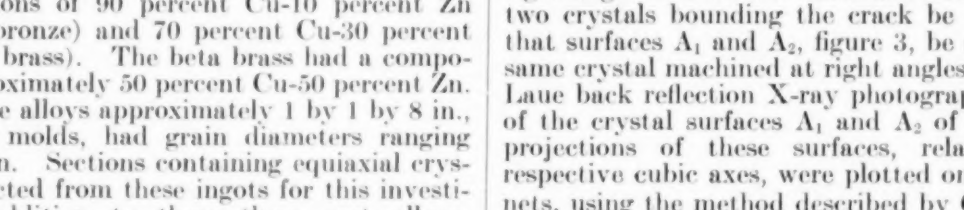

FIGURE 1. *Stress-corrosion specimen.*

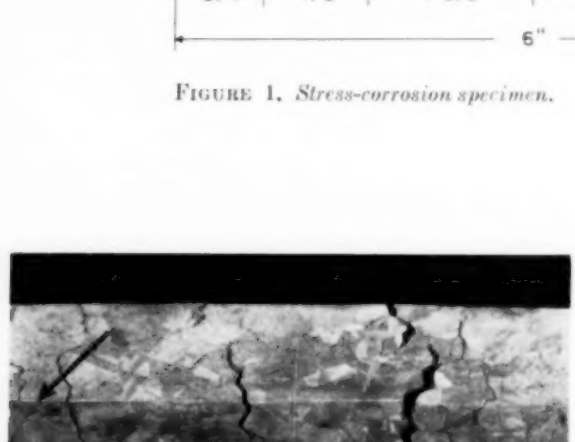

FIGURE 2.—*Specimen showing stress-corrosion cracks extending from the corner (marked by arrow) into the adjoining surfaces of specimen.* × 2

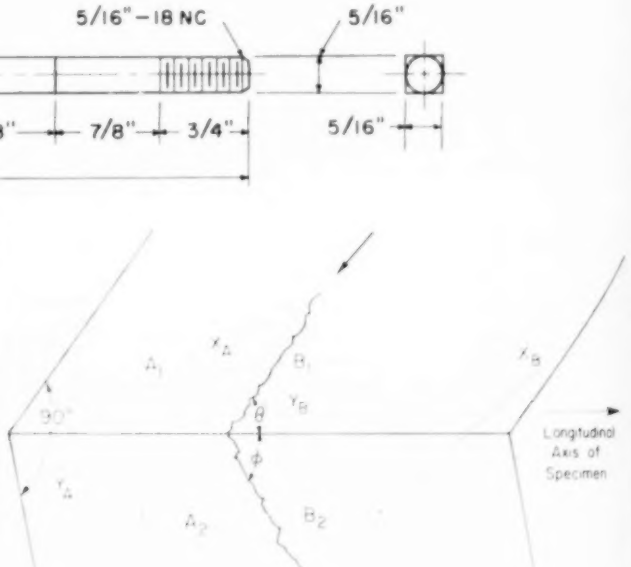

FIGURE 3. *Schematic drawing of crystals A and B with stress-corrosion crack (indicated by arrow) making an angle θ with corner of specimen in face 1 and angle φ in face 2.*

Rectilinear axes corresponding to cubic poles are indicated by X_A, X_B, etc.

considered to be faces machined normal to each other from crystal A. In the study of intercrystalline cracking a similar check was made on crystal B. The angles, θ and ϕ that the stress-corrosion cracks made with the common edge of the specimen were determined on surfaces 1 and 2, respectively, with a toolmaker's microscope. These angles then being known, the traces of the stress-corrosion crack could be plotted on the stereographic projections for the two surfaces of the crystals [*14*], and the normal to the plane of fracture could also be plotted on each projection.[2]

In order to determine the difference in orientation between the two crystals bounding intercrystalline stress-corrosion cracks, the angles between the cubic poles [3] and the normals to the planes of fracture in the two crystals were measured using a Wolf net. From these data the normals to the plane of fracture in any crystal could be plotted in a single 100, 110, 111 stereographic triangle, and if the fracture was intercrystalline the angle between the normals to the planes bounding the fracture was determined.

3. Results and Discussion

The corners of the specimens were points of stress concentration and examinations of the specimens indicated that stress-corrosion cracks originated there. This fact and the rectangular cross section of the specimens made possible the determination of the crystallographic plane or planes followed by or bounding the stress-corrosion cracks.

3.1. Alpha Brass

The orientations of the planes bounding 13 intercrystalline stress-corrosion cracks in 70-percent-Cu–30-percent-Zn brass and 11 cracks in 90-percent-Cu–10-percent-Zn brass were determined. Data were obtained from four different specimens of each alloy, each of which contained more than one stress-corrosion crack. The results, plotted in a single stereographic triangle, are shown in figure 4.

The crystal boundaries and the consequent intergranular cracks do not necessarily follow the same crystallographic planes throughout their entire lengths. Hence at different points on the boundary between two crystals the bounding planes may be different. In this investigation the bounding crystallographic planes were determined not only at the incidence of cracking but also at some other points along the continuous path that was representative of the general path or trend of the crack between the same two crystals. Poles of the latter planes were distributed in the same general way as those shown in figure 4. The distribution of the normals to all of these planes both at the incidence and along the general path of the crack is random. These data definitely indicate that it is the angle at which the crystallographic planes intersect that determines the susceptibility of a particular grain boundary, in alpha brass, to the development of stress-corrosion cracks.

The angles between the crystallographic planes in the paired crystals of the two alloys, determined by the methods described above, are given in table 1. Values were rounded to the nearest degree and are given in order of increasing magnitude.

For more than 70 percent of the cracks studied, the angles between bounding crystallographic planes at the origin of cracking were in the range of 13° to 23°, inclusive; the minimum angle for all the pairs of crystals studied was 8°. Angles of 13° to 23° are in the range in which maximum grain-boundary energies have been reported for the face-centered metals silver [*15*] and lead [*16*], as well as for tin [*10*] and an iron-silicon alloy [*11*].

No experimental data for brass have come to the author's attention; however, a value of 22.2° has been reported for copper [*17*]. The data indicate that the intercrystalline stress-corrosion cracking in

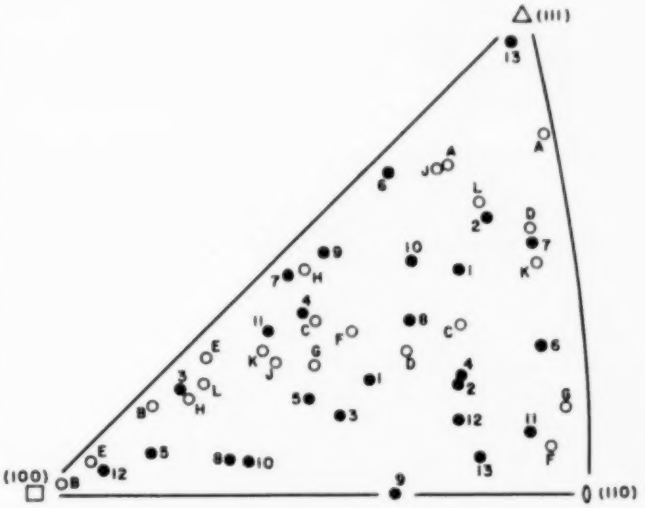

FIGURE 4. *Locations of normals to planes along which the stress-corrosion cracks originated.*

●, 70% Cu–30% Zn brass; ○, 90% Cu–10% Zn brass. Numbers or letters correspond to crystals pairs given in table 1.

[2] The normals plotted on the projections for surface 2 of crystals A or B must be brought into coincidence with those on surface 1 by the same rotation that will bring the cubic poles into coincidence. In the case of intercrystalline fractures, if the projection for surface 1 of crystal A is superimposed on that for surface 1 of crystal B so that their N–S poles, previously aligned with a fixed point on the specimen (longitudinal axis), coincide, the normals to the fractured surface will also coincide; similar results are also obtained for surface 2. It is thus seen that there is no ambiguity as to the normal to the plane of the stress-corrosion crack.

[3] The cubic poles of crystal A are designated orthogonal axes X_A, Y_A, Z_A, and the angles between the normal and these poles are designated P_x, P_y, and P_z, respectively. Angles determined on face 1, designated P_{x1}, etc., were checked by the determination of angles on face 2 designated P_{x2}, etc. As a further check use was made of the expression

$$|\cos P_{x1} \cos P_{x2}| + |\cos P_{y1} \cos P_{y2}| + |\cos P_{z1} \cos P_{z2}| \pm \Delta = 1$$

Δ was the cosine of the angle of closure; if it were larger than 0.010 it indicated the need for rechecking the measurement of the angles. An average value for P_x, etc., could then be obtained as follows:

$$\cos P_x = \pm \sqrt{|\cos P_{x1} \cos P_{x2}| \pm \Delta/3}.$$

The angles for crystal B could be similarly determined and designated Q_x, etc. The angle, a, between the crystallographic planes on opposite sides of the fracture can then be determined analytically (providing P_x, P_y, Q_x, Q_y, etc., are selected in the order of decreasing magnitude of the angles for each crystal) from the following expression:

$$\cos a = |\cos P_x \cos Q_x| + |\cos P_y \cos Q_y| + |\cos P_z \cos Q_z|$$

In the cubic system a unique solution for the angle between two crystallographic planes generally cannot be obtained. The angle determined either graphically or analytically by the methods described above is the smallest angle between the two planes.

TABLE 1. *Angles between crystallographic planes bounding stress-corrosion cracks and resolved tensile stresses on planes of crack, as a fraction of the applied tensile stress*

70% Cu-30% Zn			90% Cu-10% Zn		
Crystal pair [a]	Angle between crystallographic planes	Resolved tensile stress	Crystal pair [a]	Angle between crystallographic planes	Resolved tensile stress
	deg			*deg*	
1	11	0.891	A	8	0.834
2	13	.903	B	11	.976
3	13	.629	C	11	.961
4	14	.917	D	13	.804
5	14	.982	E	14	.978
6	18	.917	F	18	.927
7	19	.966	G	20	.998
8	19	.895	H	20	.879
9	21	.991	J	21	.903
10	21	.819	K	23	.968
11	23	.760	L	26	.951
12	30	.438			
13	32	.946			

[a] Numbers or letters correspond to poles shown in figure 4.

alpha brass is associated with grain boundaries that may be expected to have high energy contents.

It is suggested that in an environment containing the ammonium ion, galvanic cells will be set up with the high-energy grain boundaries as the anodes and the grain faces or other lower-energy areas as the cathodes. The circuits are completed through the interior of the alloy. The metal will be dissolved at the grain boundary anodes and the resulting pits will have the appearance, in cross section, of sharp notches with their apexes on the grain boundaries. On the exposed surfaces of the grains the ratio of anodic to cathodic areas will generally be much larger than those of the grain boundary areas to their cathodes. Hence pits formed on the exposed surfaces of the grains will be much shallower and will have a more rounded cross section than those formed at grain boundaries. In the absence of stress, pitting in either case will become more or less self-limiting, because of polarizing effects, and intercrystalline corrosion extending to any appreciable depth will be extremely rare. On the other hand, sharp notches centered on grain boundaries and favorably oriented with respect to either residual or applied tensile stress patterns will act as regions of stress concentration. As the notches become sufficiently deep or the stresses sufficiently high, the protective film on the brass at the roots of the notches will be ruptured, exposing metal that has an electrochemical-solution potential approximately ½ v more negative than the metal covered with an atmospherically formed film or with corrosion products [12]. The unfilmed, or unprotected, metal will corrode rapidly until failure occurs or until polarizing effects or shifting stresses permit reforming of the protective films. Corrosion will then be general until stress concentrations again rupture the protective film.

In experimental confirmation of this theory, tensile

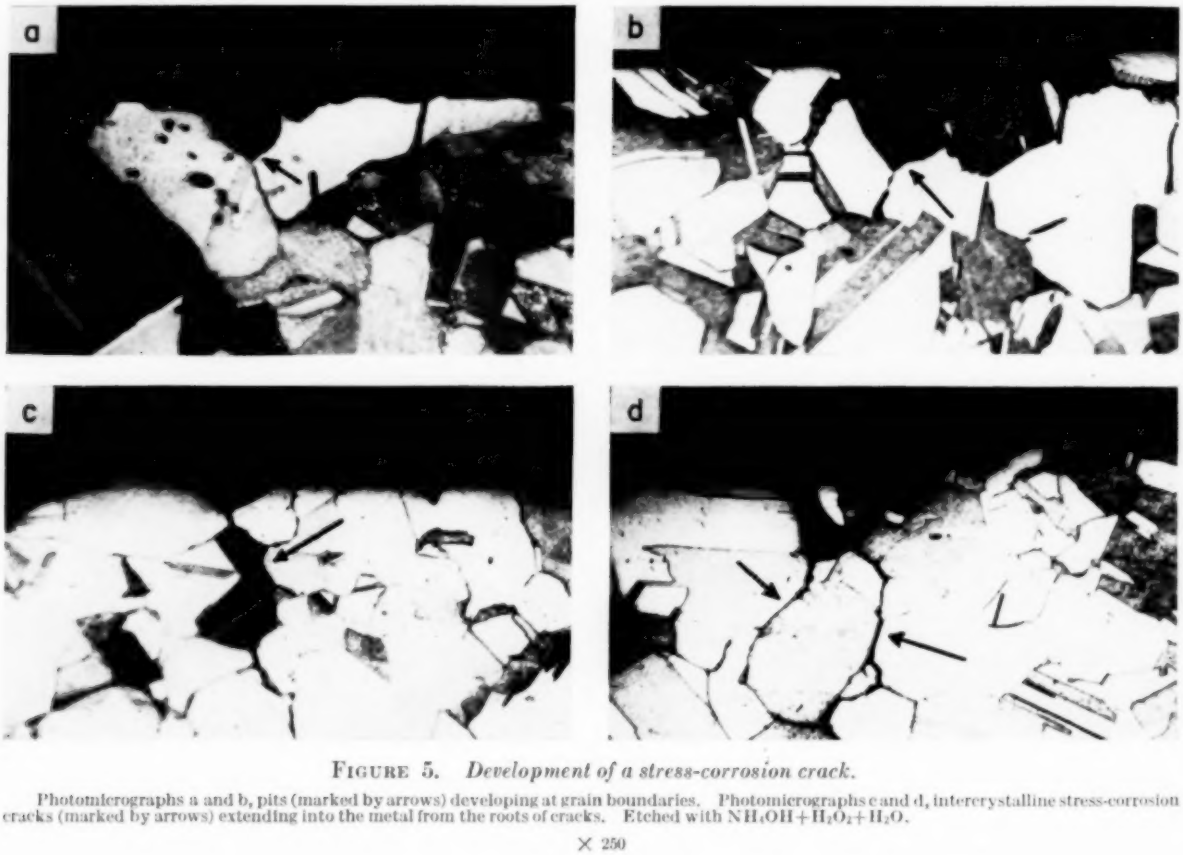

FIGURE 5. *Development of a stress-corrosion crack.*

Photomicrographs a and b, pits (marked by arrows) developing at grain boundaries. Photomicrographs c and d, intercrystalline stress-corrosion cracks (marked by arrows) extending into the metal from the roots of cracks. Etched with $NH_4OH+H_2O_2+H_2O$.

× 250

specimens of fine-grained cartridge brass were exposed under a tensile stress of approximately 45 percent of the yield strength in an ammonia, carbon dioxide, water vapor, and air atmosphere for periods ranging from 2 to 8 hr. Specimens exposed for 2 to 4 hr contained pits with their apexes at grain boundaries, as is shown in figure 5, a and b. The first evidence of stress-corrosion cracks was found in specimens exposed for 6 hr. These cracks extended from the roots of pits into the alloy along the grain boundaries in some of these specimens (fig. 5, c and d).

The residual stresses in the large-grained specimens of alpha brass were believed to be extremely small. The resolved tensile stresses on the planes of the stress-corrosion fractures were computed as fractions of the applied tensile stress and are given in table 1. It is seen that for most specimens the resolved tensile stress was 85 percent or more of the applied stress. Thus, the stress patterns were generally in such directions as to produce stress concentrations at the roots of notches formed by the corrosive process. This satisfied one of the conditions for the propagation of stress-corrosion cracks.

There was no appreciable difference between the results obtained on the cast and fully annealed wrought specimens of the 90-percent Cu–10-percent Zn alloy from the same heat.

3.2. Beta Brass

Eighteen crystals of beta brass (from four specimens) containing 47 transcrystalline stress-corrosion cracks were studied. The normals to the crystallographic planes on which these cracks were believed to have originated were determined and are plotted in a single stereographic triangle in figure 6. It is seen from these data that there is no plane or family of planes in beta brass that is particularly susceptible to stress-corrosion cracking.

If the stress-corrosion cracking of beta brass is associated with the rupture of the protective film, as is believed to be the case for alpha brass, it must be associated with either elastic or plastic deformation of the material. Webb [*18*], Rinehart [*19*] and Good [*20*] have shown that single crystals of beta brass are very anisotropic in the elastic range. Young's modulus is 8.2 times as great in the [111] direction as in the [100] direction, and the shear modulus is 12.8 times as great in the [100] direction as in the [111] direction. It was also shown that there is a linear relation between $1/E$ or $1/G$ and $f(l, m, n)$, where $f(l,m,n) = (l^2m^2+n^2m^2+n^2l^2)$ and l, m, and n are the direction cosines of the normals to any crystallographic plane with respect to the cubic axes. The values of $1/E$ and $1/G$ have been computed for both the directions parallel to the stress axis and those normal to the transcrystalline stress-corrosion cracks studied and are given in table 2. It is recognized that, because of the restraining effects of the neighboring crystals, the strain produced in a given crystallographic direction in a crystal in a polycrystalline aggregate may be different from that calculated for a single crystal.

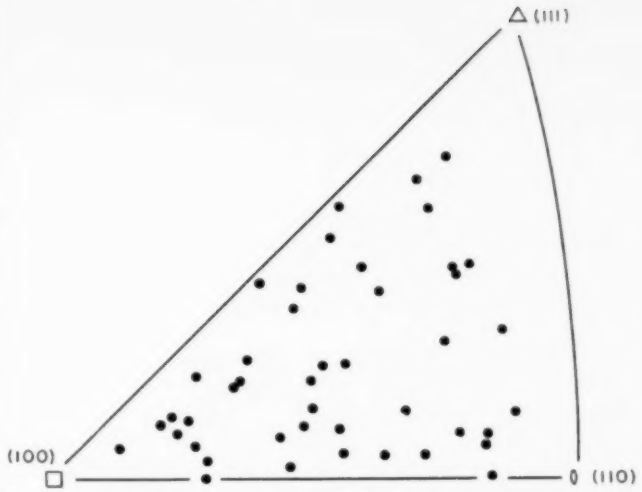

FIGURE 6. *Normals to planes containing transcrystalline stress-corrosion cracks in beta brass.*

Data obtained at the Bureau indicated, however, that there was greater elastic tensile strain for a given stress in polycrystalline grains of cast beta brass, oriented so that the [100] directions were closer to the tensile axis, than for grains with the [100] directions oriented 10° or more from that axis. Most of the crystals studied in this investigation, however, were so oriented that the [100] directions made angles greater than 10° with both the tensile axis and the normals to the planes of fracture. Hence, the possibility of microscopic plastic deformation by slip was considered. The critical shear stress for slip may be defined as $\tau = \sigma \cos \phi \cdot \cos \lambda$, where σ is the applied stress, and ϕ and λ are the angles between the direction of the applied stress and the slip plane and the slip direction (in the slip plane), respectively. Slip in beta brass has been reported [*21*] to occur on the (110) planes in the [111] direction. The angles that both the tensile axes and the normals to the planes, on which the stress-corrosion cracks were believed to originate, made with the various (110) planes and the [111] directions (lying in the respective (110) planes) were measured for each crack studied. The products of the cosines of these angles were determined for each pair of angles for each stress-corrosion crack, and the maximum value or values are given in table 2. The values obtained for the normals to the planes upon which stress-corrosion cracking originated are plotted in figure 7. There were also available orientation data for 81 large crystals in two polycrystalline beta brass tensile specimens. The values of the product $\cos \phi \cdot \cos \lambda$ (with respect to the tensile axes of the specimens) were determined and are also plotted in figure 7. If the probability of slip in a given crystal increases as the value of $\cos \phi \cdot \cos \lambda$ approaches 0.5, it is seen that there is a greater probability of slip in the crystals containing stress-corrosion cracks than in the randomly selected crystals in the tensile specimens.

A study of the data in table 2 indicates that in many cases both the probability of slip ($\cos \phi \cdot \cos \lambda$)

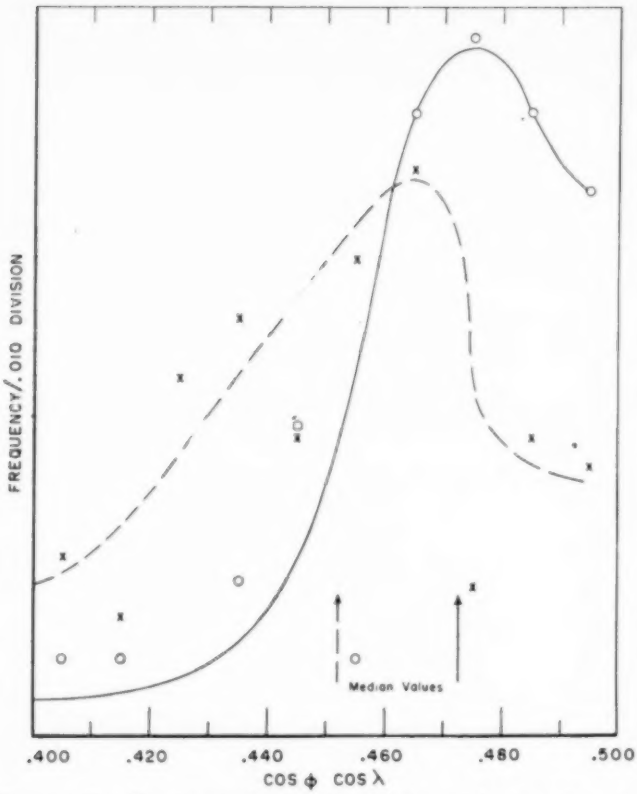

FIGURE 7. *Frequency distribution of the product cos θ cos λ.*

Values from table 2 are weighted so that they can be plotted on the same scale as data from randomly distributed crystals. ϕ=angle between normal to slip plane and stress-corrosion crack; λ=angle between the normal to stress-corrosion crack and the slip direction lying in the slip plane. Critical resolved shear stress=$\sigma \cos \cdot \phi \cos \lambda$. ○, crystal containing stress-corrosion cracks; ×, randomly distributed crystals.

and the reciprocal of the shear modulus (shear strain per unit shear stress) are large not only for stresses parallel to the stress axis but also for those normal to the stress-corrosion crack. Generally, in other cases, if one of these values is small the other is large.[4]

Smith [22] found experimentally that the grain-boundary energy of beta grains in an alpha-beta brass is only about three-quarters that of the alpha boundaries. If the grain-boundary energy in this alloy increases with increased difference in orientation of the crystals, as has been shown for certain other metals, it may be expected that pitting will occur at certain high-energy boundaries more readily than on grain surfaces. Hence, some stress-corrosion cracks may be expected to originate at grain boundaries in the beta brass by the same process described for alpha brass. Metallographic examinations at the Bureau showed that a small percentage of the stress-corrosion cracks do originate at grain boundaries. However, these become transcrystalline before they have penetrated to the depth of a full grain into the metal. Evidently factors other than high-energy grain boundaries determine the paths followed by stress-corrosion cracks in beta brass.

It is postulated that regions of stress concentration produced by pitting corrosion (or in a few instances by grain-boundary attack) in beta brass nucleate microscopic slip in the suitably oriented crystals. This slip ruptures the protective film (formed in the atmosphere or in the corroding medium) exposing narrow areas of film-free metal that are anodic to the film-covered metal, and stress-corrosion then progresses as was indicated for alpha brass. In further support of this thesis it should be noted that plastic deformation has been reported [23] and shown [24] to be associated with the transcrystalline stress-corrosion cracking of magnesium alloys. In the Bureau, slip lines have recently been found associated with transcrystalline stress-corrosion cracking of type 304 stainless steel.

4. Summary

The crystallographic planes followed by stress-corrosion cracks in beta brass and the angle between the planes in the crystals on either side of the intercrystalline cracks in alpha brass were determined by X-ray diffraction methods for specimens of beta brass and two compositions of alpha brass.

The crystallographic planes bounding intercrystalline stress-corrosion cracks in alpha brass and on which the stress-corrosion cracks originated in beta brass were randomly distributed. There was no plane or family of planes that was particularly susceptible to stress-corrosion cracking.

About 70 percent of the stress-corrosion cracks studied in alpha brass originated between crystals in which the bounding planes were oriented at angles of 13° to 23° to each other. This is the range in which the maximum interfacial energies have been reported for other materials. It is suggested that in a corroding medium the grain boundaries having the highest energies become the loci of pits. In the absence of stress these pits are most probably self limiting, but with the application of favorably oriented tensile stresses they act as areas of stress concentration that may produce rupture of the normal protective film at the roots of the pits. This film-free metal is rapidly attacked and early intercrystalline failure of the metal may result.

Assuming that there is a critical resolved shear stress for slip in beta brass, it was shown that there was a greater probability of slip occurring in crystals containing transcrystalline stress-corrosion cracks than in randomly distributed crystals. It is postulated that in a corrosive medium, microscopic slip, most probably nucleated by pitting, ruptures the protective film on the surface of the metal. The film-free metal is rapidly attacked and transcrystalline failure of the brass results.

The resolved tensile stresses normal to the stress-corrosion fractures were generally 80 percent or more of the applied tensile stresses in both the alpha and beta brasses, thus indicating that these stresses were favorably oriented for the propagation of stress-corrosion cracks.

[4] In crystal 9 both cos ϕ cos λ and $1/G$ are small; however, $1/E$ has a value of 3.65 cm^2/dyne$\times 10^{-12}$. It is suggested that in this case the film rupture resulted from elastic tensile strain.

TABLE 2. *Probability of slip, $f(\cos\phi, \cos\lambda)$ and reciprocals of elastic and shear moduli of stresses applied along the stress axis and normal to transcrystalline stress-corrosion cracks in beta brass. $f(\cos\phi, \cos\lambda) = \cos\phi \cos\lambda$ where ϕ and λ are angles between the stress axis (or ϕ', λ', normal to the fracture) and the slip plane and slip direction respectively*

Crystal	Stress parallel to tension axis			Angle between tension axis and normal to stress corrosion crack	Resolved tensile stress normal to stress corrosion crack	Stress normal to stress-corrosion crack		
	$\cos\phi \cos\lambda$	$1/E$	$1/G$			$\cos\phi' \cos\lambda'$	$1/E$	$1/G$
		$cm^2/dyne$	$cm^2/dyne$	*deg*			$cm^2/dyne$	$cm^2/dyne$
1	0.455	1.24×10^{-12}	4.64×10^{-12}	38	0.788	=0.481, 0.476	3.37×10^{-12}	1.35×10^{-12}
				21	.934	.482	1.75	3.8
				11	.982	.440	1.43	4.3
2	.462	1.43	4.33	22½	.924	.500	1.97	3.45
				26	.899	.461	1.65	4.48
				15	.966	.500	1.50	4.20
				13	.974	.495	1.48	4.25
3	.496	3.00	1.90	17	.956	.447	2.85	2.30
				6½	.994	.477	2.95	1.97
				14½	.968	.486	1.57	4.10
				19	.946	.475	3.20	1.20
				23	.921	.481, 0.477	3.30	1.43
4	.406	.79	5.25	41	.755	.447	3.73	2.35
				21½	.930	.491, 0.491	1.09	4.83
5	.495	3.01	1.90	35	.819	.370	.87	5.08
				38	.788	.468	.75	5.35
				37½	.793	.448	1.17	4.72
				14	.970	.461	3.37	1.33
				24½	.910	.451	3.75	0.77
				17½	.954	.492	3.73	0.85
6	.470	3.55	1.08	18	.951	.489	2.53	2.60
				5½	.995	.477	3.18	1.55
				11	.982	.492	2.73	2.30
7	.379	.48	5.75	12	.978	.404	1.28	4.55
8	.463	3.46	1.20	23	.921	.475	1.57	3.95
				14½	.968	.497	2.26	3.05
9	.419	3.65	0.85	9½	.986	.487, 0.483	3.30	1.45
				18	.951	.500, 0.492	2.57	2.57
10	.477	2.86	2.12	19½	.943	.438	1.15	4.73
11	.489	1.68	3.95	18½	.948	.464	1.23	4.65
				8	.980	.469	1.48	4.25
				8½	.980	.471	1.48	4.25
				11½	.980	.500	2.36	2.85
				12½	.976	.469	1.57	4.10
12	.454	3.53	1.10	25½	.903	.473	3.25	1.55
13	.491	2.98	1.93	27	.891	.464	2.23	3.08
				24	.914	.489	2.16	3.20
14	.413	2.57	2.56	15	.966	.468	1.42	4.37
15	.459	3.68	0.85	32	.848	.442	1.40	4.37
16	.408	1.30	4.50	34	.829	.410	.97	5.00
17	.484	2.80	2.20	34½	.824	.457	1.37	4.40
18	.487	2.93	2.00	17	.956	.482	1.50	4.20

[a] In those cases where two values were approximately the same both are given.

5. References

[1] Erwin S. Sperry, The season-cracking of brass and bronze tubing, Brass World **2,** 39 (1906).

[2] H. P. Croft, Influence of external stresses on tendency of brass wires to stress-corrosion crack, as indicated by the mercurous nitrate test, Proc. ASTM **41,** 905 (1941).

[3] H. P. Croft and G. Sachs, Stress cracking of brass, Iron Age **151,** 47 and 62 (1943).

[4] M. E. Whitaker, Intercrystalline failure of brasses and aluminum brasses in air, ammonia, and certain aqueous solutions and molten metals, Metallurgia **39,** 66 (1948).

[5] D. H. Thompson and A. W. Tracy, Influence of composition on the stress-corrosion cracking of some copper-base alloys, J. Metals **1,** 100 (1949).

[6] T. A. Read, J. B. Reed, and H. Rosenthal, The mechanism of season cracking of brass, ASTM-Am. Inst. Mining Met. Engrs., Symposium on Stress-Corrosion Cracking of Metals, p. 90 (1944).

[7] W. D. Robertson, Preferred orientation as a factor in intergranular corrosion, J. Metals **188,** 790 (1950).

[8] Metal Interfaces, Am. Soc. Metals (Cleveland, Ohio, 1952).

[9] H. Brooks, Theory of internal boundaries, Metal Interfaces, p. 32, Am. Soc. Metals (Cleveland, Ohio, 1952).

[10] K. T. Aust and B. Chalmers, The specific energy of crystal boundaries in tin, Proc. Roy. Soc. (London) [A] **201,** 210 (1950).

[11] C. G. Dunn, F. W. Daniels, and M. J. Bolton, Relative energies of grain boundaries in silicon iron, Trans. Am. Inst. Mining Met. Engrs. **188,** 1245 (1950).

[12] H. L. Logan, Film rupture mechanism of stress corrosion, J. Research NBS **48,** 99 (1952) RP2291.

[13] Alden B. Greninger, Determination of orientations of metallic crystals by means of back-reflection Laue photographs, Trans. Am. Inst. Mining Met. Engrs. **117,** 61 (1935).

[14] Charles S. Barrett, Structure of metals, p. 39 (McGraw-Hill Book Co., Inc., New York, N. Y., 1943).

[15] A. P. Greenough and Ronald King, Grain Boundary energies in silver, J. Inst. Met. **79,** 415 (1951).

[16] K. T. Aust and B. Chalmers, Surface energy and structure of crystal boundaries in metals, Proc. Roy. Soc. (London) [A] **204,** 359 (1950).

[17] H. Brooks, Theory of internal boundaries, Metal Interfaces, p. 41, Am. Soc. Metals, (Cleveland, Ohio, 1952).

[18] Wayne Webb, A study of beta brass in single crystal form, Phys. Rev., ii, **55,** p. 297 (1939).

[19] John S. Rinehart, Temperature dependence of Young's modulus of beta brass single crystals, Phys. Rev., ii, **58,** p. 365 (1940).

[20] W. A. Good, Rigidity modulus of beta brass single crystals, Phys. Rev., ii, **60,** p. 605 (1941).

[21] Alden B. Greninger, Deformation of beta brass, Trans. Am. Inst. Mining Met. Engrs. **128,** 369 (1938).

[22] C. S. Smith, Grains, phases and interfaces: An interpretation of microstructure, Trans. Am. Inst. Mining Met. Engrs. **175,** 25–35 (1948).

[23] D. K. Priest, F. H. Beck, and M. G. Fontana, Stress-corrosion mechanism in a magnesium-base alloy, Trans. Am. Soc. Metals **47,** 486 (1955).

[24] R. D. Williams, Kansas City Meeting NACE, March 16, 1954 (unpublished).

WASHINGTON, November 15, 1955.

U. S. GOVERNMENT PRINTING OFFICE: 1956

Recent Publications of the National Bureau of Standards

Journal of Research of the National Bureau of Standards, volume **56**, No. 1, January 1956 (RP2641 to RP2647 incl.). Annual subscription $4.00.

Technical News Bulletin, volume **40**, No. 1, January 1956. 10 cents. Annual subscription $1.00.

Basic Radio Propagation Predictions for April 1956. Three months in advance. CRPL 137. Issued January 1956. 10 cents. Annual subscription $1.00.

Research Papers

Journal of Research, volume 56, number 1, January 1956. Single copies of the Journal vary in price. Single copies of Research Papers appearing in the Journal are not available for sale. The Superintendent of Documents, U. S. Government Printing Office, Washington 25, D. C., will reprint 100 or more copies of a Research Paper. Requests for the purchase price should be mailed promptly to that office.

RP2641. Dielectric constant of water from 0° to 100° C. C. G. Malmberg and A. A. Maryott.

RP2642. A calorimeter for measuring the power in a high-energy X-ray beam. John McElhinney, Bernard Zendle, and Steve Domen.

RP2643. Pyrochlore-type compounds containing double oxides of trivalent and tetravalent ions. Robert S. Roth.

RP2644. Thermal decomposition of polytetrafluoroethylene in various gaseous atmospheres. L. A. Wall and J. D. Michaelsen.

RP2645. Abscissas and weights for Gaussian quadratures of high order. P. Davis and P. Rabinowitz.

RP2646. Behavior of cements and related materials under hydrostatic pressures up to 10,000 atmospheres. C. E. Weir, C. M. Hunt, and R. L. Blaine.

RP2647. Formulas for inverse oculatory interpolation. Herbert E. Salzer.

Publications in Other Journals

International plastic committee considers standard tests. G. M. Kline. The Magazine of Standards (70 E. 45th St., New York 17, N. Y.) **26**, No. 10, 305 (Oct. 1955).

World unification of screw threads. I. H. Fullmer. The Magazine of Standards (70 E. 45th St., New York 17, N. Y.) **26**, No. 10, 306 (Oct. 1955).

Some fading characteristics of regular VHF ionospheric propagation. G. R. Sugar. Proc. I. R. E. (1 E. 79th St., New York 21, N. Y.) **43**, No. 10, 1432 (Oct. 1955).

Residual lattice strains in sectioned bars of plastically deformed iron. C. J. Newton and H. C. Vacher. J. Metals (29 W. 39th St., New York 18, N. Y.) **7**, No. 11, 1193 (Nov. 1955).

Variability of wool content in part wool blankets. Emanuel Horowitz and W. S. Connor. ASTM Bulletin (1916 Race St., Philadelphia 3, Pa.) No. 208, 42 (Sept. 1955).

Determination of sulfur in rubber vulcanisates. E. W. Zimmerman, V. E. Hart, and Emanuel Horowitz. Anal. Chem. (1155 16th St. NW., Washington 6, D. C.) **27**, No. 10, 1606 (Oct. 1955).

Sorption of macromolecules to solid surfaces: sorption of dextran to cellulose nitrate membranes in the presence of serum albumin and surface-active agents. S. Rothman, John Mandel, Florence R. McCann, and S. G. Weissberg. J. Colloid Sci. (Academic Press, 125 E. 23d St., New York 10, N. Y.) **10**, No. 4, 338 (Aug. 1955).

A note on the estimation of sodium carbonate in photographic developers. Chester I. Pope. J. Soc. Motion Picture and Television Engrs. (20th and Northampton Sts., Easton, Pa.) **64**, 420 (Aug. 1955).

Tektites and the lost planet. Ralph Stair. Smithsonian Institution (Washington 25, D. C.) Annual Report, Publication No. 4194, 217 (1955).

Publications for which a price is indicated are available only from the Superintendent of Documents, U. S. Government Printing Office, Washington 25, D. C. (foreign postage, one-third additional). Reprints from outside journals are not available from the National Bureau of Standards but can often be obtained from the publishers.

UNITED STATES
GOVERNMENT PRINTING OFFICE
DIVISION OF PUBLIC DOCUMENTS
WASHINGTON 25, D. C.

OFFICIAL BUSINESS

PENALTY FOR PRIVATE USE TO AVOID PAYMENT OF POSTAGE, $300 (GPO)

Contents

		Page
Penetration of gamma radiation from a plane monodirectional oblique source. Martin J. Berger.	RP2656	111
A re-entrant cavity for measurement of complex permeability in the very-high-frequency region. R. D. Harrington, R. C. Powell, and P. H. Haas.	RP2657	129
Fundamental factors controlling electrical resistivity in vitreous ternary lead silicates. Simon W. Strauss, Dwight G. Moore, William N. Harrison, and Lloyd E. Richards.	RP2658	135
Some factors affecting the precision of polarographic half-wave potential measurements. John K. Taylor and Stanley W. Smith.	RP2659	143
Infrared measurements from 50 to 125 microns. Earle K. Plyler and Nicolo Acquista.	RP2660	149
Surface tension of molten glasses in the system barium oxide-boric oxide-silica. Herman F. Shermer.	RP2661	155
Relationship between crystal orientation and stress-corrosion cracking in alpha and beta brasses. Hugh L. Logan.	RP2662	159

Single copies of the above Research Papers are not available for sale, but the Superintendent of Documents, U. S. Government Printing Office, Washington 25, D. C., will reprint 100 or more copies, and request for the purchase price should be mailed promptly to that Office.

[A list of recent NBS publications is given on page 3 of the cover.]

For sale by the Superintendent of Documents, U. S. Government Printing Office, Washington 25, D. C. Price 60 cents (Single copy). Subscription price: $4.00 a year; $1.25 additional for foreign mailing. Single copies vary in price.

UNITED STATES GOVERNMENT PRINTING OFFICE, WASHINGTON : 1956